

## ABSTRACT

Title of dissertation: MULTI-SPECIES TRAPPED ATOMIC ION  
MODULES FOR QUANTUM NETWORKS

Ismail Volkan Inlek, Doctor of Philosophy, 2016

Dissertation directed by: Professor Christopher Monroe  
Joint Quantum Institute  
University of Maryland Department of Physics  
and  
National Institute of Standards and Technology

Trapped atomic ions are among leading platforms in quantum information processing with their long coherence times and high fidelity quantum operations. Scaling up to larger numbers of qubits is a remaining major challenge. A network of trapped ion modules offers a promising solution by keeping a manageable number of qubits within a module while photonic interfaces connect separate modules together to increase the number of controlled memory qubits. Since the generation of entanglement between qubits in different modules is probabilistic, an excessive number of connection trials might result in decoherence on the memory qubits through absorption of stray photons. This crosstalk issue could be circumvented by introducing a different atomic species as photonic qubits. Compared to a system that only utilizes single species of atoms, there are also additional advantages in a multi-species apparatus where attractive features of each atom can be employed for certain tasks. In this thesis, I present experimental demonstrations of necessary ingredients of a

multi-species module for quantum networking. In these experiments,  $^{138}\text{Ba}^+$  ions are intended to be used as photonic communication qubits with visible photon emission lines that are more convenient for current fiber optics and detector technologies while  $^{171}\text{Yb}^+$  ions are used for storing and processing quantum information where long coherence times available in hyperfine clock states make them suitable memory qubits. The key experiments include demonstration of atom–photon entanglement using the  $^{138}\text{Ba}^+$  qubit and utilizing the Coulomb interaction between  $^{171}\text{Yb}^+$  and  $^{138}\text{Ba}^+$  with spin-dependent forces for transfer of information from communication to memory qubits.

MULTI-SPECIES TRAPPED ATOMIC ION  
MODULES FOR QUANTUM NETWORKS

by

Ismail Volkan Inlek

Dissertation submitted to the Faculty of the Graduate School of the  
University of Maryland, College Park in partial fulfillment  
of the requirements for the degree of  
Doctor of Philosophy  
2016

Advisory Committee:  
Professor Christopher Monroe, Chair/Advisor  
Professor Alexey Gorshkov  
Professor Mohammad Hafezi  
Professor Alan Migdall  
Professor Edo Waks

© Copyright by  
Ismail Volkan Inlek  
2016

# Dedication

*To Erin*

## Acknowledgments

Graduate school has been a challenging yet at the same time rewarding, exciting and fun experience for me. First of all, I want to thank my advisor Chris Monroe for making this possible. I am very fortunate to have had the chance to benefit from Chris' expertise and intuition. Lessons I learned through my errors and successes in conjunction with his guidance has been an invaluable part of my graduate school years.

In the Monroe group, I had the opportunity to work closely with very talented people who were instrumental on achieving the results presented on this thesis. I want to thank Dave Hayes, Kenny Lee, Susan Clark, Shantanu Debnath, Dave Hucul, Grahame Vittorini, Clay Crocker, Ksenia Sosnova and Marty Lichtman for their tireless work.

Even though I only briefly overlapped with Hayes, I was grateful to benefit from his deep understanding of physics in that short period of time, especially during the late night data acquisition sessions when we did not have improved entanglement rates yet. Similarly, Kenny leaved shortly after I joined the group but it was always fun listening to Coldplay with him in the lab and he was the person I learned how to properly build electronics. Although Shantanu has been reassigned to another project by the time I have joined the group, I inherited his ground work on FPGAs and built up on it, which has been a critical part on achieving the results published over the years. He has been the person I went when my code was not working properly for one reason or other. Susan did a tremendous job as the postdoc in

our project on re-setting up remote entanglement apparatus. Hucul was the senior grad student in the ion-photon project for the most part, and I'm incredibly happy he was there to teach me how to conduct an experiment and how to troubleshoot problems when things do not work as expected. He has truly been a role model for me. Grahame was by far the most interesting person I have interacted with, in a good way. The lab environment has been a very enjoyable place to work with him and through his expertise in ion trapping, we tackled many problems. I also thank him for founding the "National Turkish-American Friendship Portrait Gallery" and hopefully he will continue commissioning my art projects in the future. Clay has been very helpful as the junior grad student on the experiments, especially on setting things up for the barium atoms. His contribution to results presented on this thesis has been significant. After Hucul and Grahame's departure, Ksenia and Marty become part of the project. Ksenia's theoretical work has illuminated us on characterizing barium ions and she has been improving rapidly on experimental techniques since. Marty joined us in my last year and helped us getting these results as well. I believe his expertise in optimization processes and automation will be crucial in taking research efforts to next level. I also want to thank all the other past and present group members, who were always there to lend an advice when I needed it.

I want to thank my family who were very supportive of my Ph.D. pursuit even when it meant I'll be on the other side of the world. And finally, without my wife Erin's support and love, this work would not have been possible.

# Table of Contents

List of Tables	vii
List of Figures	viii
List of Abbreviations	x
1 Introduction	1
1.1 Modular Quantum Networks . . . . .	1
1.2 Multi-Species Modules . . . . .	5
1.2.1 Entanglement of Remote Qubits . . . . .	6
1.2.2 Entanglement Generation Probability . . . . .	12
1.2.3 Crosstalk Considerations . . . . .	13
1.2.4 Additional Advantages of a Multi-Species Setup . . . . .	18
1.2.5 Multi-Species Network Architecture . . . . .	18
1.3 Previous Experiments . . . . .	19
2 Experimental Setup	21
2.1 RF Paul Traps and Vacuum Chamber . . . . .	21
2.2 Ytterbium and Barium Atomic Ions . . . . .	22
2.2.1 Overview . . . . .	22
2.2.2 Neutral Sources and Photo-ionization . . . . .	25
2.2.3 Methods for Getting Fluorescence Photons from Barium Ions . . . . .	28
2.2.3.1 Co-trapping for Verification of $^{138}\text{Ba}^+$ Loading . . . . .	28
2.2.3.2 $^{138}\text{Ba}^+$ Transition Wavelength Measurements with HCL . . . . .	30
2.2.4 The Optical Bloch Equations . . . . .	30
2.2.4.1 Three level system . . . . .	33
2.2.4.2 Eight level system . . . . .	39
2.3 Double Imaging Setup . . . . .	40
2.4 High Numerical Aperture Setup . . . . .	41
2.5 Re-ordering of the Ions . . . . .	44

3	Ytterbium and Barium Atomic Ion Qubits	46
3.1	Overview	46
3.2	Ytterbium Hyperfine Qubit	47
3.3	Barium Zeeman Qubit	50
3.3.1	Doppler Cooling	51
3.3.2	State Initialization	52
3.3.3	State Detection without Shelving	54
3.3.4	Laser Stabilization	59
3.3.5	Magnetic Field Stabilization	59
3.3.6	Atom-Photon Entanglement	63
3.3.6.1	Electric Dipole Transition with Fast Pulses	66
3.4	Coherent Rotations with 355-532 nm Pulses	68
3.4.1	The Rabi Frequencies	73
3.4.2	Differential Stark Shifts	75
3.4.3	Re-pumping from $^2D_{5/2}$ Level with an Orange LED	76
3.4.4	Crosstalk Between the Qubits and Raman Beams	80
4	Normal Mode Structure of Ytterbium-Barium Ion Chain	82
4.1	Normal Mode Eigenfrequencies and Eigenvectors	82
4.1.1	Longitudinal Modes	82
4.1.2	Transverse Modes	86
4.2	Spectroscopy Measurements	88
4.3	Sub-Doppler Cooling with Electromagnetically Induced Transparency	90
5	Phonon Mediated Interactions between Ytterbium and Barium Ions	100
5.1	Cirac-Zoller Interactions	100
5.1.1	Coherent Information Transfer Operation	101
5.1.2	Experimental Results	102
5.2	Mølmer-Sørensen Interactions	105
5.2.1	Spin-Dependent Forces	106
5.2.2	Multi-Species Entanglement	110
5.2.2.1	Experimental Considerations and Results	112
5.3	The Swap Gate	117
6	Outlook	120
6.1	Entanglement of Remote Barium Qubits	120
6.2	Maintaining Phase Stability in a Multi-Species Network	124
	Bibliography	126

## List of Tables

1.1	Overhead considerations in modular architectures . . . . .	5
3.1	Atomic properties of excited states . . . . .	74

## List of Figures

1.1	Modular Trapped Atomic Ion Network . . . . .	4
1.2	Photons Incident on a 50/50 Beam Splitter and Atom-Photon Entanglement . . . . .	8
1.3	Photonic Bell State Measurement . . . . .	11
1.4	Crosstalk Between Memory and Communication Qubits . . . . .	14
1.5	Distance Scaling of Crosstalk Mechanisms . . . . .	17
1.6	Multi-Species Network Architecture . . . . .	19
2.1	RF Paul Traps . . . . .	23
2.2	Photoionization of Neutral Barium . . . . .	27
2.3	Optogalvanic Effect and Transition Wavelength Measurements . . . . .	31
2.4	$^{138}\text{Ba}^+$ Energy Levels . . . . .	32
2.5	Simplified Three Level $\Lambda$ System of $^{138}\text{Ba}^+$ ion . . . . .	34
2.6	Three Level $\Lambda$ System Time Dynamics . . . . .	38
2.7	Excitation Spectrum of Three Level $\Lambda$ System . . . . .	39
2.8	Eight Level $\Lambda$ System Time Dynamics . . . . .	40
2.9	Excitation Spectrum of Eight Level $\Lambda$ System . . . . .	41
2.10	Double Imaging Setup . . . . .	42
2.11	High Numerical Aperture Setup . . . . .	43
3.1	$^{171}\text{Yb}^+$ Clebsch-Gordan Coefficients . . . . .	47
3.2	$^{171}\text{Yb}^+$ Qubit Operations . . . . .	48
3.3	$^{138}\text{Ba}^+$ Clebsch-Gordan Coefficients . . . . .	50
3.4	Doppler Cooling . . . . .	51
3.5	The $^{138}\text{Ba}^+$ Qubit State Initialization . . . . .	53
3.6	The $^{138}\text{Ba}^+$ Qubit State Detection . . . . .	56
3.7	State Detection/Initialization Optical Setup . . . . .	57
3.8	60 Hz Magnetic Field Noise . . . . .	61
3.9	Atom-Photon Entanglement . . . . .	64
3.10	Excitation with Short Pulses . . . . .	67
3.11	Magnetic Dipole Transitions . . . . .	68
3.12	Two Photon Stimulated Raman Transitions . . . . .	69
3.13	Stimulated Raman Transitions on $^{138}\text{Ba}^+$ and $^{171}\text{Yb}^+$ . . . . .	74

3.14	Differential Stark Shift on $^{138}\text{Ba}^+$	77
3.15	Deshelving From $^2D_{5/2}$ Levels with an Orange LED	79
4.1	Two Ion Longitudinal Mode Motional Amplitudes	85
4.2	Two Ion Longitudinal Mode Frequencies	85
4.3	Two Ion Transverse Mode Motional Amplitudes	87
4.4	Two Ion Transverse Mode Frequencies	87
4.5	Two Ion Transverse Mode Structure Dependence on Trap Parameters	89
4.6	Non-Copropagating Beam Geometry	90
4.7	Motional Spectrum	91
4.8	EIT Cooling	94
4.9	EIT Dynamics	97
4.10	Motional Spectrum with EIT Cooling	98
5.1	State Transfer with CZ interactions	103
5.2	Coherence Measurement of CZ interactions	104
5.3	Single Qubit Mølmer-Sørensen Interaction	109
5.4	Two Qubit Mølmer-Sørensen Interaction	112
5.5	The Raman Beam Configuration for $^{171}\text{Yb}^+ - ^{138}\text{Ba}^+$ MS Interaction	113
5.6	Schematic of Control Electronics	115
5.7	Multi-Species MS Interaction	118
6.1	Optical Pumping with a Beam Along Photon Collection Axis	122
6.2	Entanglement of Remote $^{138}\text{Ba}^+$ Qubits	123
6.3	Phase Stability on a Multi-Species Module	125

## List of Abbreviations

AOM	Acousto-Optic Modulator
APD	Avalanche Photo Diode
CZ	Cirac-Zoller
EIT	Electromagnetically Induced Transparency
EOM	Electro-Optic Modulator
HWP	Half Waveplate
HCL	Hollow Cathode Lamp
IP	In-Phase
MS	Mølmer-Sørensen
NA	Numerical Aperture
NV	Nitrogen-Vacancy
OP	Out-of-Phase
PBS	Polarizing Beam Splitter
PMF	Polarization Maintaining Fiber
PMT	Photo Multiplier Tube
QWP	Quarter waveplate
RF	Radio Frequency
SPAD	Single Photon Avalanche Diode
SNSPD	Superconducting Nanowire Single Photon Detector
UV	Ultraviolet

## Chapter 1: Introduction

### 1.1 Modular Quantum Networks

Scaling up the number of qubits while maintaining quantum coherence in the system is the current challenge in quantum information processing platforms [1–4]. Trapped ions are currently the leading candidate in this front for two major reasons. First, since they are nature’s qubit, they are identical with each other. Using qubits that only weakly interact with the environment, one can make use of frequencies that are very close to each other, which is helpful in building a large scale system. For instance, the hyperfine clock states of  $^{171}\text{Yb}^+$  are separated by [5]:

$$\omega_0/2\pi = 12\,642\,812\,118.5 + (310.8)B^2 \text{ Hz} \quad (1.1)$$

where  $B$  is the magnetic field in Gauss. Around 1 G, this corresponds to a sensitivity of 0.6216 Hz/mG. Using integrated sensors in proximity to the ions, magnetic fields can be stabilized to much better than 1 mG [6]. Consequently, it is practical to make use of qubit frequencies that are within less than 1 Hz, an otherwise challenging task. For fabricated qubits, such as superconducting circuits, NV centers or quantum dots, the fact that current fabrication methods do not produce the exact same qubit introduces additional complexity [7, 8]. While this is not a fundamental limitation,

relative phase evolution of the qubits needs to be kept track of in these platforms which becomes increasingly difficult as the system size grows. For instance, the two-qubit entangled state

$$|\psi\rangle_{en} = \frac{1}{\sqrt{2}}(|0\rangle_a|1\rangle_b + e^{i\Delta_{ab}t}|1\rangle_a|0\rangle_b) \quad (1.2)$$

evolves with the frequency difference between the participating qubits “a” and “b”,  $\Delta_{ab} = \omega_a - \omega_b$ . As such, for a system of size  $N$ , there are  $O(N^2)$  phases that need to be monitored. More importantly, if the qubit frequencies are subject to fluctuations due to environmental effects, these phase calibration requirements might even prevent maintaining overall coherence properties of the whole system. Hence, the indistinguishability and high levels of isolation of trapped ions from the environment gives them an edge on this aspect of scalability.

Second, a straightforward approach of putting more qubits in close proximity to each other is likely to fail [1] which necessitates a more modular approach for scaling, similar to classical computing architectures, and trapped ions have shown more promising results so far. Each platform has some limitation on the number of controllable qubits achievable within a module. In NV centers, each electron spin has limited number of neighbor nuclear spins that can be used as qubits [4]. Production and calibration of small size superconducting circuit modules that eventually connect to each other might be an easier scaling approach than manufacturing a single chip with many qubits and the required connections. And with trapped atomic ions, simply adding more qubits to the crystal chain is hampered by the increased number of interactions between the qubits that need to be reliably controlled [9]. Also, this

size increase results in slower multi-qubit entangling operations, making them more susceptible to decoherence mechanisms [10]. Increased likelihood of background gas collisions and the resulting destabilization of the ion chain currently limits manageable chains sizes to about 20 [11], and cryogenic traps are being considered to minimize these collisions to push the number close to 100. For these reasons, a modular approach is the way forward [12, 13]; a small programmable quantum computer has recently been demonstrated with trapped atomic ions [14], and such small units can be connected together with re-configurable photonic interfaces to create a network architecture (see Fig. 1.1). In this approach, quantum information is processed at memory qubits while modules are connected by probabilistic entanglement of communication qubits via photon interference [15].

There have been various experiments on different platforms that utilize optical or microwave photons to entangle qubits at a distance [7, 13, 16, 17]. One important parameter in scaling and entanglement propagation in the modular network architecture is the ratio between the average entanglement generation time and the entangled state coherence time. Trapped atomic ions is the only platform to date that has achieved a ratio less than one, and it is three orders of magnitude smaller than the closest platform (see Table. 1.1). As this ratio gets bigger, having multiple modules connected at the same time in the network gets exponentially harder to achieve and might result in unrealistic overhead in the resources required.

These two aspects, the indistinguishability of qubits and the fast generation of entanglement between them compared to the coherence time, make trapped ions attractive for use in a modular network architecture.

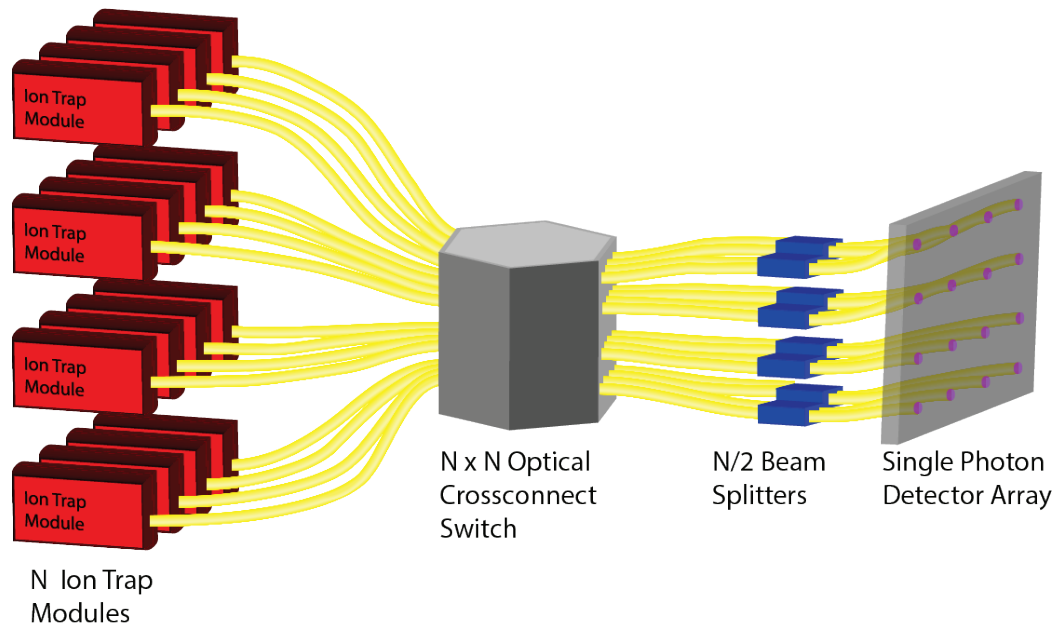


Figure 1.1: In this network architecture, each module holds a manageable number of trapped ions. Entanglement within a module is generated using local Coulomb interactions. Specific ions are assigned as communication qubits within a module; scattered photons from these ions are collected into a  $N \times N$  optical cross-connect switch to link arbitrary modules with each other. Entanglement between communication qubits is heralded by a Bell state measurement on the collected photons using beam splitters and photon detectors.

Platform	entanglement generation (sec)	coherence time (sec)	Ratio ( $x$ )	Overhead ( $x^x$ )
Trapped Ions [13]	0.22	1.12	0.2	0.71
Neutral Atoms [17]	0.1	$2 \times 10^{-4}$	500	$10^{1350}$
Superconducting Circuits [7]	0.005	$6 \times 10^{-6}$	800	$10^{2300}$
NV centers [16]	250	0.01	25000	$10^{100000}$

Table 1.1: Entanglement generation time between qubits that are linked together with photonic interfaces and the coherence time of this entangled state. The ratio between these two numbers ( $x$ ) is a big indication of how scalable a platform is since the probability of successfully connecting multiple modules at the same time gets lower as  $x$  grows. In a modular network, the overhead in resources scale as a super-exponential ( $x^x$ ) for realizing fault tolerant operations [12].

Another promising approach to scaling is through quantum charge-coupled devices where trapped ions are shuttled between trapping zones to bring together short chains of ions for quantum algorithms [18]. Still, complexity of controlling the hardware and optical requirements might limit the size of the system [12].

## 1.2 Multi-Species Modules

Entanglement of remote qubits is the key ingredient in the construction of a modular network. This operation is mediated through the quantum interference of two photons on a beam splitter, and in this section I revisit the underlying theory. The understanding of this mechanism is helpful in characterizing the crosstalk issues related to these entanglement operations in a network architecture, which can be

eliminated by going to a multi-species apparatus.

### 1.2.1 Entanglement of Remote Qubits

The first demonstration of interference between two identical photons impinging on a beam splitter was done by Hong, Ou and Mandel [19]. In this experiment, identical photons incident on two input ports of a 50/50 non-polarizing beam splitter were observed to bunch in either of the output ports. Since photon number resolution is difficult even with current detectors [20], this behavior was usually verified by the absence of coincident detection of photons on separate output ports of the beam splitter.

The operation of a 50/50 beam splitter can be expressed in terms of creation operators [21]. First, a single photon in the  $n^{\text{th}}$  port of the beamsplitter (see Fig. 1.2 (a)) can be obtained by applying operator  $a_n^\dagger$  to the vacuum state;  $|1_n\rangle = a_n^\dagger|0\rangle$ . And, the effect of beam splitter on the photons is described by:

$$\begin{aligned} a_3^\dagger &= \frac{1}{\sqrt{2}}(a_1^\dagger - a_2^\dagger) \\ a_4^\dagger &= \frac{1}{\sqrt{2}}(a_1^\dagger + a_2^\dagger) \end{aligned} \tag{1.3}$$

where the sign difference is due to a low to high index of refraction change for light going from port 2 to 3 [22]. Rewriting these equations:

$$\begin{aligned} a_1^\dagger &= \frac{1}{\sqrt{2}}(a_3^\dagger + a_4^\dagger) \\ a_2^\dagger &= \frac{1}{\sqrt{2}}(a_4^\dagger - a_3^\dagger) \end{aligned} \tag{1.4}$$

we can theoretically recreate the first interference experiment. For instance, when

two identical photons are incident on the input ports 1 and 2:

$$\begin{aligned}
|1_1 1_2\rangle &= a_1^\dagger a_2^\dagger |0\rangle \\
&= \frac{1}{2}(a_3^\dagger + a_4^\dagger)(a_4^\dagger - a_3^\dagger)|0\rangle \\
&= \frac{1}{2}(a_4^\dagger a_4^\dagger - a_3^\dagger a_3^\dagger)|0\rangle \\
&= \frac{1}{\sqrt{2}}(|0_3 2_4\rangle - |2_3 0_4\rangle).
\end{aligned} \tag{1.5}$$

With this simple analysis, it is evident that the photons bunch at either of the two output ports of the beam splitter, and detectors placed at output ports 3 and 4 would not register at the same time assuming the incident photons are identical. Another note of importance is that, here the photons are assumed to be in a single state, or a single mode; hence only one set of creation operators is used. Identical photons that are in a superposition of states do not necessarily exhibit this bunching behavior as will be shown.

In principle, states that carry extra information can be distinguished from each other in the lab. For example, perpendicular polarized photons can be separated using a polarizing beam splitter, or cavities can be used to differentiate between different frequency photons. Hence, introduction of another set of operators is necessary if photons incident on a 50/50 beam splitter are in such a superposition.

We utilize these extra degrees of freedom for entanglement of remote qubits. In this technique, a photon is first entangled with its parent atom [23]. Orthogonal sets of horizontal and vertical polarization states  $\{|H\rangle = a^\dagger|0\rangle, |V\rangle = b^\dagger|0\rangle\}$  are used for transferring the information, resulting in a joint atom-photon state:

$$|\psi\rangle = |\downarrow H\rangle + |\uparrow V\rangle \tag{1.6}$$

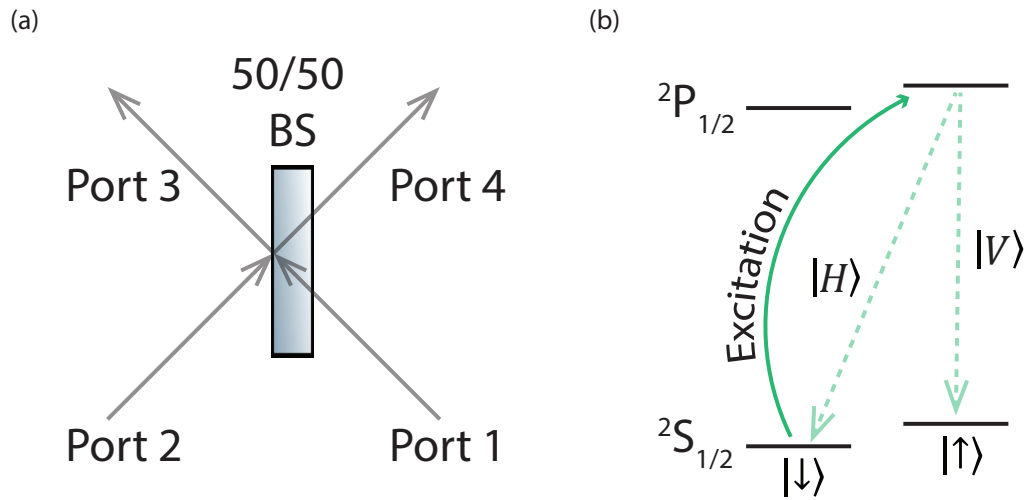


Figure 1.2: (a) A 50/50 non-polarizing beam splitter, with two input (1 and 2) and two output (3 and 4) ports. The reflection happens inside the material from port 1 to 4 and in the air from port 2 to 3, introducing a  $\pi$  phase shift to the field. (b) Basic principle of generation a photon entangled with its parent atom. The atoms are initialized to a pure state with optical pumping beams and another field drives a dipole transition to excited level afterwards. Atom decays back to ground state levels emitting a photon where the timescale is determined by the lifetime of the excited level. The polarization state of this photon and the spin state of the atom get entangled in the process. Capture and detection of these photons from two separate qubits at the same trial cycle is required for entanglement generation between them.

where I ignore normalization for simplicity in the rest of these calculations and the procedure of creating this atom-photon entangled state is shown in Fig. 1.2 (b).

Then, the joint state of two such pairs is:

$$\begin{aligned} |\psi\rangle_1 \otimes |\psi\rangle_2 &= (|\downarrow H\rangle + |\uparrow V\rangle)_1 \otimes (|\downarrow H\rangle + |\uparrow V\rangle)_2 \\ &= |\downarrow\downarrow HH\rangle + |\downarrow\uparrow HV\rangle + |\uparrow\downarrow VH\rangle + |\uparrow\uparrow VV\rangle. \end{aligned} \quad (1.7)$$

Without loss of generality, we can rewrite this joint state in terms of entangled atom and photon Bell states:

$$\begin{aligned} |\psi^+\rangle &= |HV\rangle + |VH\rangle & |\psi^-\rangle &= |HV\rangle - |VH\rangle \\ |\phi^+\rangle &= |HH\rangle + |VV\rangle & |\phi^-\rangle &= |HH\rangle - |VV\rangle \end{aligned} \quad (1.8)$$

for photons and similarly:

$$\begin{aligned} |\psi^+\rangle &= |\downarrow\uparrow\rangle + |\uparrow\downarrow\rangle & |\psi^-\rangle &= |\downarrow\uparrow\rangle - |\uparrow\downarrow\rangle \\ |\phi^+\rangle &= |\downarrow\downarrow\rangle + |\uparrow\uparrow\rangle & |\phi^-\rangle &= |\downarrow\downarrow\rangle - |\uparrow\uparrow\rangle \end{aligned} \quad (1.9)$$

for atoms. Then, the joint state in Eqn. 1.7 expressed with these Bell states is:

$$|\psi\rangle_1 \otimes |\psi\rangle_2 = |\psi^+\rangle_a |\psi^+\rangle_p + |\psi^-\rangle_a |\psi^-\rangle_p + |\phi^+\rangle_a |\phi^+\rangle_p + |\phi^-\rangle_a |\phi^-\rangle_p \quad (1.10)$$

where “a” and “p” subscripts denote atom and photon respectively. The effect of beam splitter on photonic Bell states impinging from ports 1 and 2 can be seen using Eqn. 1.4:

$$\begin{aligned} |\psi^+\rangle &= (a_1^\dagger b_2^\dagger + b_1^\dagger a_2^\dagger)|0\rangle \\ &= (a_4^\dagger b_4^\dagger - a_3^\dagger b_3^\dagger)|0\rangle \\ &= |0_3(HV)_4\rangle - |(HV)_3 0_4\rangle \end{aligned} \quad (1.11)$$

where we observe photon bunching of orthogonal polarization states in either output ports with equal probability. In contrast,  $|\psi^-\rangle$  anti-bunches:

$$\begin{aligned}
|\psi^-\rangle &= (a_1^\dagger b_2^\dagger - b_1^\dagger a_2^\dagger)|0\rangle \\
&= (a_3^\dagger b_4^\dagger - b_3^\dagger a_4^\dagger)|0\rangle \\
&= |H_3V_4\rangle - |V_3H_4\rangle
\end{aligned} \tag{1.12}$$

and photons get separated to different ports. To complete the set of equations for all four Bell states:

$$\begin{aligned}
|\phi^+\rangle &= (a_1^\dagger a_2^\dagger + b_1^\dagger b_2^\dagger)|0\rangle \\
&= (a_4^\dagger a_4^\dagger - a_3^\dagger a_3^\dagger + b_4^\dagger b_4^\dagger - b_3^\dagger b_3^\dagger)|0\rangle \\
&= |0_3(HH)_4\rangle - |(HH)_30_4\rangle + |0_3(VV)_4\rangle - |(VV)_30_4\rangle \\
|\phi^-\rangle &= (a_1^\dagger a_2^\dagger - b_1^\dagger b_2^\dagger)|0\rangle \\
&= (a_4^\dagger a_4^\dagger - a_3^\dagger a_3^\dagger - b_4^\dagger b_4^\dagger + b_3^\dagger b_3^\dagger)|0\rangle \\
&= |0_3(HH)_4\rangle - |(HH)_30_4\rangle - |0_3(VV)_4\rangle + |(VV)_30_4\rangle
\end{aligned} \tag{1.13}$$

resulting another bunching outcome, in which same polarization states emerge from same output port.

As shown in Fig. 1.3, measurement on these photons can be carried out using polarizing beam splitters (PBS) in conjunction with detectors, such as photo multiplier tubes (PMT's). Importantly, the outcomes for distinct impinging Bell states give different coincident detection result, which allows us to do a Bell state measurement on the joint photonic wave function. This in turn, projects the atomic state of two qubits into an entangled state (see Eqn. 1.10). Only two out of the total

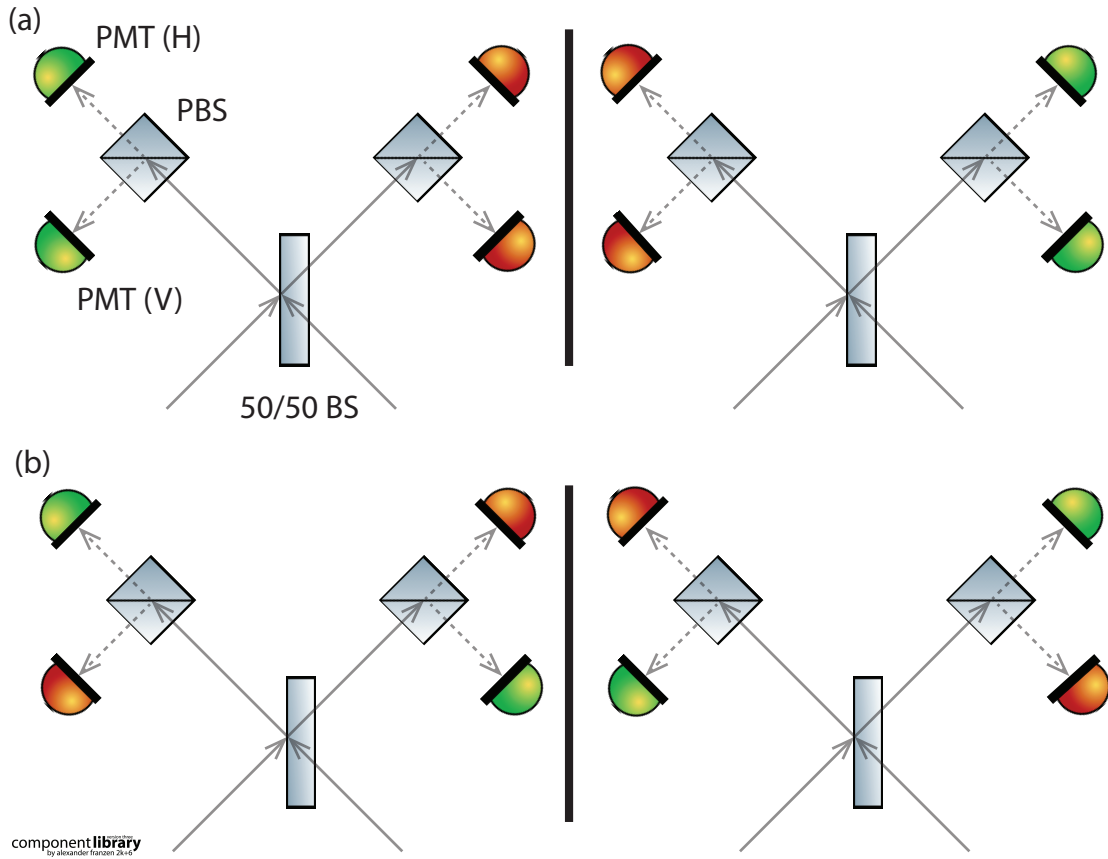


Figure 1.3: Polarizing beam splitters (PBS) can be used at the output ports of a 50/50 beam splitter to distinguish  $|H\rangle$  and  $|V\rangle$  photons, where PMT(H)[PMT(V)] detects  $|H\rangle[|V\rangle]$ . (a) An incoming  $|\psi^+\rangle$  polarization state has two orthogonal polarization states leaving the same output port of the beam splitter as can be seen from Eqn. 1.11, which is later split apart by the PBS. Hence, coincident detection events on the same output port side projects the atomic qubits to  $|\psi^+\rangle$ . (b) Coincident detection events involving different output ports with different polarization states result in projection of atoms to  $|\psi^-\rangle$  (see. Eqn. 1.12). Incoming photonic  $|\phi^\pm\rangle$  states leave from same output port with same polarization state (see. Eqn. 1.13), hence these states are not misinterpreted as  $|\psi^\pm\rangle$

four Bell states can be measured with this setup, since even with photon number resolving detectors,  $|\phi^+\rangle$  and  $|\phi^-\rangle$  cannot be distinguished from each other as they only differ by a phase factor. However, it is still possible to distinguish all four Bell states if photons are entangled in more than one degree of freedom (hyperentangled state) [24]. The probabilistic nature does not affect the purity of entangled state, as we post-select events where only two photons are detected, giving the commonly used “heralded entanglement” name to this procedure [15].

### 1.2.2 Entanglement Generation Probability

In this heralded scheme, the successful generation of entanglement between remote qubits depends on coincident collection and detection of photons from the atoms. Hence, a large number of trials might be necessary until a successful event happens. Considering  $^{171}\text{Yb}^+$  qubits [13], we can characterize this entanglement probability looking at several factors that are involved:

$$P_{\text{Ent}} = \frac{1}{2} (P_{\text{br}} P_{\text{CG}} \left(\frac{\Omega}{4\pi}\right) P_{\text{fc}} P_{\text{qe}} P_{\text{loss}})^2 \quad (1.14)$$

where branching ratio ( $P_{\text{br}} = 0.995$ ) and Clebsch-Gordon coefficients ( $P_{\text{CG}} = \frac{2}{3}$ ) amount to the generation probability of the single photon of interest after atom excitations while collection solid angle ( $\frac{\Omega}{4\pi} = 0.1$ ), fiber-coupling fraction ( $P_{\text{fc}} = 0.2$ ), photon detector quantum efficiency ( $P_{\text{qe}} = 0.35$ ) and losses in the system ( $P_{\text{loss}} = 0.95$ ) accounts for detection of these photons. The overall  $\frac{1}{2}$  factor comes from the number of detectable Bell states, and the probability numbers are squared since two photons from each atom needs to be collected and detected during the same

experimental trial. The largest number for  $P_{\text{Ent}}$  ever achieved with trapped atomic ions was the  $10^{-5}$  [13] measured in our lab. Along with the  $\sim 500$  kHz experimental repetition rate, an average entanglement generation rate of  $\sim 5 \text{ s}^{-1}$  was achieved. Optimistically, this rate can be pushed to  $\sim 500\text{--}5000 \text{ s}^{-1}$  range with improvements on fiber coupling and detector efficiencies.

### 1.2.3 Crosstalk Considerations

After looking at the basic principles of entanglement generation between remote qubits and factors that determine number of trials required to create this entangled state, we can now better understand the problems that might stem from these operations in a modular network architecture.

In this setup (see Fig. 1.4), processing of quantum information and protection of coherence on memory qubits while trying to entangle photonic qubits is required for maximum utilization of resources. Hence, it is important to eliminate crosstalk processes between them; excitation and optical pumping beams used in heralded entanglement schemes or photons emitted by the communication qubits might be absorbed by the memory atoms and result in corruption of the stored information. In this section, the specific case of  $^{171}\text{Yb}^+$  qubits will be considered with hyperfine clock states utilized for storing/processing information and a heralded entanglement scheme relying on polarization encoding [13, 25].

At a distance of  $r$  between the photonic qubit and the nearest memory qubit,

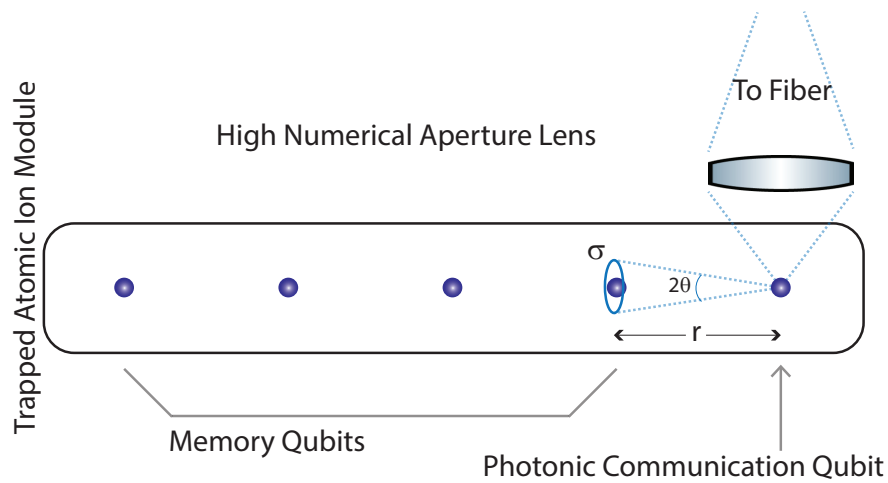


Figure 1.4: A trapped atomic ion module; the unit cell of network architecture. Photons emitted from communication qubits are collected into a single-mode fiber to be used in heralded entanglement of qubits in different modules. However, these photons get emitted towards the memory qubits as well, and might be absorbed, resulting in loss of information. Addressing only the photonic atoms with excitation and optical pumping beams for heralded entanglement operation while not affecting the memory qubits might be challenging as well. These crosstalk processes between memory and communication qubits might compromise the quantum information processing if they are close to each other.

the apex angle of the cone that covers the resonant absorption cross section is:

$$2\theta(r) = 2\text{Arctan}\left(\frac{\sqrt{3\lambda^2/2\pi^2}}{r}\right) \quad (1.15)$$

and, the ratio of the resulting solid angle to the total area is:

$$\frac{\Omega}{4\pi} = \frac{2\pi \int_0^\theta \sin \theta' d\theta'}{4\pi} = \frac{1 - \cos[\theta(r)]}{2}. \quad (1.16)$$

Probability of photon absorption by the memory qubit is proportional to this ratio. However, there are two other factors that need to be included as well. First, the polarization state and the frequency of the emitted photons affect how strongly they can disturb the memory qubits, which amounts to a factor of  $\sim \frac{1}{3}$ . Second, photons are emitted from communication atoms with an exponential decaying temporal envelope [26], which could only result in a maximum excitation probability of 0.54 on memory atoms from these photon wave packets [27]. Including these factors, the crosstalk probability from these stray photons scale as:

$$P_{\text{ct\_stray}}(r) \approx \frac{1}{6} \frac{1 - \cos[\theta(r)]}{2}. \quad (1.17)$$

Another crosstalk source is the individual beams needed to address the communication qubit; the optical pumping beam for state initialization and the excitation light to create single photons. To reduce these effects, the waist of the beam addressing the communication qubit needs to be minimized. The intensity of the light present at a distance  $r$  from photonic atom site can be found by assuming a Gaussian beam shape of center intensity  $I_0$  and waist  $w_0$ :

$$I(r) = I_0 e^{\frac{-2r^2}{w_0^2}}. \quad (1.18)$$

The ratio of the photon scattering rate at the origin and at a distance  $r$  can be used to calculate the crosstalk probability:

$$P_{\text{ct.beams}}(r) = \frac{\Gamma(r)}{\Gamma(0)} = \frac{s(r)/(1+s(r))}{s(0)/(1+s(0))} \quad (1.19)$$

where  $s(r) = \frac{I(r)}{I_{\text{sat}}}$  and the beam is assumed to be on resonance. Setting  $I_0 = I_{\text{sat}}$ , the excitation probability of an atom at distance  $r$ , while the atom at beam center scatters a single photon is:

$$P_{\text{ct.beams}}(r) = \frac{2e^{-\frac{2r^2}{w_0^2}}}{1 + e^{-\frac{2r^2}{w_0^2}}} . \quad (1.20)$$

Fig. 1.5 shows plots of two crosstalk mechanisms calculated in Eqn. 1.17 and 1.20.

Even with two orders of magnitude improvement on entanglement generation probability, it is evident from Fig. 1.5(b) that, crosstalk might introduce considerable errors with typical atom separations of a few microns in trapped ion modules. Introduction of a different atomic species as the communication qubit can eliminate the crosstalk issues if the excitation and emitted light is far from any optical resonance of the memory qubits [28]. This claim is verified in our multi-species apparatus by showing that the coherence time of  $^{171}\text{Yb}^+$  qubit is not affected by a nearby single photon source at a different resonance frequency or the laser field itself that drives the dipole transition of the nearby atom. This experiment incorporated a Ramsey measurement on  $^{171}\text{Yb}^+$  while Doppler cooling beams were incident on the  $^{138}\text{Ba}^+$  atom to scatter many photons.

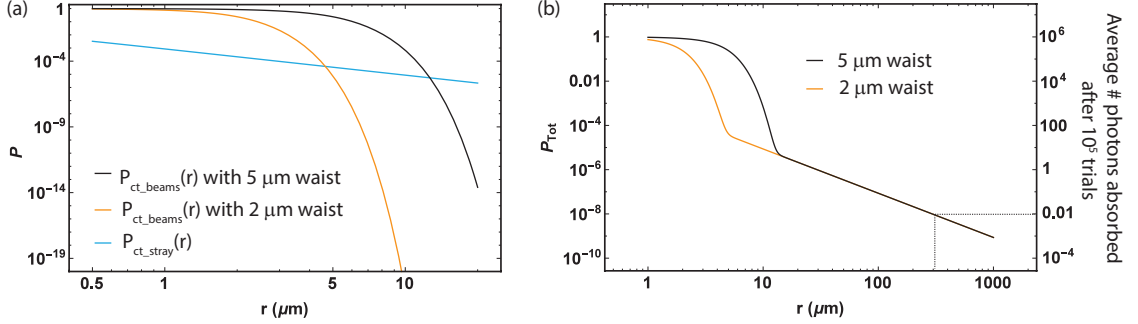


Figure 1.5: (a) Probability of photon absorption versus atom spacing. For these calculations,  $^{171}\text{Yb}^+$  atoms are considered. At close distances, the addressing beams dominate the crosstalk effects. However, intensity at the tails of these Gaussian beams quickly diminish and the stray photon contribution becomes the significant factor. Curves for beams with 2 and 5  $\mu\text{m}$  waists are shown. (b) Total probability of photon absorption from these two mechanisms,  $P_{\text{Tot}} = P_{\text{ct.stray}} + P_{\text{ct.beams}}$ , versus average number of photons absorbed at a distance  $r$  after  $10^5$  trials,  $\bar{p}(r) = P_{\text{Tot}}(r) \times 10^5 \times 10$ . The factor of  $10^5$  is used here to match the number of trials it took to entangle the remote qubits in our experiment [13]. The factor of 10 accounts for the approximate number of photons that needed to be scattered from the communication qubit for each trial. While we use single photons for entanglement generation, optical pumping to a pure state introduces these extra photons. Single photon absorption would result in total loss of information, hence the right axis can be considered as crosstalk errors as well. As shown, to reduce the errors caused by crosstalk below 1% levels, the photonic atom needs to be separated from memory atoms by more than 300  $\mu\text{m}$ .

## 1.2.4 Additional Advantages of a Multi-Species Setup

In addition to solving the crosstalk problem, introducing a different species of atom might enable extra features to a trapped ion module. The second species can be used as refrigerant atoms to cool memory qubits [29] allowing for higher fidelity quantum operations. Importantly, the coherence properties stored in the memory qubits would not be affected by this operation, making it possible to execute more quantum logic gates which might be necessary for realizing specific algorithms [14].

Attractive properties of each atom can be taken advantage of for certain tasks as well. For example, atoms that are less susceptible to external noise sources might be better suited as memory qubits with their long coherence times [30]. At the same time, atoms that have strong photon emission lines in the visible or infrared bands would be more advantageous for use as photonic communication qubits, benefiting from less attenuation on optical fibers to extend the networks to larger distances [31] and higher quantum efficiency photon detectors [32] for increased entanglement generation rates on modular architectures.

## 1.2.5 Multi-Species Network Architecture

The scaling approach with multi-species modules is shown in Fig. 1.6. After entanglement of photonic link  $^{138}\text{Ba}^+$  qubits, the information is transferred to nearby memory  $^{171}\text{Yb}^+$  qubits using the Coulomb interaction between them. This effectively transfers the entanglement to memory qubits and increases the number of connected processor atoms to scale up the system size. The operations required for realizing

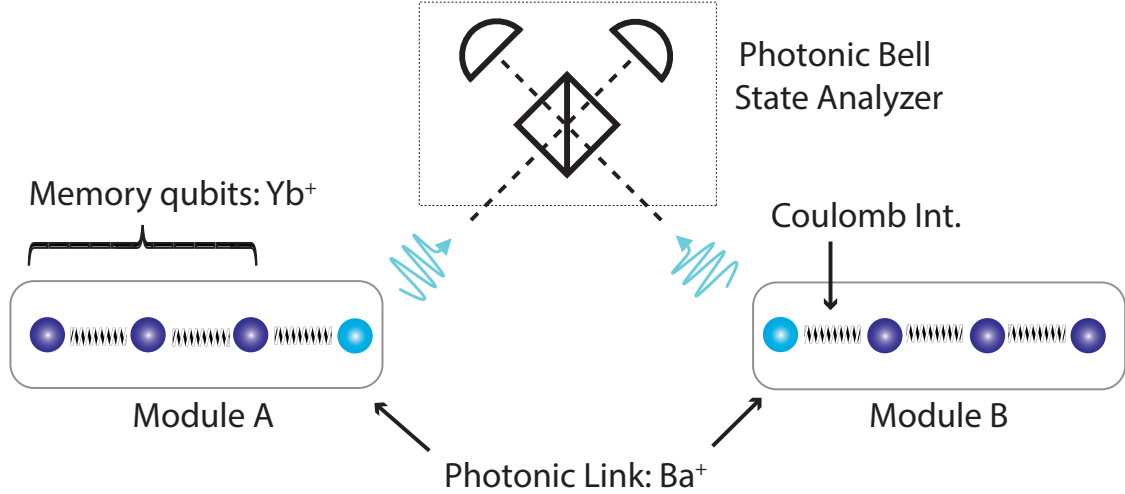


Figure 1.6: Different modules are connected by first entangling the  $^{138}\text{Ba}^+$  qubits using flying photon qubits. After successful connection, the Coulomb interaction between  $^{171}\text{Yb}^+$  and  $^{138}\text{Ba}^+$  atoms can be utilized for transferring information from the photonic link to memory qubits.

this goal has been experimentally demonstrated and the results are shown later in this thesis.

### 1.3 Previous Experiments

In the first three and a half years in the Monroe group, I have been a part of various experiments. The first experiment involved combining photonic and phononic entanglement operations on a unit cell of modular architecture [13]. The aim on this experiment was showing the validity of the modular scaling approach by combining these different entanglement operations. Another important aspect was addressing the requirement of faster timescale on creating entanglement than phase coherence time of the entangled state.

Afterwards, we showed that phase coherence on this network architecture can

be maintained over space and time by using phase locking techniques [33], and this is a critical requirement for scaling. Finally, we have shown how distinguishable quantum memories can be entangled [34]. Even though trapped atomic ions can be made identical with little effort, the techniques shown here can be beneficial on other platforms where manufactured qubits might have non-identical frequencies.

Details on these experiments can be found on Refs. [13,33–35] and rather than repeating the results and experimental considerations here, the focus of this thesis will be on the multi-species apparatus.

## Chapter 2: Experimental Setup

This thesis work has been conducted on an optical table with a long history which produced many doctorate degrees. Hence, the details about certain aspects of experimental setup are covered throughly in accompanying theses [35–37], where only  $^{171}\text{Yb}^+$  qubits were employed. However, a major renovation took place in the last two years to accommodate another species of atom. As such, in this chapter I will briefly describe the setup and mainly focus on the details that came into existence with inclusion of the second atomic species.

### 2.1 RF Paul Traps and Vacuum Chamber

We use RF Paul traps to hold onto positively charged atomic ions [38]. The experimental demonstrations done in this thesis work was realized in four-rod [36] and segmented blade [35] traps (see Fig. 2.1). Even though these hand assembled traps are primitive compared to fabricated traps with many electrical connections [39, 40], which are more suitable for complex shuttling procedures, allocating different zones for various operations or shaping trapping potentials for equal spacing of ions, such complexity was not required as experiments done so far only involved a maximum number of two co-trapped ions. On the contrary, the hand assembled traps used

in this thesis work were better suited for the experiments conducted here. They utilize two separate large optical access view-ports, which is convenient as one port is mainly used for photon collection during heralded entanglement procedures, while the other port is used for state detection of qubits and trapped ion imaging. Recently, high optical access requirements started to be considered in fabricated trap technologies, for example the Sandia HOA 2.0 trap [41], and will likely make hand assembled traps obsolete in the near future.

To minimize the background gas collisions with the trapped ions, a high vacuum environment is needed. The procedures for reaching  $10^{-11}$  Torr levels involve baking the vacuum chamber enclosure and the RF Paul trap installed for several days after initial cleaning procedures. These steps are investigated in greater detail in Ref. [35, 36].

## 2.2 Ytterbium and Barium Atomic Ions

### 2.2.1 Overview

As mentioned before, the past experiments conducted in my project used only  $^{171}\text{Yb}^+$  atomic ions as qubits. Other research projects in the Monroe group are also exclusively utilizing  $^{171}\text{Yb}^+$  in their experiments [14, 42, 43].  $^{171}\text{Yb}^+$  ions are attractive in quantum information processing with long coherence times [5], convenient high fidelity state detection schemes [44] and easy manipulation with external fields [45]. However, UV photons emitted from the ions are not well suited for remote entanglement schemes with current optical fiber and detector technologies. Addi-

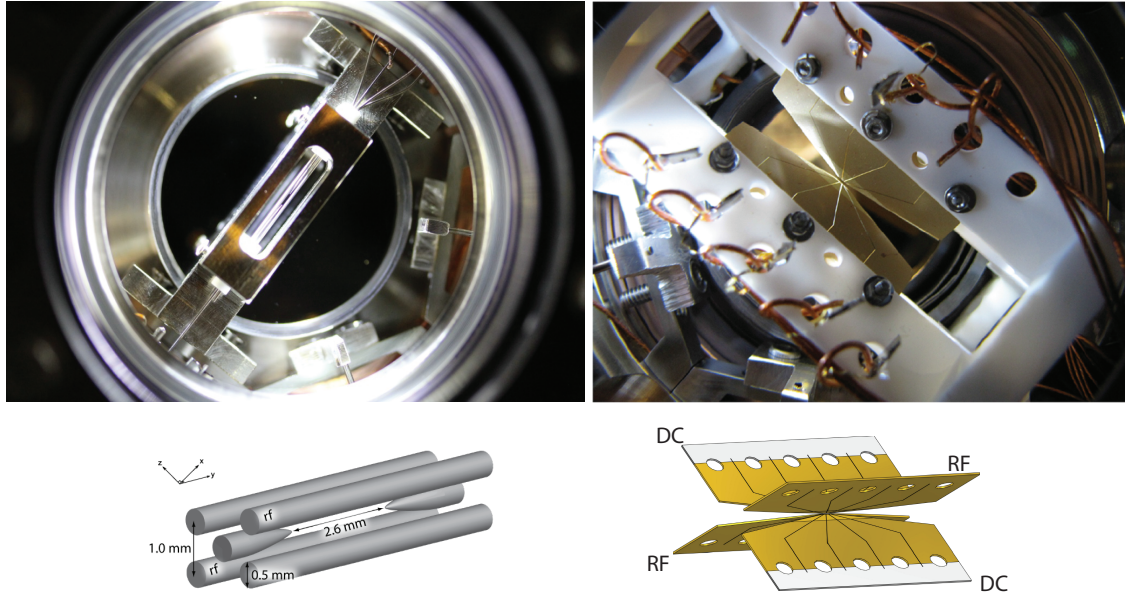


Figure 2.1: The RF Paul traps used in this thesis work are constructed with four rod (left) and segmented blade (right) structures. Four tungsten rods are held with an alumina spacer with holes and two needles in the middle section provide confinement in longitudinal axis with DC voltages. In the segmented blade trap, alumina plates are laser machined and coated with gold. Segments allow application of different DC voltages to shape the longitudinal confinement potential for changing the ion spacings. In these traps, the typical applied RF field is  $\sim 100\text{-}1000$  V in the 10-40 MHz range where helical resonators are used to create these high voltage and high frequency fields. Due to larger separations between the needles, the applied DC voltages are considerably higher in four rod trap compared to segmented blade trap to achieve similar axial confinement. Application of 200 V on both needles results in a longitudinal mode frequency of  $\sim 1$  MHz in four rod trap while it only requires  $\sim 10$  V on the outermost segments of the blade trap to achieve this mode frequency.

tionally, due to issues and in view of advantages indicated in the previous chapter, we have introduced another atomic species.

We decided on barium atomic ions as photonic communication qubits for several reasons. First,  $^{138}\text{Ba}^+$  atoms have strong emission lines at 493 nm and 650 nm wavelengths, deeper in the visible range compared to other available atomic species. These photons can be sent longer distances with less attenuation in fibers for a large scale distributed quantum networks. Single photon avalanche diodes (SPAD) and superconducting nanowire single-photon detectors (SNSPD) are commercially available and can reach up to 90% detection efficiencies at these wavelengths, increasing the entanglement generation rate between remote qubits. Second, since  $^{138}\text{Ba}^+$  is close to  $^{171}\text{Yb}^+$  in mass, we can co-trap these ions with same RF field, without resorting to application of multiple RF fields which might be necessary for widely different massed species [46]. Lastly, the simple atomic structure of  $^{138}\text{Ba}^+$  would make photon generation schemes easier for entanglement operations between different modules and sympathetic cooling of memory qubits for achieving longer quantum information processing times. One disadvantage of these qubits is their short coherence times as qubit states are encoded on the electron spin which is more susceptible to magnetic field noise compared to hyperfine states. However, this does not pose a big problem since entanglement between  $^{138}\text{Ba}^+$  qubits will be readily transferred to memory qubits where this entanglement can be preserved for longer periods. I will revisit these points more in detail later.

## 2.2.2 Neutral Sources and Photo-ionization

We load the ions into the trap by first heating a source of neutral atoms to create a flux in the trapping region, and then photo-ionize them on the spot. For ytterbium sources, a few milligrams of material is filled into a hypodermic needle oven which is pointed towards the trapping region and a 3-4 A of current is passed through to heat it up [36]. In contrast to ytterbium, barium rapidly oxidizes when it is exposed to air, which makes putting a pure source into the vacuum chamber a challenging task. A few different procedures were tried to minimize this oxidization.

Initially, a stainless steel tube filled with barium and closed with an indium seal in an argon environment was tried as a source (purchased from Alvatec). The first time we have tried this in a vacuum chamber, the indium seal was simply melted off by running a small current (2 A), benefiting from a low melting point of 156 °C, and barium source became available. However, following the same procedure resulted in mixed results in subsequent trials for constructing another ion trap, ranging from splattering of melted indium to shooting it off as a chunk. We attributed this to pressure gradient across the seal due to argon gas on one side and vacuum on the other, which means the initial source oven installed in the ion trap might have had a defective seal. This would also explain the long period of unsuccessful  $^{138}\text{Ba}^+$  trapping trials we have experienced, where a thick barium oxide layer might have been present and needed to be depleted first.

We have also tried another way of removing the indium seal by snipping it off in an argon rich environment. While eventually we were able to trap using this

source, we had a hard time trapping initially. Eventually getting the oven red hot to melt the source in the hopes of dissipating any oxide layer that might be blocking the elemental source resulted in successful loading on this second ion trap.

Compared to these Alvatec ovens, a more traditional approach of quickly putting barium inside a previously aligned oven tube in an argon rich environment, and keeping the source at elevated temperatures during vacuum chamber bake-out might work better. Nevertheless, the search for a reliable pure barium source installation is still in progress. One particular solution might use getter materials, where barium is emitted from the material (BaAl4) at high temperatures while the alloy prevents the oxidization of barium in air. Maintaining a directional neutral flux is the main hurdle in this setup. Another approach might be using platinum filaments implanted with barium [47]. Due to work function and ionization energy differences, barium directly gets released as ions when a filament is heated. Directing ions to the trap might pose a problem here as well, but recently this idea has been revisited and different isotopes of barium ions were successfully loaded in Wes Campbell's group at UCLA.

After a flux of neutral atoms in the trapping region is maintained, these atoms are photo-ionized with lasers. A 399 nm laser tuned to the  $^1S_0 \rightarrow ^1P_1$  transition of neutral Yb excites the atom and another photon from the 369 nm laser finalizes the photo-ionization process [36].

For loading  $^{138}\text{Ba}^+$ , we have looked into commonly used schemes (see Fig. 2.2) and ultimately decided to use a 413 nm laser for loading in our apparatus. This method only required the addition of one more readily available laser to the setup.

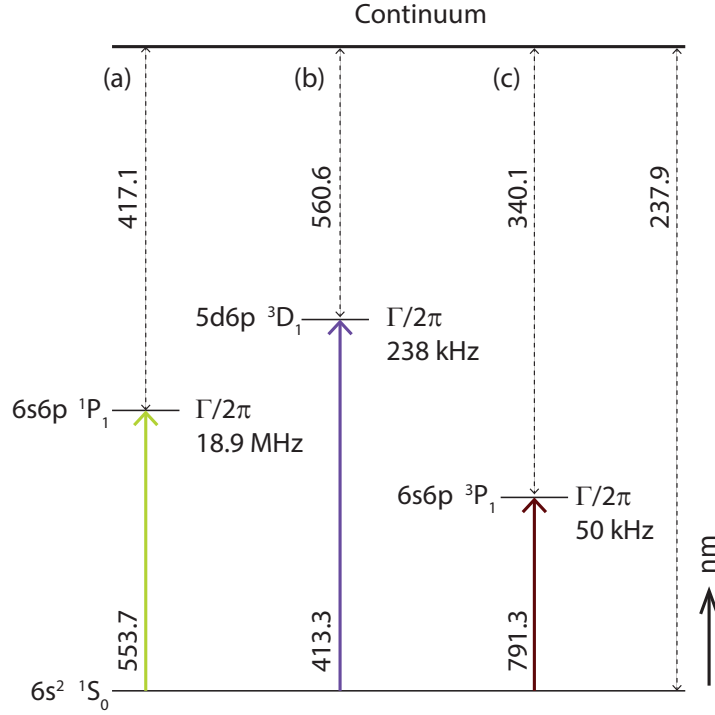


Figure 2.2: Energy level diagram of neutral barium drawn to scale. Wavelengths and natural linewidths are cited from Ref. [48, 49] and dashed lines show the maximum wavelength that can be used for the second part of the photo-ionization process (a) A strong dipole allowed transition is excited with a 553 nm laser and another with less than 417 nm wavelength, which is already available for  $^{171}\text{Yb}^+$  qubits, can be used for excitation to the continuum [50]. However, the lack of laser diodes around 553 nm make this scheme costly and impractical, as dye lasers or doubling from 1106 nm would be necessary. (b) A weak intercombination line is utilized in this method [51], and another 413 nm photon from the same laser has enough energy to complete the photo-ionization process. (c) Another method [52] involving a weaker intercombination line which requires an extra UV source as well, making it less appealing compared to (b).

In the ionization process,  $\sim 2$  mW of 413 nm laser beam is focused at the center of the trap with a waist of  $\sim 10$   $\mu\text{m}$ . We have noticed that, to trap  $^{138}\text{Ba}^+$ , the required flux from the barium oven is much more than is necessary for trapping  $^{171}\text{Yb}^+$ , as evidenced by the pressure reading in the vacuum chamber. With current running through the barium oven, we see pressures climbing from  $10^{-11}$  up to  $10^{-9}$  Torr where we start to see non negligible photo-ionization rates of a few per minute. Whereas, while trapping  $^{171}\text{Yb}^+$ , the pressure jump is less than  $10^{-11}$  Torr. This difference might be due to natural linewidth differences in the first excitation step of photo-ionization process, or there might be a considerable amount of oxide components in the barium source, reducing the percentage that can be photo-ionized and necessitate a higher flux.

### 2.2.3 Methods for Getting Fluorescence Photons from Barium Ions

Rather than looking directly at the  $^{138}\text{Ba}^+$  fluorescence for the initial verification of loading these ions, we followed an indirect path by first verifying the presence of these ions and afterwards trying to find the correct beam alignment and wavelengths for addressing the transitions.

#### 2.2.3.1 Co-trapping for Verification of $^{138}\text{Ba}^+$ Loading

After loading an  $^{171}\text{Yb}^+$  ion into the trap, we first tried to co-trap a  $^{138}\text{Ba}^+$  by heating the neutral source and aligning the 413 nm photo-ionization beam along the middle of the trap and directly looked for a shift on the  $^{171}\text{Yb}^+$  ion position to

verify presence of an extra ion in the trap. The 413 nm wavelength starting point was obtained from past works [48, 51] and also corrections were made to account for the Doppler shift due to the angle between the neutral flux direction and the photo-ionization beam. Finding the absolute transition frequency is not a critical requirement in this step, as the dispersion of the neutral flux broadens the transition.

One particular anecdote is worthwhile to point out here. Initially we tried this approach while the  $^{171}\text{Yb}^+$  was fluorescing. Collisions due to flux from the barium source when the  $^{171}\text{Yb}^+$  ions are in the excited state has been observed to get them to the long lived  $^2F_{7/2}$  state. To bring the ions back to fluorescing levels, a 355 nm laser was also incident on the  $^{171}\text{Yb}^+$ . However, the first ion trapped with this method was actually verified from motional spectroscopy to be a  $\text{BaO}^+$  molecule. We attributed this to the presence of a 355 nm laser which might have been stripping electrons from the trap electrodes that collide with neutral source to ionize them, or directly driving optical transitions on BaO for photo-ionization. To prevent this issue, during  $^{138}\text{Ba}^+$  trapping trials, we blocked the 369 nm beams to make sure  $^{171}\text{Yb}^+$  is not excited and consequently do not end in the  $^2F_{7/2}$  state. After pressure levels go back to normal values of around  $10^{-11}$  Torr, the 369 nm beam is unblocked to check the presence of any extra ion that might have been added in the process.

With trials around the guess value of the 413 nm transition including a  $\sim 1$  GHz of Doppler shift, the optimal loading point was found at 725.25980 THz, which is consistent with reference point of 725.25890 THz [48].

### 2.2.3.2 $^{138}\text{Ba}^+$ Transition Wavelength Measurements with HCL

After the co-trapping verification, fluorescence measurements are the next step. Even though transition wavelengths for  $^{138}\text{Ba}^+$  can be found from previous works [48,51], calibration differences might introduce significant variations. For this reason, we have directly measured these wavelengths using the optogalvanic effect in a hollow cathode lamp (HCL) following techniques demonstrated in Ref. [53]. Fig. 2.3 shows the setup for this measurement and the results.

Using the transition frequencies obtained with this method as a starting point, fluorescence counts were able to be seen from a single  $^{138}\text{Ba}^+$  ion by scanning around these frequency regions to find them more precisely.

A more complete level structure of the  $^{138}\text{Ba}^+$  ion is shown in Fig. 2.4. Since the  $^2S_{1/2}$ ,  $^2P_{1/2}$  and  $^2D_{3/2}$  form a closed 3 level  $\Lambda$  configuration, two lasers addressing the transitions between them is sufficient for fluorescence, Doppler cooling and some of the qubit operations that will be covered in following chapters.

## 2.2.4 The Optical Bloch Equations

For the fluorescence considerations, the  $^{171}\text{Yb}^+$  atom can be treated as a two level system since branching from  $^2P_{1/2}$  to  $^2D_{3/2}$  is negligible and the deshelving laser does not directly couple back to the  $^2P_{1/2}$  level to bring the population back to the cycling transition of  $^2S_{1/2} \leftrightarrow ^2P_{1/2}$ .

In contrast, a  $\Lambda$  configuration prevents carrying out a similar approach in the  $^{138}\text{Ba}^+$ . For a full characterization of interaction between a single  $^{138}\text{Ba}^+$  ion and

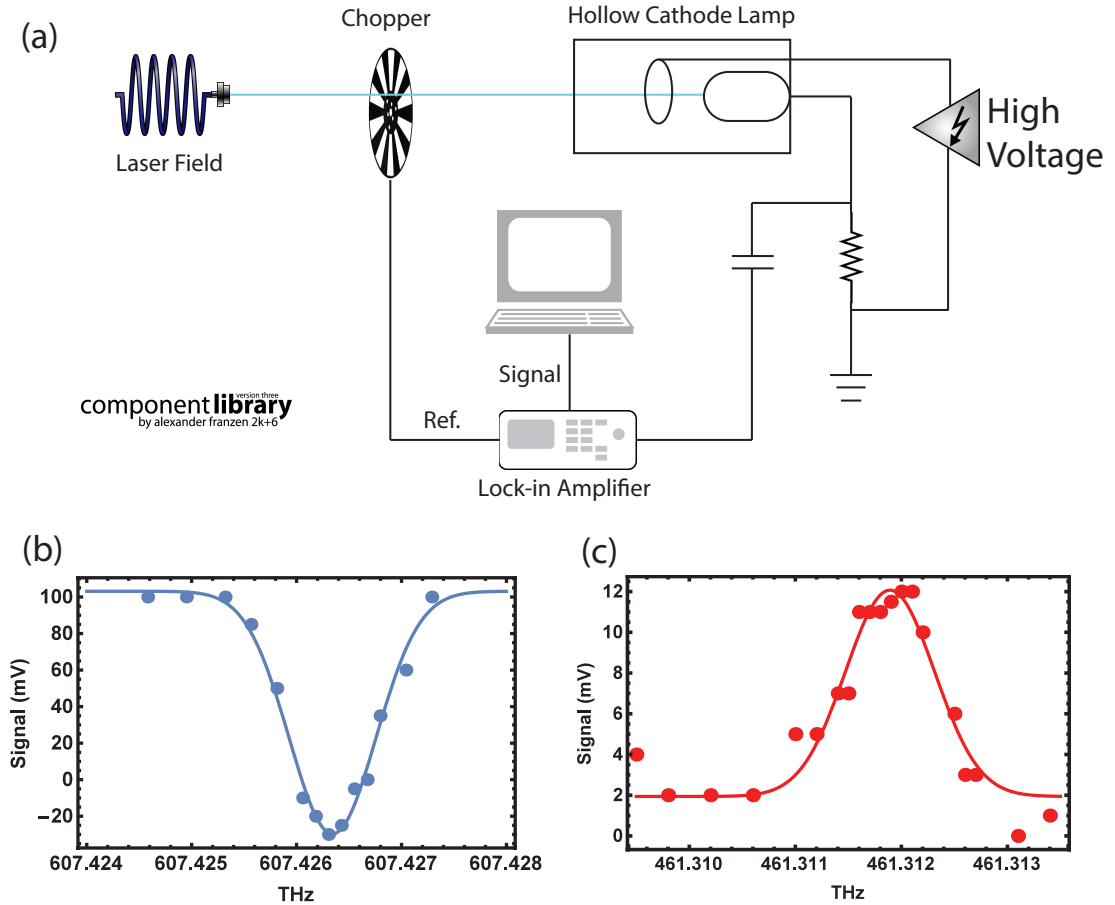


Figure 2.3: (a) The conductivity of the discharge gas changes when an optical transition is excited [53], resulting in a voltage change which can be measured to find these transitions. Using this method, we have measured (b)  $^2S_{1/2} \rightarrow ^2P_{1/2}$  and (c)  $^2D_{3/2} \rightarrow ^2P_{1/2}$  transition wavelengths of the  $^{138}\text{Ba}^+$  ion, finding the center of transition at 607.42634 THz (493.54536 nm) and 461.31189 THz (649.86935 nm), respectively. Even though we were not able to do a Doppler free measurement, since HCL was not transparent, the net effect is a broadening rather than a shift in the transition frequency, making this method suitable to find the approximate wavelength of transitions.

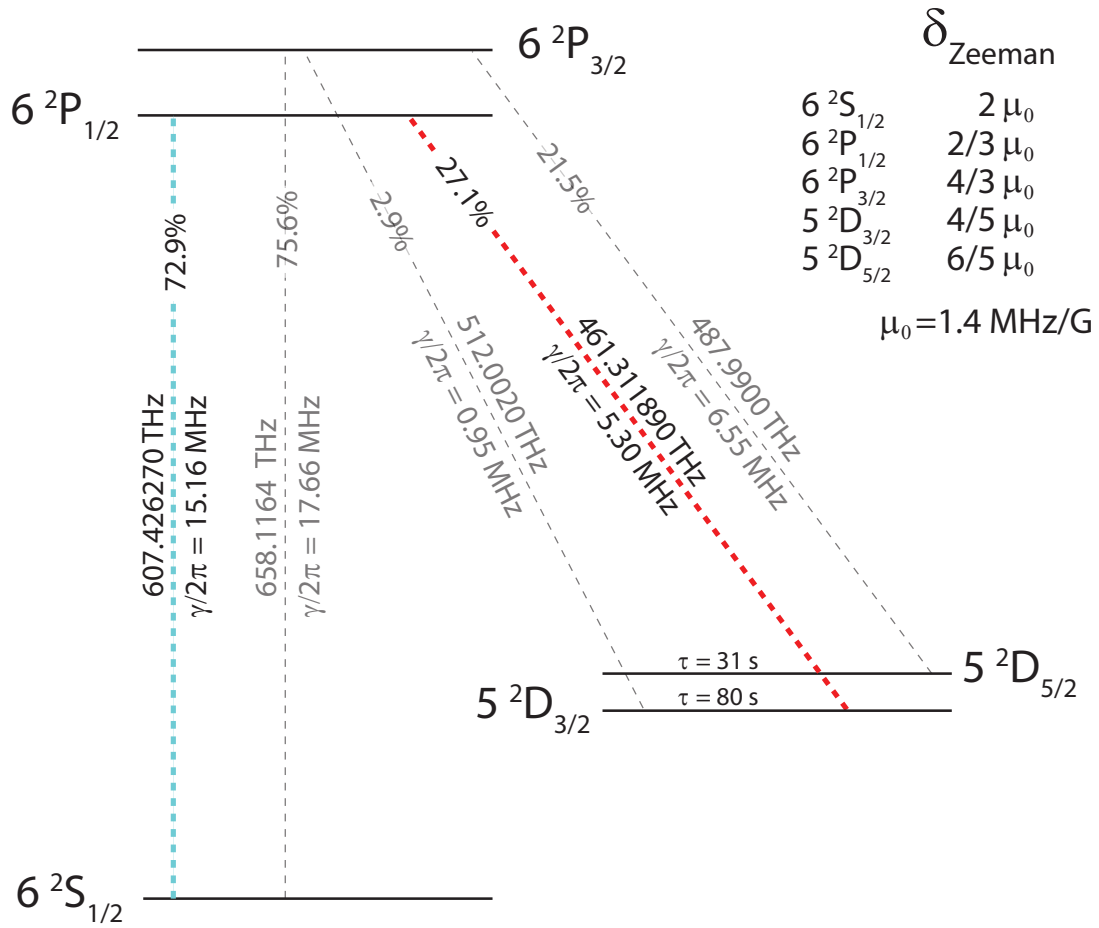


Figure 2.4: Relevant levels of the  $^{138}\text{Ba}^+$  drawn to scale. Branching ratios are given as percentages and quoted from Ref. [54, 55]. Transition frequencies (in THz) given for  $^2S_{1/2} \rightarrow ^2P_{1/2}$  and  $^2D_{3/2} \rightarrow ^2P_{1/2}$  are from readings on a calibrated HighFinesse WSU10 wavemeter in our lab and agrees with Ref. [48] which is quoted for the rest of the transitions and the natural linewidths. Low lying  $D$  state lifetimes are quoted from Ref. [56, 57]. Frequency splitting per Gauss between Zeeman sub-levels with  $\Delta m_J = 1$  (omitted in this figure) are given at upper right corner for each manifold.

two near resonant laser light fields, it is necessary to include all eight Zeeman sub-levels in the participating levels. However, for simplicity, I start with a three level system (see Fig. 2.5) and extend this formalism to include eight levels afterwards. These interactions for the specific case of  $^{138}\text{Ba}^+$  has been investigated with greater detail in Ref. [51, 58] and calculations carried out here follow these works.

### 2.2.4.1 Three level system

The total Hamiltonian of the system includes the atom, the light fields and the interaction between them:

$$H = H_{\text{atom}} + H_{\text{light}} + H_{\text{int}} \quad (2.1)$$

and the atomic Hamiltonian is described by:

$$H_{\text{atom}} = \sum_{n=1}^3 \hbar\omega_n |n\rangle\langle n| \quad (2.2)$$

where  $|n\rangle$  are the atomic eigenvectors as shown in Fig. 2.5 ( $n = 1, 2, 3$ ) with the Bohr frequencies of  $\omega_n$ . Then, the matrix representation of this atomic Hamiltonian is:

$$H_{\text{atom}} = \hbar \begin{pmatrix} \omega_1 - \omega_2 & 0 & 0 \\ 0 & 0 & 0 \\ 0 & 0 & \omega_3 - \omega_2 \end{pmatrix} \quad (2.3)$$

where the basis is defined by:

$$|1\rangle = \begin{pmatrix} 1 \\ 0 \\ 0 \end{pmatrix}, \quad |2\rangle = \begin{pmatrix} 0 \\ 1 \\ 0 \end{pmatrix}, \quad |3\rangle = \begin{pmatrix} 0 \\ 0 \\ 1 \end{pmatrix} \quad (2.4)$$

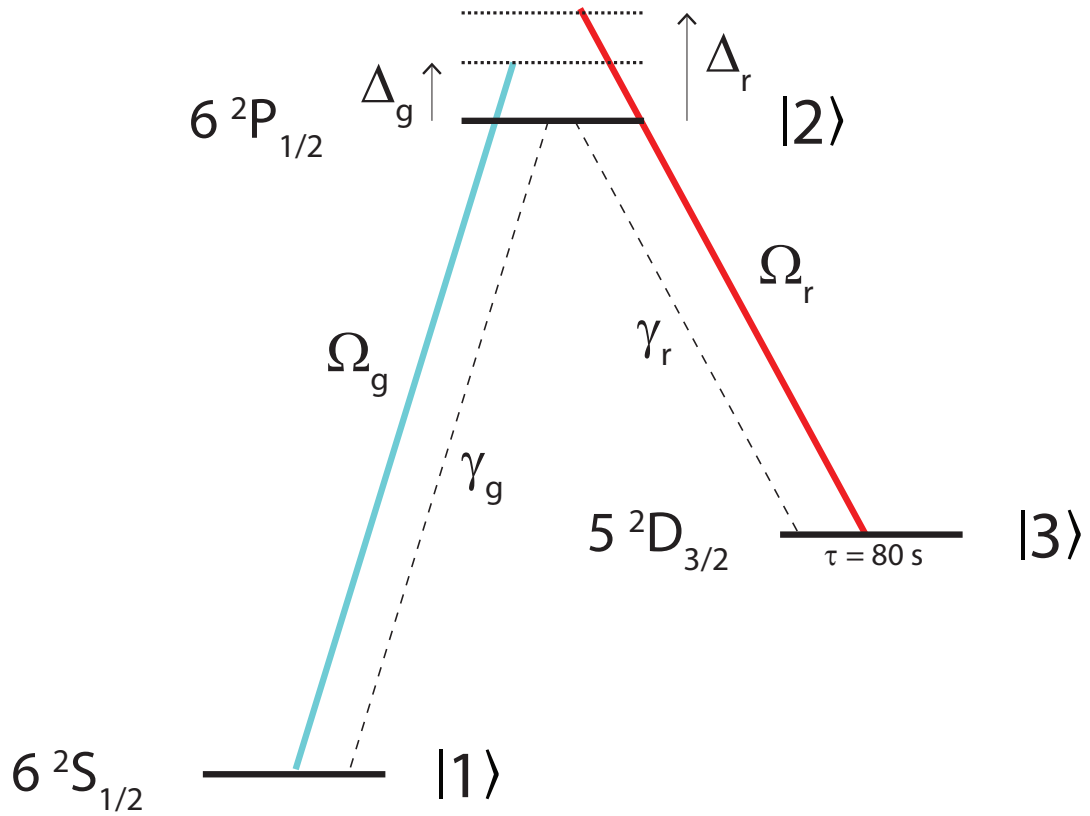


Figure 2.5: The parameters used in Bloch equations are shown here and describe a simplified three level  $^{138}\text{Ba}^+$  ion interacting with two laser fields.  $\Omega$ ,  $\gamma$  and  $\Delta$  indicate the Rabi frequencies, natural linewidths and detunings of the laser fields, respectively.

and zero energy level is chosen to be  $\hbar\omega_2$ .

The atomic levels are coupled with the laser fields; 493 nm light (green) drives the dipole transition between the states  $|1\rangle$  and  $|2\rangle$  while 650 nm light (red) couples states  $|2\rangle$  and  $|3\rangle$ . This interaction between the light field and the atom is described by:

$$H_{\text{int}} = -\vec{D} \cdot \vec{E} \quad (2.5)$$

where  $\vec{D}$  is the atomic dipole operator. Through this interaction, the light field is only negligibly effected by losing a single photon, hence the electric field operator  $\vec{E}$  can be treated classically with amplitude  $E_0$ , polarization vector  $\vec{\epsilon}$  and angular frequency  $\omega$ . Therefore, in the basis defined earlier, this interaction Hamiltonian corresponds to:

$$H_{\text{int}} = \hbar \begin{pmatrix} 0 & \frac{\Omega_g}{2} e^{+i\omega_g t} & 0 \\ \frac{\Omega_g}{2} e^{-i\omega_g t} & 0 & \frac{\Omega_r}{2} e^{-i\omega_r t} \\ 0 & \frac{\Omega_r}{2} e^{+i\omega_r t} & 0 \end{pmatrix} \quad (2.6)$$

where the Rabi frequency is defined as:

$$\begin{aligned} \hbar\Omega_g &\equiv \vec{\epsilon}_g \cdot \vec{D}_{12} E_{0g} \\ \hbar\Omega_r &\equiv \vec{\epsilon}_r \cdot \vec{D}_{23} E_{0r} \end{aligned} \quad (2.7)$$

Consequently, the complete Hamiltonian is:

$$H = \hbar \begin{pmatrix} \omega_1 - \omega_2 & \frac{\Omega_g}{2} e^{+i\omega_g t} & 0 \\ \frac{\Omega_g}{2} e^{-i\omega_g t} & 0 & \frac{\Omega_r}{2} e^{-i\omega_r t} \\ 0 & \frac{\Omega_r}{2} e^{+i\omega_r t} & \omega_3 - \omega_2 \end{pmatrix} \quad (2.8)$$

with  $H_{\text{light}}$  being eliminated by the classical approximation.

In order to include damping terms such as spontaneous emission from state  $|2\rangle$  and the finite linewidth of the lasers, a density operator  $\hat{\rho}$  is introduced to describe the system:

$$\hat{\rho} = \sum_{n,m=1,2,3} \rho_{nm} |n\rangle \langle m|. \quad (2.9)$$

Here, the diagonal elements  $\rho_{nn}$  are the probability of the atom being in the  $|n\rangle$  state, and the off-diagonals are called coherences. The Liouville equation reveals the time dynamics of the density matrix elements:

$$\frac{d\rho}{dt} = -\frac{i}{\hbar} [H, \rho] + L(\rho) \quad (2.10)$$

where  $L(\rho)$  is:

$$L(\rho) = -\frac{1}{2} \sum_k (\hat{C}_k^\dagger \hat{C}_k \rho + \rho \hat{C}_k^\dagger \hat{C}_k - 2\hat{C}_k \rho \hat{C}_k^\dagger). \quad (2.11)$$

Decay to states  $|1\rangle$  and  $|3\rangle$  from state  $|2\rangle$  via spontaneous emission are included by:

$$\hat{C}_1 = \sqrt{\gamma_g} |1\rangle \langle 2| \text{ and } \hat{C}_2 = \sqrt{\gamma_r} |3\rangle \langle 2|, \text{ respectively.} \quad (2.12)$$

And similarly, the linewidths of green ( $\gamma_{gl}$ ) and red ( $\gamma_{rl}$ ) lasers are accounted by:

$$\hat{C}_{gl} = \sqrt{2\gamma_{gl}} |1\rangle \langle 1|, \hat{C}_{rl} = \sqrt{2\gamma_{rl}} |3\rangle \langle 3|. \quad (2.13)$$

Transforming into a frame rotating at the laser frequencies, using the unitary operator:

$$U = \begin{pmatrix} e^{-i\omega_g t} & 0 & 0 \\ 0 & 1 & 0 \\ 0 & 0 & e^{-i\omega_r t} \end{pmatrix} \quad (2.14)$$

gives the Hamiltonian of the system:

$$H' = \begin{pmatrix} \Delta_g & \frac{\Omega_g}{2} & 0 \\ \frac{\Omega_g}{2} & 0 & \frac{\Omega_r}{2} \\ 0 & \frac{\Omega_r}{2} & \Delta_r \end{pmatrix} \quad (2.15)$$

where detunings are defined as:

$$\begin{aligned} \Delta_g &= \omega_g - (\omega_2 - \omega_2) \\ \Delta_r &= \omega_r - (\omega_2 - \omega_3) \end{aligned} \quad (2.16)$$

and the density operator is:

$$\rho' = \hat{U} \rho \hat{U}^\dagger . \quad (2.17)$$

Under this transformation the damping terms do not change.

The optical Bloch equations are acquired by inserting  $H'$ ,  $\rho'$  and  $L(\rho)$  into Eqn. 2.10 :

$$\begin{aligned} \vec{\rho} &\equiv (\rho_{11}, \rho_{12}, \dots, \rho_{33}) \\ \dot{\vec{\rho}}_m &= \sum_n M_{mn} \vec{\rho}_n \end{aligned} \quad (2.18)$$

with the solution of:

$$\vec{\rho}(t) = e^{Mt} \vec{\rho}(0) \quad (2.19)$$

for initial condition given by  $\vec{\rho}(0)$ .

Finally, the steady state solution, along with the  $\sum_n \rho_{nn} = 1$  normalization constraint, can be used to find the excitation spectrum:

$$\dot{\vec{\rho}} = 0 = \sum_n M_{mn} \vec{\rho}_n . \quad (2.20)$$

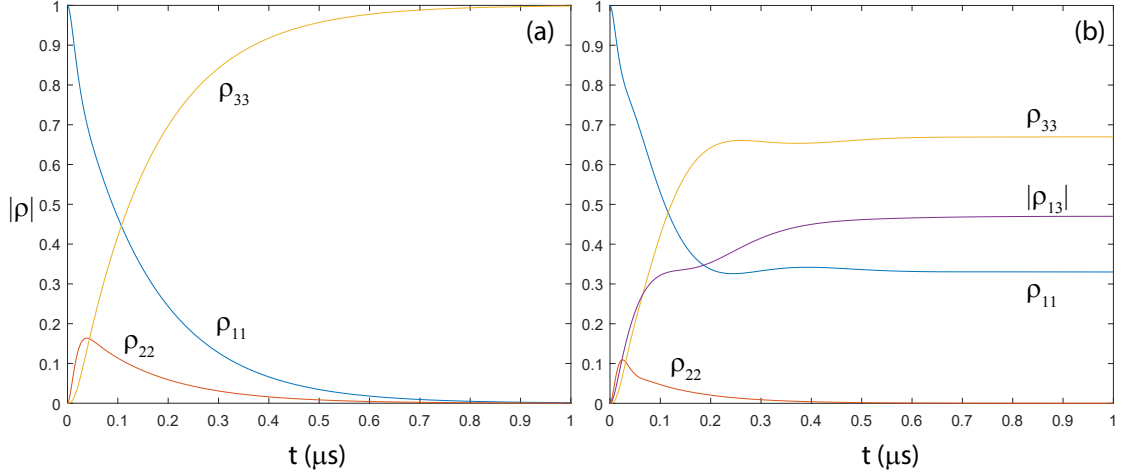


Figure 2.6: (a) The three level atom is optically pumped to state  $|3\rangle$  when only a resonant green laser is incident without a re-pumping red laser. The parameters used are  $s_g = 1$ ,  $s_r = 0$ ,  $\Delta_g = 0$ ,  $\Delta_r = 0$ ,  $\gamma_{gl} = 0$ ,  $\gamma_{rl} = 0$  (b) Two laser fields drive the atom into a dark state, a coherent superposition of states  $|1\rangle$  and  $|3\rangle$ , when green and red lasers have the same detuning. Time evolution is shown for  $s_g = 1$ ,  $s_r = 4$ ,  $\Delta_g/2\pi = -10$  MHz,  $\Delta_r/2\pi = -10$  MHz,  $\gamma_{gl} = 0$ ,  $\gamma_{rl} = 0$ .

In the following examples, the Rabi frequencies of transitions with green ( $i \rightarrow g$ ) and red ( $i \rightarrow r$ ) laser interactions are expressed with corresponding saturation parameters:

$$\Omega_i = \sqrt{\frac{s_i}{2}} \gamma_i \quad (2.21)$$

and the decay rates are that of a  $^{138}\text{Ba}^+$  atom,  $\gamma_g/2\pi = 15.1$  MHz,  $\gamma_r/2\pi = 5.3$  MHz. Time dynamics of this three level atom when subject to laser fields is shown in Fig. 2.6.

Since in photon counting experiments the typical integration time (0.1-1 s) is much longer than time scale of settling to the steady state ( $< 1 \mu\text{s}$ ), time dynamics can be ignored and the excitation spectrum is evaluated at steady state. For

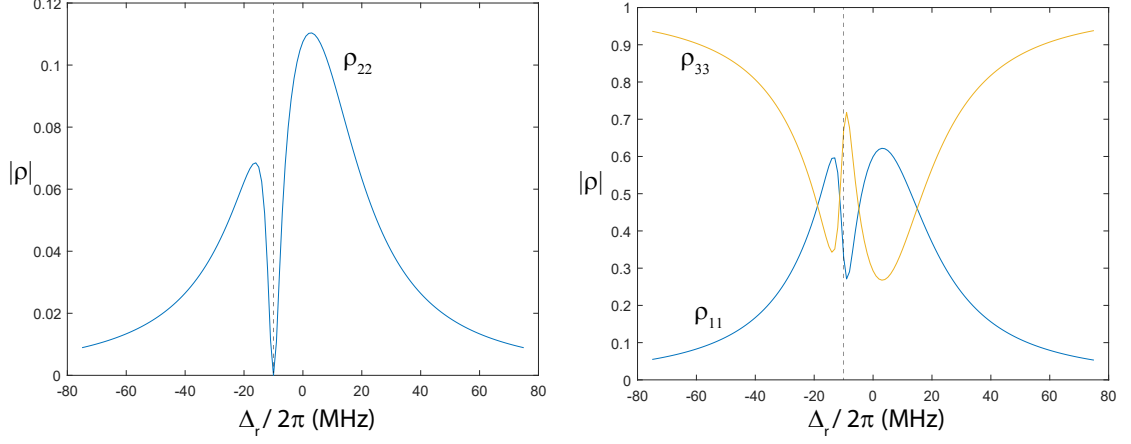


Figure 2.7: Density matrix diagonal elements of three level system at steady state with parameters  $s_g = 1$ ,  $s_r = 4$ ,  $\Delta_g/2\pi = -10$  MHz,  $\gamma_{gl} = 0$ ,  $\gamma_{rl} = 0$  and the red laser detuning  $\Delta_r/2\pi$  is scanned. Dashed line shows the coherent dark state (see Fig. 2.6 (b)) where  $\rho_{22}$  vanishes and the atom does not emit photons when  $\Delta_g = \Delta_r$ . Fluorescence measurement on an atom reveals  $\rho_{22}$ . Compared to a two level system where  $\rho_{22} = 0.5$  for a saturated transition, introduction of an extra level results in significant reduction in excited state population and consequently measured brightness of the atom.

example, emitted green photons are:

$$\# \text{ Green Photons} = \gamma_g \rho_{22}(t_{ss}). \quad (2.22)$$

The excitation spectrum is shown in Fig. 2.7.

#### 2.2.4.2 Eight level system

With Zeeman sublevels included,  $^{138}\text{Ba}^+$  forms an eight level system where each manifold contributes  $2J + 1$  states that are lifted from zero field degeneracy by the magnetic field,  $\Delta\omega/2\pi \approx \frac{1}{2}g_J\mu_0B$  where  $g_J$  is the Landé g-factor (see Fig. 2.4).

Optical Bloch equations can be derived following the same procedure described in the previous section, and the addition of a magnetic field introduces laser polar-

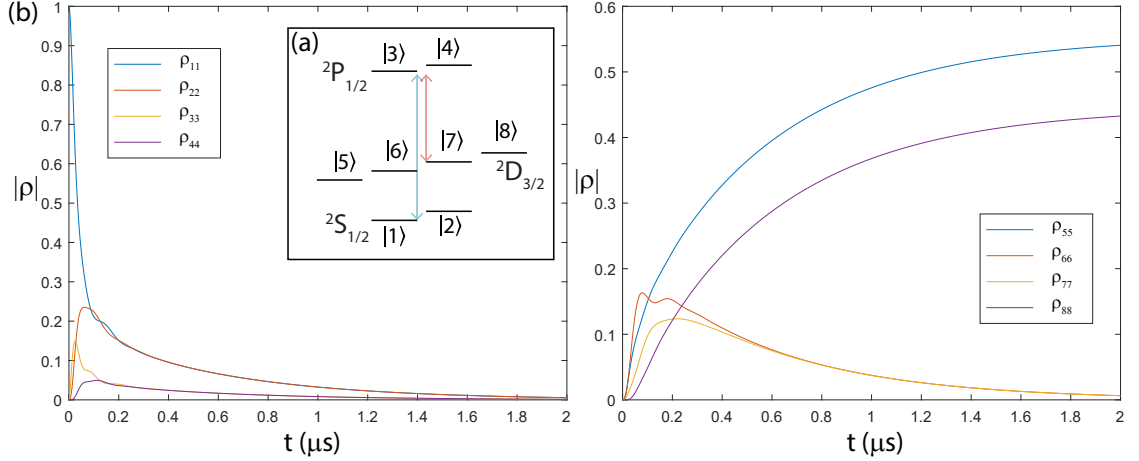


Figure 2.8: (a) Indexing of the  $^{138}\text{Ba}^+$  states. (b) The eight level  $^{138}\text{Ba}^+$  atom is optically pumped to the states  $|5\rangle$  and  $|8\rangle$  when only a  $\pi$  polarized laser field is incident as there are no levels from these states that  $\pi$  light can couple to. The parameters used are  $s_g = 1$ ,  $s_r = 2$ ,  $\Delta_g/2\pi = -10$  MHz,  $\Delta_r/2\pi = 10$  MHz,  $\gamma_{gl} = 0$ ,  $\gamma_{rl} = 0$  and  $B = 4$  Gauss. Starting condition of  $|\psi(t=0)\rangle = |1\rangle$  results in higher occupation in  $|5\rangle$  compared to  $|8\rangle$  in the steady state.

ization effects and the field amplitude into the dynamics.

Fig. 2.8 and 2.9 show simulated time dynamics and the steady state excitation spectrum of the  $^{138}\text{Ba}^+$  ion.

### 2.3 Double Imaging Setup

The atoms are imaged by collecting the spontaneously emitted photons on  $^2P_{1/2} \rightarrow ^2S_{1/2}$  decays to a camera. Since the wavelengths of these photons are vastly different for  $^{171}\text{Yb}^+$  and  $^{138}\text{Ba}^+$ , a double imaging setup (see Fig. 2.10) is constructed to have the same focus for both point sources at the detector surface.

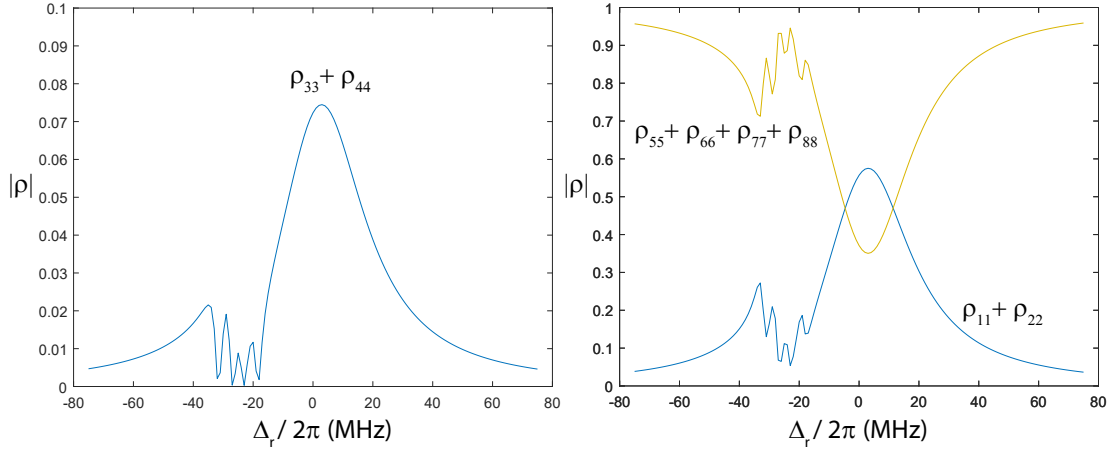


Figure 2.9: For simplicity in presentation populations in each manifold are summed up. Extra Zeeman levels result in multiple dark resonances compared to the single coherent dark state of the three level system. The parameters are set to  $s_g = 2$ ,  $s_r = 4$ ,  $\Delta_g/2\pi = -25$  MHz,  $\gamma_{gl} = 0$ ,  $\gamma_{rl} = 0$ ,  $B = 4$  Gauss with the laser fields polarized perpendicular to the quantization axis.

## 2.4 High Numerical Aperture Setup

In addition to a double imaging setup, a second view-port allows collecting photons from the opposite side of the vacuum chamber. The re-entrant window on this side is designed to accommodate a NA-0.6 PhotonGear lens with a working distance of about  $\sim 17$  mm. This objective collects  $\sim 10\%$  of the emitted light and will be used to couple photons to a single mode fiber for eventual entanglement of remote qubits. However, so far it is only utilized in a free space setup and mainly used for collecting 493 nm photons (see Fig. 2.11).

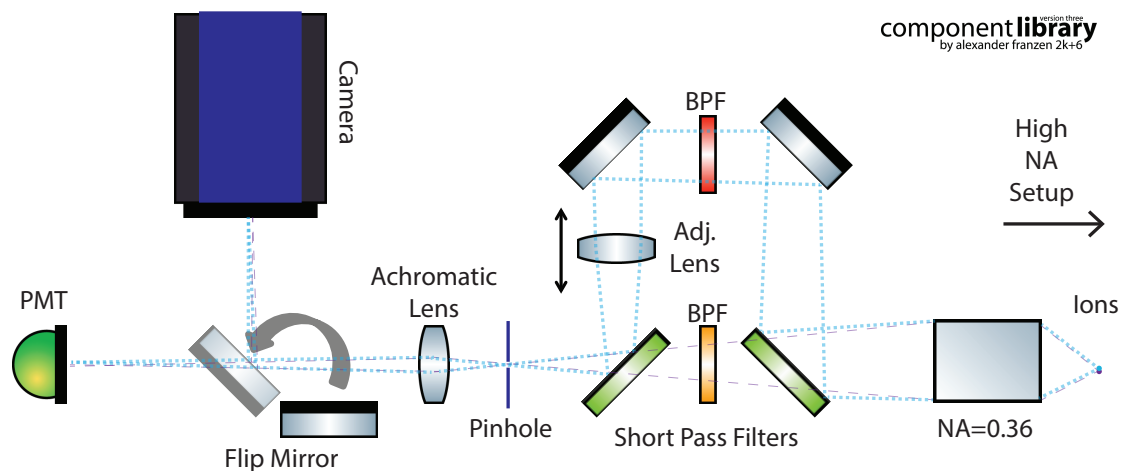


Figure 2.10: The photons from both  $^{171}\text{Yb}^+$  and  $^{138}\text{Ba}^+$  are collected with an NA=0.36 lens stack. Short pass filters are used to separate 369 nm and 493 nm light and an adjustable lens corrects for chromatic aberration. Band pass filters (BPF) are used to block the room light and other laser fields while letting through 369 and 493 nm fields and additionally a pinhole of diameter 100-200  $\mu\text{m}$  spatially filters the laser background from the ion signals. Finally an achromatic lens provides extra magnification of the image formed at pinhole. A flip mirror is used to direct light between a PMT, used in photon resolving for state detection of  $^{171}\text{Yb}^+$  and fluorescence measurements, and a camera. Since the camera is only used for loading verification and ion number confirmation, an inexpensive CMOS camera (PointGrey Blackfly 2.3 MP Mono GigE PoE) is sufficient in this setup.

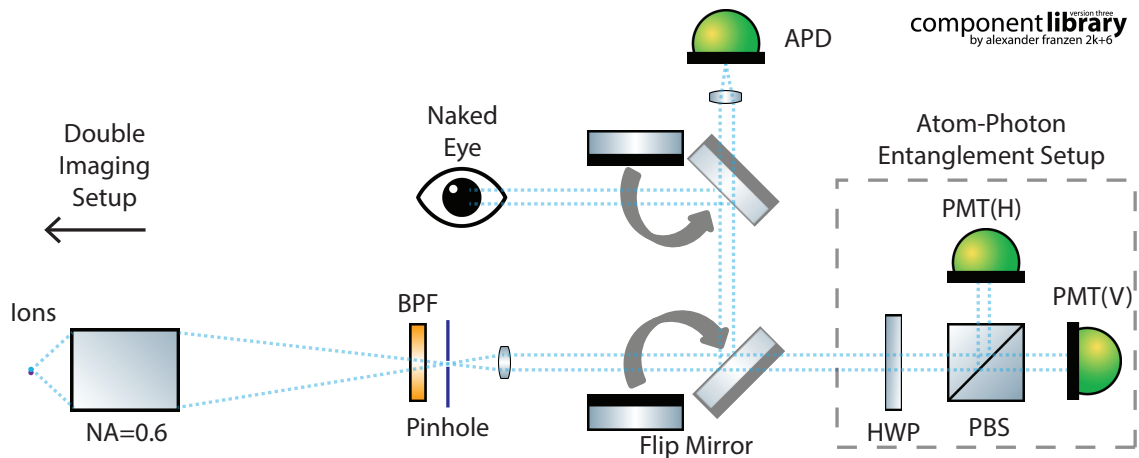


Figure 2.11: For correcting aberrations [59] and maximizing the photon collection, NA=0.6 lens is placed on a five axis pitch, yaw and translation stage. A  $50\ \mu\text{m}$  diameter pinhole spatially filters the  $^{138}\text{Ba}^+$  photons from background. Flip mirrors are used for switching between different applications; atom-photon entanglement setup incorporates polarization analyzing optics and photo multiplier tubes (PMT's) with low dark counts to minimize errors while avalanche photo diode (APD) with higher quantum efficiency at 493 nm region allows getting shorter integration times. High numerical aperture and the sensitivity of the human eye to visible photons make it possible to see a single  $^{138}\text{Ba}^+$  with naked eye, which is not possible with  $^{171}\text{Yb}^+$  and other ions with strong dipole transitions around UV wavelengths. In future applications of entanglement of remote  $^{138}\text{Ba}^+$  qubits, atom-photon entanglement setup can be replaced with a single mode fiber coupling optics.

## 2.5 Re-ordering of the Ions

In a multi-species system, different atoms might be required to occupy specific positions. For example, communication qubits need to be coupled into a single mode fiber for generating entanglement between them, and a change in the position will considerably reduce the coupling efficiency with optics aligned to a certain spot. Additionally, laser beams addressing a particular species at a certain position likely do not have the same intensity at different locations which will change the interaction dynamics.

The experiments presented in this thesis are carried out with only one of each species co-trapped in the same chain, and the ions are observed to swap positions on minute timescales possibly caused by the background gas collisions. Two different hardware implementations are used to keep the ions in a desired configuration.

The first approach relies on changing the applied DC voltages to push the ions to a spot where the micromotion [38] is not compensated. These voltages are applied for  $\sim 200$  ms and then brought back to the original micromotion compensated values. This results in brief heating of the ions by the Doppler cooling beams to melt the crystal, and re-crystallizing in a random configuration when the optimal cooling conditions are satisfied again by applying the initial voltages.

Another method is realized by RF voltage modulation. At low RF powers, the ions align along the transverse axis due to weaker confinement, and they get re-ordered in the longitudinal direction when switched back to high RF. This is realized by amplitude modulation of the RF voltage with control DC voltages.

Both methods probabilistically re-order the  $^{171}\text{Yb}^+ - ^{138}\text{Ba}^+$  crystal in the correct configuration and for only two ions these approaches have been satisfactory since it takes only a few trials on average to get the right formation. However, with inclusion of more memory and communication qubits to the modules, a deterministic re-ordering method might be necessary such as has been realized in Paul traps with sophisticated electrode structures [60].

## Chapter 3: Ytterbium and Barium Atomic Ion Qubits

### 3.1 Overview

In our multi-species apparatus, we encode the memory qubits in the  $^2S_{1/2}$  manifold hyperfine clock states of  $^{171}\text{Yb}^+$  atomic ions,  $|F = 0, m_F = 0\rangle \equiv |\downarrow\rangle$  and  $|F = 1, m_F = 0\rangle \equiv |\uparrow\rangle$ . They are well suited to be used as memory qubits with their long coherence times and easy state initialization/detection schemes [5]. The qubit frequency separation of  $12\,642\,812\,118.5 + \Delta$  Hz can be conveniently addressed with microwave sources and pulsed lasers [45] for quantum operations, and a small second order dependence to external magnetic field ( $\Delta = 310.8 B^2$  Hz with field amplitude  $B$  in G) is the source of long coherence time.

As communication qubits, we use the electron spin of  $^{138}\text{Ba}^+$  atomic ions in the  $^2S_{1/2}$  level,  $|J = 1/2, m_J = -1/2\rangle \equiv |\downarrow\rangle$  and  $|J = 1/2, m_J = +1/2\rangle \equiv |\uparrow\rangle$  [61]. The frequency splitting between qubit states depend on the external magnetic field and it is given by  $2\mu_0 B \approx 2.8 B$  MHz where  $\mu_0$  is the Bohr magneton (1.4 MHz/G) and  $B$  is magnetic field in G. Current optical fiber and photon detector technologies make  $^{138}\text{Ba}^+$  an attractive communication qubit compared to other common trapped atomic ion species owing to its visible 493 and 650 nm photon emission lines.

For the eventual construction of a multi-species network, there are several

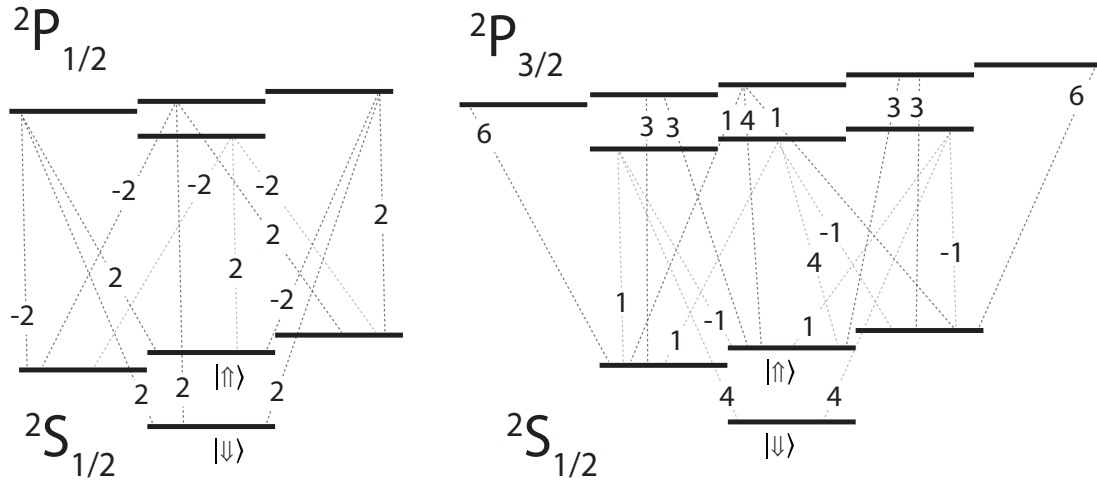


Figure 3.1: For ease of representation, Clebsch-Gordan coefficients are shown as  $6 \times C^2$  in here. The transitions with a negative sign indicate a minus sign on the corresponding coefficient.

essential single qubit quantum operations that must be performed in the modules, such as qubit initialization, state detection, coherent rotations and atom-photon entanglement. In this chapter, I present the experimental techniques used for these operations.

### 3.2 Ytterbium Hyperfine Qubit

The excited states of the atoms can be utilized for coherent and dissipative qubit operations. The relative coupling strength of dipole allowed transitions and decay probabilities from an excited level to different ground states are characterized with Clebsch-Gordan coefficients, which are shown on Fig. 3.1 for  $^{171}\text{Yb}^+$  atoms. Fig. 3.2 summarizes the Doppler cooling, state detection and initialization procedures for the  $^{171}\text{Yb}^+$  atom.

Doppler cooling is realized by driving the  $F = 1 \leftrightarrow F = 0$  transition between

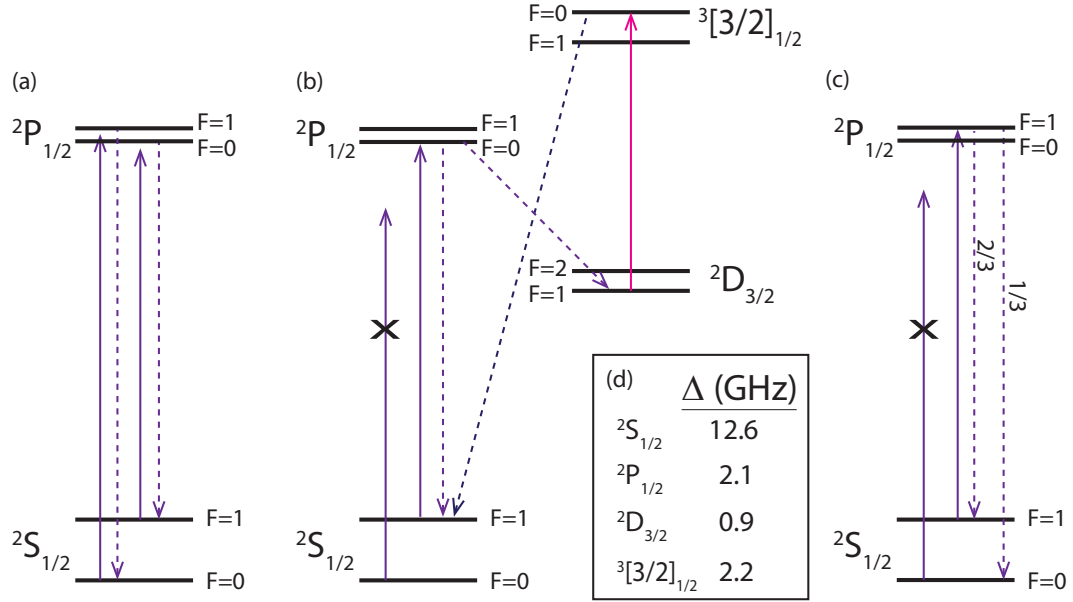


Figure 3.2: (a) Doppler cooling beam is detuned from the transition to achieve an optimal temperature. Only a small amount of optical intensity on the sideband is sufficient as the off-resonant pumping probability is low. (b) State detection of the qubit relies on selective photon scattering from  $F = 1$  levels. Branching needs to be considered here, as any mixing between  $F = 0$  and  $F = 1$  population would result in reduced fidelity. This is prevented by forbidden decays from the  $F = 0$  level of  $^3[3/2]_{1/2}$  to  $F = 0$  of  $^2S_{1/2}$ . (c) The optical pumping beam is produced by adding 2.1 GHz sidebands to the detection beam with an EOM. After each photon scattering event, the atom decays to the  $F = 0$  level with a probability of  $1/3$ . Even though it is not a limiting factor in most applications, the carrier needs to be eliminated for faster optical pumping as scattering with this component would result in photon scattering without decays to  $F = 0$ . This can be realized with using an AOM rather than EOM to add the necessary 2.1 GHz. (d) Table of hyperfine splittings in different manifolds.

$^2S_{1/2}$  and  $^2P_{1/2}$  levels with a detuning  $\delta \approx -\gamma/2$  where  $\gamma/2\pi \approx 19.6$  MHz [26]. Off-resonant coupling to the  $F = 1$  level result in pumping to the  $F = 0$  level of the  $^2S_{1/2}$  manifold. Hence, a second beam is necessary to put the population back to main cooling cycle and it is produced by introducing a 12.6+2.1 GHz sideband with an EOM.

A resonant beam is turned on for the state detection, and population in  $F = 1$  scatters many photons while  $F = 0$  scattering rate is greatly reduced since the laser is detuned by 14.7 GHz from the closest allowed transition. By looking at the number of collected photons in a certain time window, a single shot measurement is done on the  $^{171}\text{Yb}^+$  qubit state. The background light from the environment and the scattered laser light from the trap electrodes that might find a way to the photon detectors are minimized by spectral and spatial filters to prevent these photons from being registered as atom signal. The main limitation with this method is off-resonant pumping to the  $F = 0$  level [5,62] which abruptly stops the fluorescence of the qubit state  $|\uparrow\rangle$ . In our setup, with a 0.36 NA lens and 30 % efficient photon detectors, we can detect the qubit state with a fidelity of  $\mathcal{F} \approx 99.2$  % in around 200  $\mu\text{s}$ . With the employment of faster optics (NA=0.6), a record  $^{171}\text{Yb}^+$  state detection fidelity of 99.9% is demonstrated in Kim group at Duke University [44].

The state of the  $^{171}\text{Yb}^+$  qubit can be initialized to  $|\downarrow\rangle$  by turning on a laser resonant with  $F = 1$  of  $^2S_{1/2}$  and  $^2P_{1/2}$ . After each scattering event, the atom decays to  $F = 0$  with 1/3 probability. The low probability of pumping back from  $F = 0$  with this laser beam results in near perfect state initialization with a timescale of less than 1 $\mu\text{s}$ .

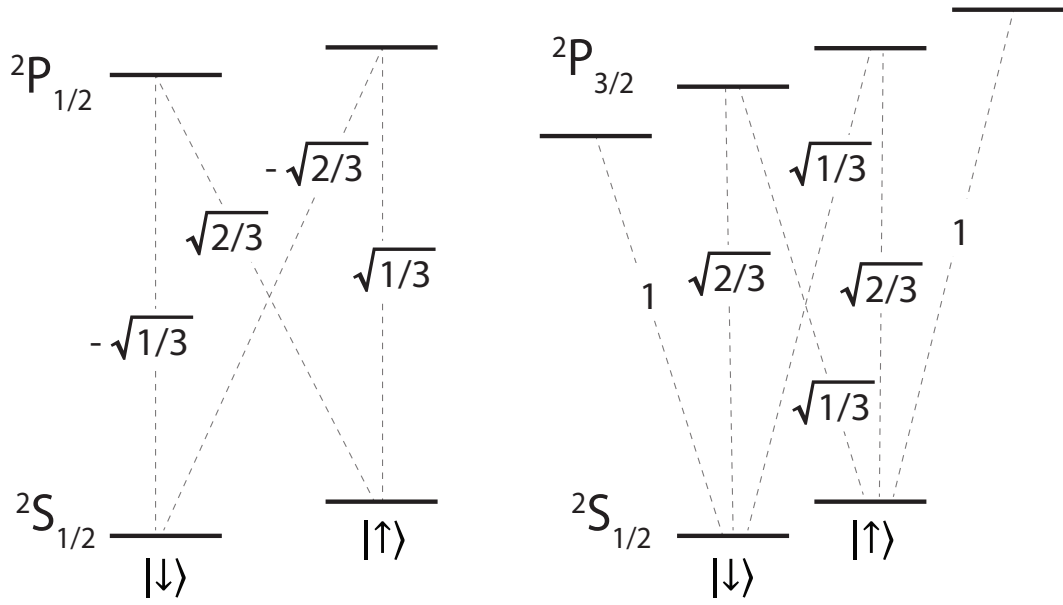


Figure 3.3: Clebsch-Gordan coefficients of allowed dipole transitions on  $^{138}\text{Ba}^+$  atom. Even though  $^2P_{3/2}$  states are not directly populated in the experiments conducted here, they play an important role on the stimulated Raman transition that will be analyzed later in this chapter.

### 3.3 Barium Zeeman Qubit

The Clebsch-Gordan coefficients for  $^{138}\text{Ba}^+$  atom are given in Fig. 3.3. While decays to levels  $^2D_{3/2}$  and  $^2D_{5/2}$  change the time dynamics of the operations, the individual matrix elements related to the coupling between  $^2P_{1/2} \leftrightarrow ^2D_{3/2}$  and  $^2P_{3/2} \leftrightarrow ^2D_{5/2}$  level do not play an important role on most of the operations described here for  $^{138}\text{Ba}^+$ , therefore they are not shown.

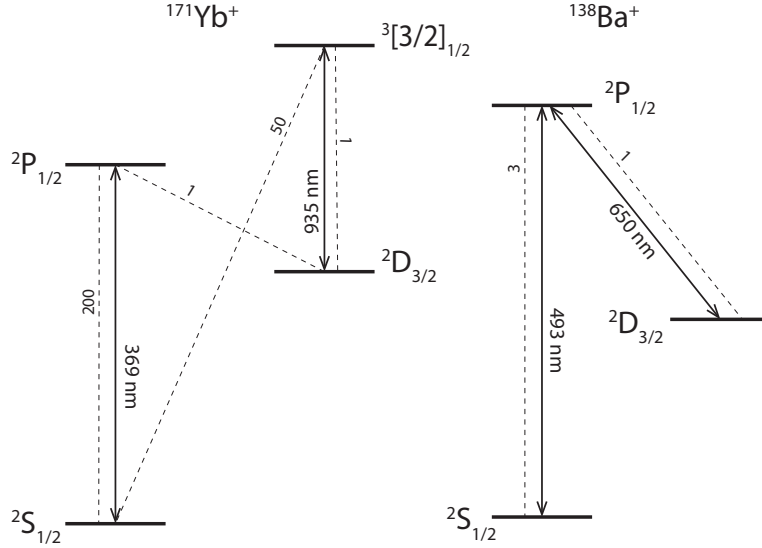


Figure 3.4: The numbers on dashed lines indicate approximate relative branching ratios; the small decay probability to the  $^2D_{3/2}$  level (1/200), and bow-tie configuration of the  $^{171}\text{Yb}^+$  excitation scheme result in a simplified Doppler cooling mechanism where it is sufficient to consider  $^2S_{1/2}$  and  $^2P_{1/2}$  manifolds. In contrast, a much higher branching ratio (3:1) and dark states that might be introduced in a system of  $^{138}\text{Ba}^+$  necessitates all three levels and two laser fields to be considered in the cooling layout.

### 3.3.1 Doppler Cooling

The  $^{171}\text{Yb}^+$  atom can be treated as a two level closed system in Doppler cooling applications, as the small branching ratio introduces a negligible divergence from the assumed two level structure and additionally, re-pumping from the metastable  $^2D_{3/2}$  level can be achieved without a transition back to the  $^2P_{1/2}$  level (see Fig. 3.4(a)). In contrast, since the levels  $^2S_{1/2}$ ,  $^2P_{1/2}$  and  $^2D_{3/2}$  form a  $\Lambda$  configuration in  $^{138}\text{Ba}^+$  as shown in Fig. 3.4(b), these manifolds and two laser fields that couple them need to be considered in the Doppler cooling process of this atom.

Interestingly, a numerical analysis shows that the Doppler cooling process in this configuration is mainly dominated by the  $^2S_{1/2}$  to  $^2P_{1/2}$  transition and the fre-

quency of the  ${}^2D_{3/2}$  to  ${}^2P_{1/2}$  laser has almost no effect [63]. Still, for optimal cooling, the 650 nm laser should have enough optical intensity to saturate the transition to prevent population trapping in the  ${}^2D_{3/2}$  levels, and the frequency of this laser needs to be adjusted to prevent driving the atom to a coherent dark state in conjunction with the 493 nm laser [64].

Additionally, in a non-zero magnetic field, the transitions between  ${}^2S_{1/2}$  and  ${}^2P_{1/2}$  Zeeman sublevels have different frequencies, hence adjustment in the detuning of the 493 nm laser is necessary for efficient cooling. This shift from the nominal optimal detuning of  $\delta = -\gamma/2$  approximately amounts to  $-\frac{4}{3}\mu_0 B$  ( $-\frac{2}{3}\mu_0 B$ ) for light polarized perpendicular (parallel) to the quantization axis where the magnetic field  $B$  is in units of G and  $\mu_0 = 1.4$  MHz/G [63]. Finally, optical pumping to a particular Zeeman sublevel must be avoided by adjusting the polarization of both lasers. For instance, a pure  $\pi$  polarized 650 nm light would lead to population trapping at  ${}^2D_{3/2}$ ,  $m_J = \pm 3/2$  levels, which can be prevented by introducing circular polarized components. Even with these adjustments, there are inevitable dark states introduced with the  ${}^2D_{3/2} \leftrightarrow {}^2P_{1/2}$  transition [65] which the atom evolves out of at the Larmor frequency. This results in an overall drop in fluorescence rate and Doppler cooling speed.

### 3.3.2 State Initialization

We initialize the  ${}^{138}\text{Ba}^+$  qubit with polarization selectivity of the dipole transitions between the states  $|\downarrow\rangle$ ,  $|\uparrow\rangle$  and the levels at the excited  ${}^2P_{1/2}$  manifold (see

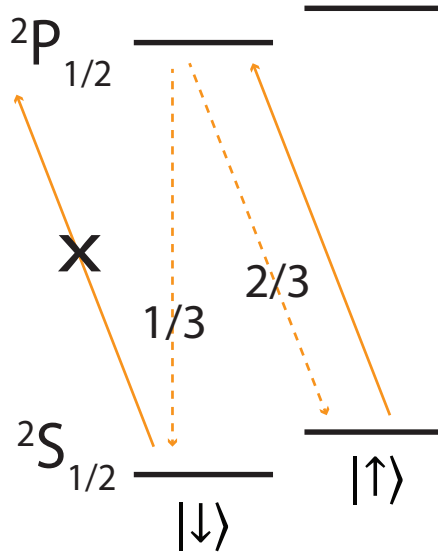


Figure 3.5: Levels involved in optical pumping of the  $^{138}\text{Ba}^+$  qubit, and decay probabilities to different qubit states. After scattering  $N$  photons, the probability of the qubit being initialized to the  $|\downarrow\rangle$  state is:  $P(|\downarrow\rangle) = 1 - (2/3)^N$ . Decays from  $^2P_{1/2}$  to  $^2D_{3/2}$  manifold is not included for simplicity, as these events effect overall speed and not the efficiency.

Fig. 3.5). When a 493 nm  $\sigma^-$  polarized laser light field is incident on the atom, the state  $|\uparrow\rangle$  gets excited to the  $^2P_{1/2} |m_J = -1/2\rangle$  level and decays to the  $|\downarrow\rangle$  state with  $1/3$  probability. Since the  $|\downarrow\rangle$  state does not have any allowed dipole transitions with this  $\sigma^-$  light which might put the population back into the state  $|\uparrow\rangle$ , the atom gets optically pumped to the  $|\downarrow\rangle$  state after several scattering events. The qubit can be initialized to the  $|\uparrow\rangle$  state as well following same procedure with a  $\sigma^+$  light.

Since the efficiency of this operation depends on the polarization purity of the light, a polarization maintaining fiber is used to send in this light to prevent long term drifts and eliminate occasional calibration requirements. Even though a single quarter waveplate (QWP) is enough to turn the linear polarization output of the fiber into the circular light necessary for the optical pumping, we use a set of

three waveplates, quarter-half-quarter, to have arbitrary control on the polarization state in order to account for polarization rotations that might be introduced during reflections on mirrors and birefringence of the view-ports.

To achieve the maximum optical pumping efficiency, the fluorescence counts from the atom are monitored while the laser beam is incident, and waveplates are adjusted to minimize these counts. Since realizing the perfect polarization also depends on alignment between the quantization axis and the beam wave vector  $\vec{k}$ , fine adjustment on the perpendicular magnetic field components is generally necessary to tilt the field along the  $\vec{k}$ . We obtain a typical optical pumping time of less than 1  $\mu\text{s}$  with  $> 99.5\%$  efficiency, which is ultimately limited by the polarization optics.

### 3.3.3 State Detection without Shelving

In this network architecture, entanglement generated between  $^{138}\text{Ba}^+$  qubits in different modules is immediately transferred to neighboring  $^{171}\text{Yb}^+$  qubits. Consequently,  $^{138}\text{Ba}^+$  qubits only act as a link between memory qubits in the system and quantum information processing ultimately does not rely on state detection of these communication qubits. However, qubit state detection for  $^{138}\text{Ba}^+$  atoms is still useful for troubleshooting of operations until the state can be reliably transferred to and read out on memory qubits. Since  $^{138}\text{Ba}^+$  atoms lack an isolated cycling transition for qubit states, a common detection method on  $^{138}\text{Ba}^+$  relies on shelving one of the qubit states to a long lived state and looking at the fluorescence of the remaining population [66]. This method requires two additional lasers, one for

shelving and another for depopulating the long lived state. As this detection method is not necessary in the long run, we have implemented a different state detection technique which does not require additional lasers.

In our  $^{138}\text{Ba}^+$  state detection technique (see Fig. 3.6(a) and (b)), after conducting an experiment, we first excite the  $^2S_{1/2}$  to  $^2P_{1/2}$  transition with 493 nm  $\sigma^+$  polarized light. If the ion is in the  $|\downarrow\rangle$  state, it scatters three photons in average before getting optically pumped to the  $|\uparrow\rangle$  state. In contrast, the  $|\uparrow\rangle$  state does not scatter any photons due to absence of excited state lines this it can couple to. In the next experimental cycle, we send  $\sigma^-$  polarized light and this time only the  $|\uparrow\rangle$  state scatters photons. We cycle between  $\sigma^+$  and  $\sigma^-$ , and look at the distribution of photon detection events corresponding to the polarization of the excitation beam to infer the  $^{138}\text{Ba}^+$  qubit state.

As it is evident from the description, one of these detection beams is identical to the optical pumping beam. Hence, nominally only one extra beam addition to the setup is necessary for this detection scheme. To create this second beam, we send another orthogonally polarized beam through the same polarization maintaining fiber (see. Fig. 3.7), and rotations through the optics turn it into the opposite circular polarization state compared to the optical pumping beam.

Even though some information can be extracted from the qubit with the use of a single beam, we reduce statistical effects on state detection accuracy stemming from the probabilistic nature of this method by switching between the orthogonally polarized beams. For instance, the number of photon detection events in a certain time window (T) from  $^{138}\text{Ba}^+$  qubit ( $\alpha|\downarrow\rangle + \beta|\uparrow\rangle$ ) subject to only  $\sigma^-$  beam on each

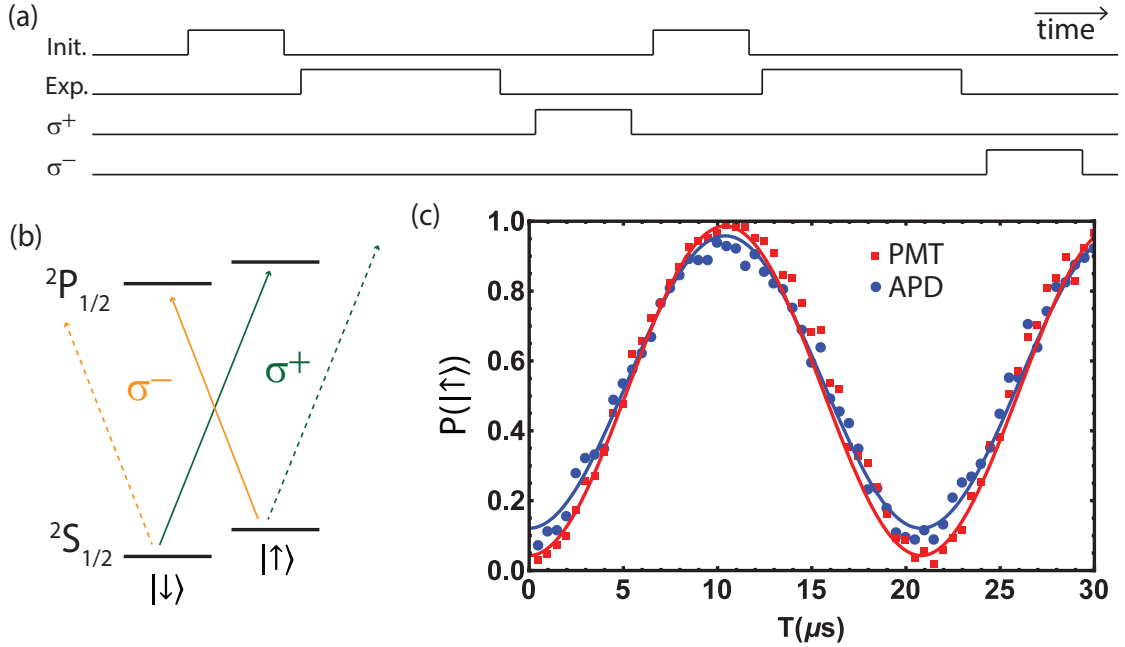


Figure 3.6: (a)  $^{138}\text{Ba}^+$  detection timing sequence. (b) Relevant energy levels on  $^{138}\text{Ba}^+$  and coupling of different levels with  $\sigma^+$  and  $\sigma^-$  light. (c) State detection on a single qubit Rabi flopping experiment. In this state detection technique, we utilize already existing infrastructure that is required for achieving rapid entanglement generation between modules; an 80% quantum efficient avalanche photodiode (APD) and a lens that collects around 10% of the emitted light ( $\text{NA}=0.6$ ). Hence, overall data acquisition rate of our technique compared to a deterministic single shot state detection method amounts to 8%. Using a photo multiplier tube (PMT) which has lower dark counts compared to the APD, we get higher detection accuracy. However, this switch also results in a lower data acquisition rate due to lower PMT quantum efficiency of 30%.

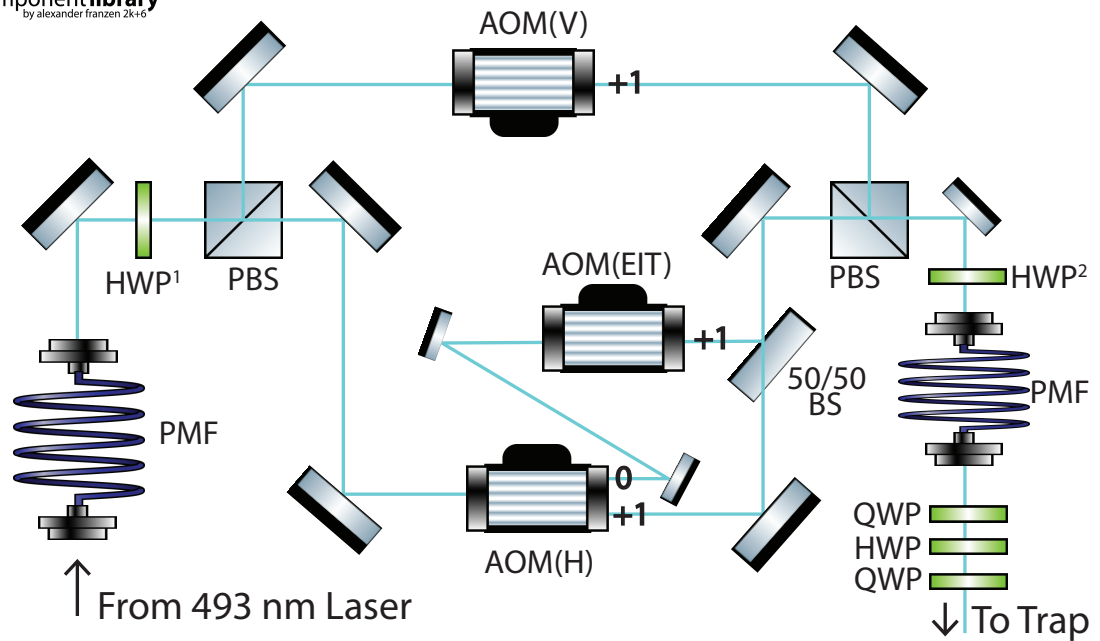


Figure 3.7: 493 nm light is sent to initialization/detection optical setup through a polarization maintaining fiber (PMF). HWP<sup>1</sup> is used for optical power adjustments between two arms, while HWP<sup>2</sup> is necessary for aligning the polarization to the axis of second PMF. AOM(H) and AOM(V) are used to switch between orthogonally polarized detection beams; they couple into the same fiber and waveplate stack turns  $H \rightarrow \sigma^+$  and  $V \rightarrow \sigma^-$ . For optimal addressing of the dipole transitions, the RF drive frequency difference between these two AOM's should match the corresponding transition frequency difference of  $^{138}\text{Ba}^+$ . This amounts to  $\Delta(RF)/2\pi = \frac{8}{3} \times 1.4 \times B$  MHz where magnetic field amplitude  $B$  is in G. An extra beam is also incorporated in this setup for electromagnetically induced transparency (EIT), whose function will be explained in the following chapter. Numbers on the beams following AOM's indicate which diffraction order is being used.

trial would yield a Poisson distribution around the mean:

$$\lambda \propto \beta \frac{\Gamma(I, \delta)}{\Gamma_{\text{Max}}} P_{\text{eff}} N(T) \quad (3.1)$$

where  $N(T)$  is number of trials in this time window,  $P_{\text{eff}}$  is the overall photon detection efficiency of the system, and finally  $\Gamma(I, \delta)$  is the scattering rate as a function of the intensity,  $I$ , and detuning  $\delta$ . Consequently, different superposition states produce distributions that overlap each other, leading to inaccuracy in inferring the state of  $^{138}\text{Ba}^+$  from the number of events where a photon is detected. Introduction of the second beam results in a higher state detection accuracy by producing another Poisson distribution that can be used, similar to the  $^{171}\text{Yb}^+$  case where both qubit states have a measurable outcome. Overall, with two different circular polarized beams utilized, this scheme resembles a modified  $^{171}\text{Yb}^+$  state measurement technique where only some random subset of all the measurements are taken into account.

Additionally, the accuracy of this method is not susceptible to slow intensity and frequency noise of the laser to a certain extent; as the polarization is swapped for each trial, noise sources slower than the experimental repetition rate, typically  $< 1 - 10$  kHz, become common mode since they shift the mean value for both distributions. We obtain a detection accuracy of about 98% with a PMT and 94% with an APD as measured in Fig. 3.6(c), which is limited by polarization purity of the beams and detector dark counts.

### 3.3.4 Laser Stabilization

For the operations described above, laser frequency stabilization requirements are not rigorous. The final Doppler temperature is first order insensitive to frequency fluctuations around the optimal detuning, optical pumping transitions can be over saturated and kept on longer to eliminate effects of laser frequency changes and swapping between  $\sigma^+$  and  $\sigma^-$  polarized light on state detection cancels out slow laser drift issues. Therefore, we found locking the 493 and 650 nm laser frequencies with a calibrated wavemeter utilizing a slow software based feed forward PID loop sufficient. The wavemeter (HighFinesse WSU10) measures up to 16 different wavelengths and after each measurement the voltage output that is dependent on the difference from set point is applied to the laser grating piezo actuator to correct for drifts. Estimated long term stability of this passive locking technique is around 1 MHz, which is satisfactory for the  $^{138}\text{Ba}^+$  operations.

Typical fluctuations of 493 and 650 nm laser optical power outputs or fiber coupling efficiencies do not have significant effect on the  $^{138}\text{Ba}^+$  operations either, hence a noise eater setup was not utilized here.

### 3.3.5 Magnetic Field Stabilization

In the multi-species approach, communication qubits do not require long coherence times as photonic entanglement generated between them gets quickly transferred to nearby memory qubits where this entanglement can be stored for longer and used later. However, the short coherence time of the Zeeman  $^{138}\text{Ba}^+$  qubits,

which is a result of high magnetic field sensitivity of about 2.8 kHz/mG, might result in errors during transfer operations.

The effect of magnetic field noise can be characterized by looking at the time evolving density matrix of a single qubit prepared in  $|\psi\rangle = \frac{1}{\sqrt{2}}(|\downarrow\rangle + |\uparrow\rangle)$ :

$$\rho(t) = \frac{1}{2}(|\downarrow\rangle\langle\downarrow| + |\uparrow\rangle\langle\uparrow| + e^{i\phi(t)}|\uparrow\rangle\langle\downarrow| + e^{-i\phi(t)}|\downarrow\rangle\langle\uparrow|) \quad (3.2)$$

where  $\phi(t) = \int_0^t \Delta(t')dt'$  in the frame rotating with qubit frequency and  $\Delta(t)$  is the noise term. The unknown evolution introduced to the density matrix due to this extra phase results in decoherence.

Rather than directly measuring the coherence time of  $^{138}\text{Ba}^+$ , magnetic field sensitive transition between the  $|\Downarrow\rangle$  and  $|F = 1, m_F = -1\rangle$  states of the  $^{171}\text{Yb}^+$  is utilized in a Ramsey experiment for faster data acquisition. In our typical lab environment, we have measured a coherence time  $T_2^*$  of around 200  $\mu\text{s}$ , which indicates 100  $\mu\text{s}$  for the  $^{138}\text{Ba}^+$  qubits due to approximately twice the magnetic field sensitivity. Since this coherence time is comparable to the time required for transferring information [67], we have implemented a setup for canceling background magnetic field noise to extend the coherence time.

A major contribution to magnetic field noise comes from lab equipment and power lines at 60 Hz and higher harmonics. We have verified this effect by looking at the correlation between the frequency separation of the  $|\Downarrow\rangle$  and  $|F = 1, m_F = -1\rangle$  states on  $^{171}\text{Yb}^+$  and the phase of the 60 Hz signal (see Fig. 3.8 (a)). Since the experiments are typically conducted on a much faster time scale than  $1/(60 \text{ Hz})$ , the result is sampling of the line signal at different magnetic field amplitudes rather

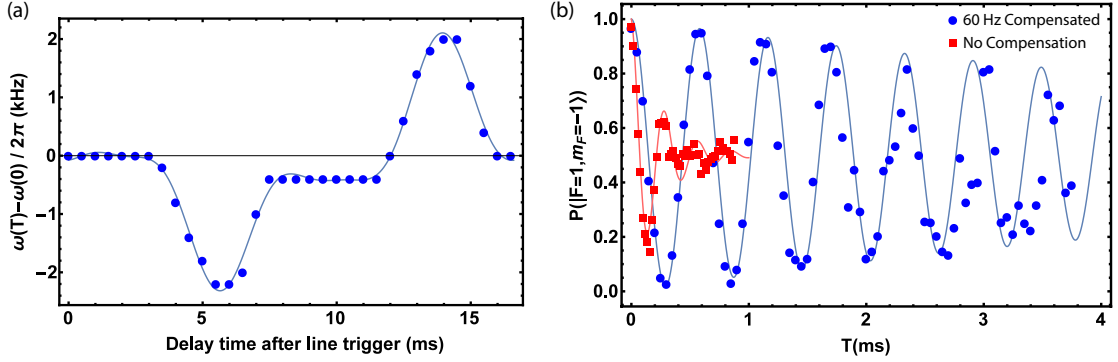


Figure 3.8: (a) The effect of 60 Hz noise is evident with shown dependence of frequency splitting between  $|\downarrow\rangle$  and  $|F = 1, m_F = -1\rangle$  states on  $^{171}\text{Yb}^+$  ( $\omega$ ) to delay from the line trigger. Blue circles are the experimental measurements on  $^{171}\text{Yb}^+$  and the line is a fit with 60 Hz and higher harmonics sinusoids. (b) A Ramsey experiment conducted on  $^{171}\text{Yb}^+$ , driving transition between  $|\downarrow\rangle$  state and magnetic field sensitive  $|F = 1, m_F = -1\rangle$  state. Coherence time is measured without (red squares) and with (blue circles) 60 Hz compensation fields created using a SRS DS345 waveform generator which is line triggered. The factor of two higher magnetic field sensitivity of  $^{138}\text{Ba}^+$  qubit results in half of the coherence time measured here.

than dephasing on individual experiments.

A common way of solving this issue involves conducting experiments at a given point of the 60 Hz cycle, such that the magnetic field is same for each experiment [68, 69]. Since photonic entanglement generation is probabilistic, this method is not feasible for us as it will greatly reduce the entanglement generation rate between two modules. Instead, initially we have tried an active magnetic field stabilization technique where the fluctuations are measured with a detector placed close to the trapped ions and corrections are fed forward to a coil to cancel them. However, due to shielding effects and spatial inhomogeneity of magnetic field amplitude, it is difficult to use a detector outside the vacuum chamber to actively stabilize the field at the ion position [6].

As an alternative, we employed a passive approach where we use an arbitrary waveform generator to apply a magnetic field at 60 Hz and higher harmonics with full phase and amplitude control to minimize the background noise the ions experience. Looking at the coherence time of the qubit directly as we adjust the parameters, we were able to push this coherence time to about 8 ms as shown in Fig. 3.8 (b). As the background field is subject to changes with addition of experimental apparatus or alterations in the orientation of the existing electrical equipment, occasional recalibration of the parameters is generally necessary once in a few days timescale. Even though it has not been realized in our setup yet, this process can be automatized with existing experimental control electronics to make it more robust against such disturbances.

Active stabilization of DC bias magnetic field is challenging for similar reasons, and unlike 60 Hz there is no periodicity that can be utilized in a passive technique since these effects are mostly caused by operation of nearby elevator, movements of magnetized materials around the lab etc. Therefore, experiments where small detunings can introduce large errors are conducted at after work hours to circumvent this problem. A feed forward stabilization technique might be a valid solution to this problem, where the qubit splitting is measured at regular intervals interrupting other experimental sequences, and a controlled current source counters the changes in DC field.

### 3.3.6 Atom-Photon Entanglement

As the first step on using  $^{138}\text{Ba}^+$  as our communication qubits we have shown entanglement between the atom and the emitted photon following a procedure similar to Ref. [23, 70]. On this experiment, we initialize the qubit to the  $|\downarrow\rangle$  state, and weakly excite it to the  $^2P_{1/2} |m_J = +1/2\rangle$  level with  $\sigma^+$  laser light (see Fig. 1.2). This weak excitation beam is generated by applying a 5 ns RF pulse to the same AOM used in the qubit detection setup, and the corresponding transition probability was observed to be approximately 10%. The ion decays back to the  $|\downarrow\rangle$  state emitting a  $\sigma^+$  polarized photon, or to the  $|\uparrow\rangle$  state with a  $\pi$  photon. We collect the photons perpendicular to the quantization axis (see Fig. 3.9(a)); therefore  $\pi$  photons are registered as vertical polarized in the ( $|V\rangle$ ) basis while the  $\sigma^+$  photons are registered as horizontally polarized ( $|H\rangle$ ). Along this photon collection axis, approximately a factor of two radiation intensity difference between  $\pi$  and  $\sigma^+$  photons is counterbalanced with decay probabilities from Clebsch-Gordon coefficients, resulting in a joint atom-photon state:

$$|\psi\rangle = \frac{1}{\sqrt{2}}(|\downarrow H\rangle + |\uparrow V\rangle) . \quad (3.3)$$

Following a photon detection event, the qubit state is measured to look at the correlation between atom and photon states in the original basis. Next, the same measurement is done by rotating polarization state, without changing the atomic qubit:

$$R_p(4\theta) \equiv \begin{pmatrix} \cos 2\theta & \sin 2\theta \\ \sin 2\theta & -\cos 2\theta \end{pmatrix}, \quad |H\rangle = \begin{pmatrix} 1 \\ 0 \end{pmatrix}, \quad |V\rangle = \begin{pmatrix} 0 \\ 1 \end{pmatrix},$$

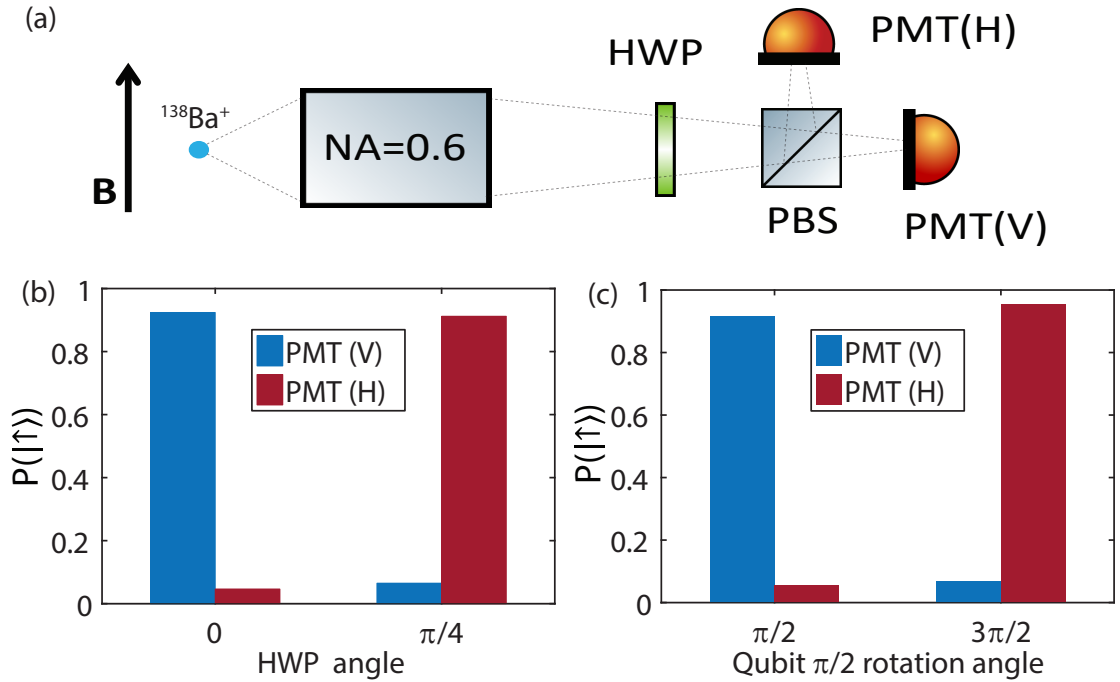


Figure 3.9: (a) Single photon collection setup. (b) Photon polarization qubit is rotated with a half wave plate (HWP) and we look at atom-photon qubit state correlations after photon detection on PMT's. (c) Photon polarization is rotated to diagonal basis by fixing HWP at  $\pi/8$ ,  $|H\rangle \rightarrow |H\rangle - |V\rangle$  and  $|V\rangle \rightarrow |H\rangle + |V\rangle$ . Photon detection on PMT's project the atom to a superposition (PMT(H)  $\rightarrow |\uparrow\rangle + |\downarrow\rangle$ ) and PMT(V)  $\rightarrow |\uparrow\rangle + |\downarrow\rangle$ ). Following detection of a photon, we coherently rotate these superposition states to  $|\downarrow\rangle$  and  $|\uparrow\rangle$  with a  $\pi/2$  rotation to show atom-photon entanglement.

$$R_p(\pi)|\psi\rangle = \frac{1}{\sqrt{2}}(|\downarrow V\rangle + |\uparrow H\rangle) \quad (3.4)$$

where a  $\pi$  rotation on photon polarization qubit,  $R_p(\pi)$ , is realized by changing the HWP angle by  $\pi/4$  (see Fig. 3.9 (b)).

Entanglement is verified by repeating the correlation measurement in the rotated basis of both atom and photon qubits. First, the polarization state is rotated to the diagonal basis by applying a  $\pi/2$  rotation:

$$\begin{aligned} R_p(\pi/2)|\psi\rangle &= \frac{1}{2}(|\downarrow(V+H)\rangle + |\uparrow(V-H)\rangle) \\ &= \frac{1}{2}(|(\downarrow+\uparrow)V\rangle + |(\downarrow-\uparrow)H\rangle) \end{aligned} \quad (3.5)$$

and following a photon detection event, the atomic qubit is rotated by  $\pi/2$  around the equatorial axis defined by rotation phase  $\phi$ :

$$\begin{aligned} R_a(\pi/2, \phi = \pi/2)R_p(\pi/2)|\psi\rangle &= \frac{1}{2}(|\downarrow H\rangle + |\uparrow V\rangle) \\ R_a(\pi/2, \phi = 3\pi/2)R_p(\pi/2)|\psi\rangle &= \frac{1}{2}(|\downarrow V\rangle + |\uparrow H\rangle). \end{aligned} \quad (3.6)$$

Correlation measurements between atom and photon qubit states in these rotated bases are shown in Fig. 3.9 (c). We calculate entanglement fidelity to be  $F \geq 0.86$  from these measurements. Errors are attributed to polarization mixing due to non-zero solid angle (10%) [36], multiple photon scattering from the atom in excitation step (3%) and imperfect state initialization/detection (1%). These error sources can be eliminated in future implementations by collecting photons along the quantization axis [13, 71] and using pulsed lasers for fast excitation of atoms [15].

### 3.3.6.1 Electric Dipole Transition with Fast Pulses

In addition to preventing multiple excitation events, usage of pulsed lasers for fast dipole transitions allow achieving a better temporal overlap on a beamsplitter between the photon wave-packets coming from separate atoms. The speed requirements of these transitions depend on the lifetime of the atom in the excited state; errors due to temporal mismatch scale as  $1 - e^{-\Delta/\tau}$  where  $\Delta$  is the arrival time difference and  $\tau$  is the lifetime of the excited state.

Previous experiments on  $^{171}\text{Yb}^+$  have been conducted using a Spectra Physics Tsunami Ti:Sapphire laser [15, 26, 72] that produces 1 ps pulses to realize  $\Delta \ll \tau$ , and the same laser can be tuned to 986 nm region to be frequency doubled to produce 493 nm light for  $^{138}\text{Ba}^+$ . However, this laser does not produce as much optical power at this wavelength compared to 740 nm and the operation might be compromised with air absorption lines which requires purging of the laser cavity. As a more robust alternative, we have tried a Toptica FemtoFiber pro TVIS fiber based laser to attain short laser pulses.

Fig. 3.10 (a) shows the spectrum of these laser's pulses, as measured with a optical spectrum analyzer. This laser produces 500 ps pulses with a repetition rate of approximately 80 MHz and a pulse picker is used for extinction of subsequent pulses. The electric field produced by the laser drives the optical dipole transition between  $^2S_{1/2}$  and  $^2P_{1/2}$  level in which the angle of this rotation on Bloch sphere is given by:

$$\theta = \frac{\mu}{\hbar} \int_0^T E(t) dt = \frac{\mu}{\hbar} \int_0^T \sqrt{I(t)} dt \quad (3.7)$$

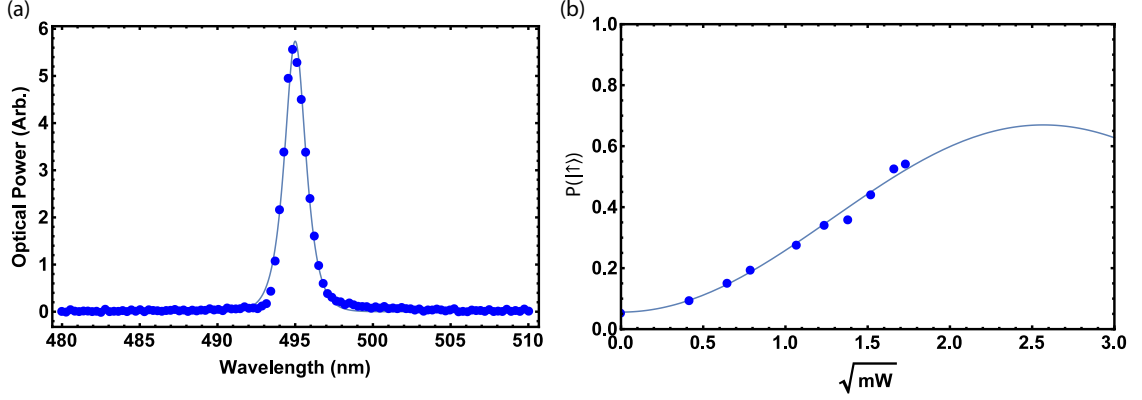


Figure 3.10: (a) Optical spectrum is measured and fit to a hyperbolic secant function. The width is consistent with transform limited 500 ps pulses in the time domain. (b) Excitation probability to  ${}^2P_{1/2}|m_J = -1/2\rangle$  with a single  $\pi$  polarized pulse is measured by looking at the qubit state. From the excited level, decay probabilities are 1/3 and 2/3 to the states  $|\downarrow\rangle$  and  $|\uparrow\rangle$ , respectively. Hence, the maximum probability of finding the qubit in the  $|\uparrow\rangle$  state approaches 66 % following the excitation and spontaneous emission. Available optical power from the laser was not sufficient to drive a complete  $\pi$  pulse even with a considerably well focused beam of  $5 \mu\text{m}$  waist. (Data is presented with permission from Toptica Inc.)

where  $T$  is the total pulse duration and  $I(t)$  is the optical intensity. For measuring this transition probability,  ${}^{138}\text{Ba}^+$  initialized in  $|\downarrow\rangle$  is excited with a  $\pi$  polarized pulse to  ${}^2P_{1/2}|m_J = -1/2\rangle$ . Then, probability of this excitation and creating a single photon that is entangled with the atom is:

$$\begin{aligned}
 P({}^2P_{1/2}|m_J = -1/2\rangle) &= \sin^2(\theta/2) \\
 &= \sin^2(\alpha\sqrt{I}).
 \end{aligned}
 \tag{3.8}$$

For this calculation, the intensity of light field is assumed to be constant through the pulse duration, however, this assumption does not affect the fitting to experimental results (see Fig. 3.10 (b)) as the overall factors on the intensity can be taken out of the integral given in Eq. 3.7.

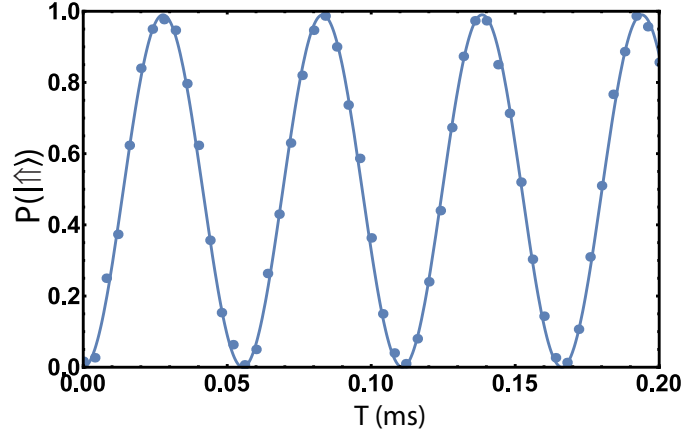


Figure 3.11: The Rabi flopping between the  $|\downarrow\rangle$  and  $|\uparrow\rangle$  states in  $^{171}\text{Yb}^+$  with microwave radiation. Oscillating field is applied for a total time of  $T$  to the qubit initialized in the  $|\downarrow\rangle$  state.

### 3.4 Coherent Rotations with 355-532 nm Pulses

The  $^{171}\text{Yb}^+$  qubit states can be rotated by applying microwaves resonant with the hyperfine splitting. Similarly, RF radiation is suitable for manipulation of  $^{138}\text{Ba}^+$  Zeeman qubits. These oscillating fields drive magnetic dipole transitions and Rabi flopping between the qubit states. Hence, single qubit gates can be easily implemented by directing a microwave horn or a inductive coil towards the trap and applying a few watts of resonant radiation (see Fig. 3.11).

The long wavelengths of the microwave and RF fields result in negligible momentum transfer to atoms during interaction, therefore, they do not resolve the collective motion of the ions and are not suitable for two qubit entanglement operations through utilization of spin dependent forces [73]. Large magnetic field gradients can be applied to increase the effective coupling to the motion for realization of multi qubit entangling gates [74, 75] but this approach is beyond the scope of this thesis

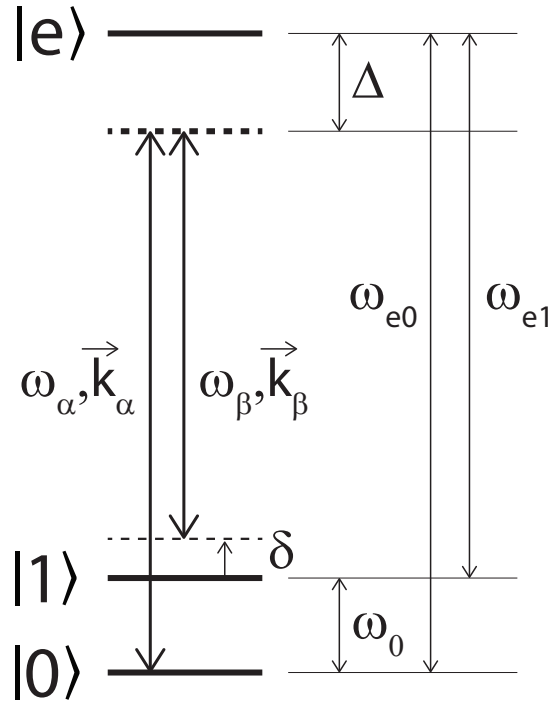


Figure 3.12: Diagram of two photon stimulated Raman transition between ground states  $|0\rangle$  and  $|1\rangle$  via coupling to the excited state  $|e\rangle$ . Two fields that couple the qubit states are detuned from the excited state by  $\Delta$ .

work.

In contrast to microwave and RF fields, optical beams can impart considerable momentum with two photon stimulated Raman transitions where the ground states are coupled through a virtual level. Fig. 3.12 shows the general theme of this operation and specific considerations for  $^{171}\text{Yb}^+$  and  $^{138}\text{Ba}^+$  qubits will be carried out later in this section. Even though frequency combs of a pulsed laser are used in the experiments conducted here, these optical fields can be treated as continuous waves (CW) without loss of generality [37, 45].

Two optical fields that drive electric dipole transitions between the states

$|0\rangle \leftrightarrow |e\rangle$  and  $|1\rangle \leftrightarrow |e\rangle$  are given by:

$$\vec{E}_n(\mathbf{r}) = \frac{E_n}{2} \vec{\epsilon}_n (e^{i(\mathbf{k}_n \cdot \mathbf{r} - \omega_n t - \phi_n)} + e^{-i(\mathbf{k}_n \cdot \mathbf{r} - \omega_n t - \phi_n)}) \quad (3.9)$$

with  $n = \alpha, \beta$  and polarization  $\vec{\epsilon}_n$ . This interaction Hamiltonian in a frame rotating with  $\omega_\beta$  and under the rotating wave approximation is [73]:

$$\begin{aligned} H_I &= -\mathbf{D} \cdot \mathbf{E} \\ &= \frac{\hbar}{2} [(g_{0,\alpha} e^{i(\mathbf{k}_\alpha \cdot \mathbf{r} - \delta t - \phi_\alpha)} |e\rangle \langle 0| + \text{h.c.}) + (g_{1,\beta} e^{i(\mathbf{k}_\beta \cdot \mathbf{r} - \phi_\beta)} |e\rangle \langle 1| + \text{h.c.}) + \Delta |e\rangle \langle e|] \end{aligned} \quad (3.10)$$

and single photon Rabi frequencies are  $g_{i,n} = -D_i \cdot \epsilon_n E_n / 2\hbar$ . With detuning from the excited level much larger than the atomic linewidth and coupling terms ( $\Delta \gg \gamma, |g_{i,n}|^2$ ) excited state population is adiabatically eliminated [76]. Under another rotating wave approximation:

$$H_I = \frac{\hbar}{2} [(\Omega e^{-i(\Delta \mathbf{k} \cdot \mathbf{r} - \delta t - \Delta \phi)} |1\rangle \langle 0| + \text{h.c.}) + \chi_0 |0\rangle \langle 0| + \chi_1 |1\rangle \langle 1|] \quad (3.11)$$

where  $\Delta \mathbf{k} = \vec{k}_\alpha - \vec{k}_\beta$  and  $\Delta \phi = \phi_\alpha - \phi_\beta$ . The two photon Rabi frequency is given by  $\Omega = g_{1,\alpha}^* g_{0,\beta} / 2\Delta$  and AC Stark shifts are  $\chi_i = [|g_{i,\alpha}|^2 + |g_{i,\beta}|^2] / 4\Delta$ .

The motion in the harmonic trap can be considered at this stage. By assuming  $\Delta \mathbf{k}$  is along the  $x$  direction, we are only interested in motion along this axis. The position operators for two atoms are expressed as:

$$\mathbf{r}_i = x_i + q_{i,\text{IP}}(a + a^\dagger) + q_{i,\text{OP}}(b + b^\dagger) \quad (3.12)$$

where  $x_i$  is the equilibrium position,  $a, a^\dagger$  and  $b, b^\dagger$  are the usual creation and annihilation operators, for the in-phase and out-of-phase modes, respectively. When

two atoms are of the same mass:

$$\begin{aligned}
q_{1,\text{IP}} &= q_{2,\text{IP}} = \frac{1}{\sqrt{2}} \sqrt{\frac{\hbar}{2M\omega_{\text{IP}}}} \\
q_{1,\text{OP}} &= -q_{2,\text{OP}} = \frac{1}{\sqrt{2}} \sqrt{\frac{\hbar}{2M\omega_{\text{OP}}}}
\end{aligned} \tag{3.13}$$

where  $M$  is the ion mass and  $\omega_{\text{IP}}$ ,  $\omega_{\text{OP}}$  are the normal mode frequencies. These coefficients are analyzed in detail for the unequal mass case in the next chapter. In the vibrational mode interaction frame, the Hamiltonian for two ions ( $m=1,2$ ) is:

$$\begin{aligned}
H_I &= \frac{\hbar}{2} \sum_{m=1,2} \left[ (\Omega_m e^{-i[\eta_{m,\text{IP}}(ae^{-i\omega_{\text{IP}}t} + a^\dagger e^{i\omega_{\text{IP}}t}) + \eta_{m,\text{OP}}(be^{-i\omega_{\text{OP}}t} + b^\dagger e^{i\omega_{\text{OP}}t})]} \right. \\
&\times e^{i\delta t} e^{-i(\Delta k x_m - \Delta\phi)} |1_m\rangle \langle 0_m| + \text{h.c.}) + \chi_{0,m} |0, m\rangle \langle 0, m| + \chi_{1,m} |1, m\rangle \langle 1, m| \left. \right] \tag{3.14}
\end{aligned}$$

where the Lamb-Dicke parameters are defined as  $\eta = \Delta k q$ . The optical phases are introduced on this interaction through  $e^{-i(\Delta k x_m - \Delta\phi)}$ . Since the two Raman beams are originating from the same laser source, fluctuations in the optical phase of the laser does not cause shot to shot variations. However, if the beams are not propagating through the same optical path, for instance when it is required for addressing motion to introduce a  $\Delta \mathbf{k}$  vector, relative optical path length fluctuations might be a source of decoherence on long timescales. The optical paths are passively stable on the majority of experiments presented here, which are generally around 100-200  $\mu\text{s}$ . Even though these non-copropagating qubit rotations are sensitive to the optical phases as analyzed here, multi qubit entangling gates can be made insensitive by introducing special geometries [33, 73].

In the resolved sideband limit ( $\Omega \ll \omega_{\text{IP}}$ ,  $\omega_{\text{OP}}$ ), frequency difference between the Raman beams can be tuned to drive transitions between different qubit states

and eigenstates of the harmonic motion [38]. With  $\delta$  adjustments, a stationary term emerges from the interaction Hamiltonian and other terms can be eliminated with a rotating wave approximation.

With  $\delta$  set to 0, including the AC Stark shift effects, the transitions between the internal qubit states are driven while the motional quanta is preserved. This carrier interaction is given by [38]:

$$H_I^{car} = \frac{\hbar}{2} \sum_{m=1,2} \sum_{n_{IP}, n_{OP}} (\Omega_m \mathcal{D}_{m, n_{IP}, n_{OP}} e^{i(\Delta k x_m - \Delta \phi)} \sigma_+^{(m)} + \text{h.c.}) |n_{IP}, n_{OP}\rangle \langle n_{IP}, n_{OP}| \quad (3.15)$$

where spin operators are  $\sigma_+ = |1\rangle\langle 0|$ ,  $\sigma_- = |0\rangle\langle 1|$ , and the Debye-Waller factor  $\mathcal{D}_{m, n_{IP}, n_{OP}} = e^{-\frac{1}{2}(\eta_{m, IP}^2 + \eta_{m, OP}^2)} \mathcal{L}_{n_{IP}}(\eta_{m, IP}^2) \mathcal{L}_{n_{OP}}(\eta_{m, IP}^2)$  suppresses the carrier transition for large phonon occupation states through Laguarre polynomial of order  $n_{IP}$  or  $n_{OP}$  [38].

A collective motional state can be decreased or increased by one quanta accompanying a spin flip. These interactions are called red and blue sideband transitions, respectively. Setting  $\delta = -\omega_{IP}$  gives the red sideband interaction:

$$H_I^{\text{RSB}} = \frac{\hbar}{2} \sum_{m=1,2} (\eta_{m, IP} \Omega_m e^{i(\Delta k x_m - \Delta \phi)} \mathcal{D}'_{n, n-1} \sigma_+^{(m)} a + \text{h.c.}) \quad (3.16)$$

and with  $\delta = \omega_{IP}$ , blue sideband interaction is:

$$H_I^{\text{BSB}} = \frac{\hbar}{2} \sum_{m=1,2} (\eta_{m, IP} \Omega_m e^{i(\Delta k x_m - \Delta \phi)} \mathcal{D}'_{n, n+1} \sigma_+^{(m)} a^\dagger + \text{h.c.}) \quad (3.17)$$

where  $\mathcal{D}'$  is the sideband Debye-Waller factors [38, 73]. These interactions between fields and the atoms respectively drive  $|0, n\rangle \leftrightarrow |1, n-1\rangle$  and  $|0, n\rangle \leftrightarrow |1, n+1\rangle$  transitions.

### 3.4.1 The Rabi Frequencies

The analysis above only considered the single excited level. In reality, there are multiple levels involved in these stimulated Raman transitions on  $^{171}\text{Yb}^+$  and  $^{138}\text{Ba}^+$  atoms. These paths and their detunings from the excited level are shown in Fig. 3.13 and the Rabi frequency depends on the coupling strength to these levels and the detuning from them:

$$\Omega = \sum_i \frac{g_{0,i}^* g_{1,i}}{2\Delta_i}. \quad (3.18)$$

The single photon Rabi frequencies,  $g_{ij}$ , show the coupling strength and are given by [76]:

$$g_{ij} = C\gamma\sqrt{\frac{I}{2I_{\text{sat}}}} \quad (3.19)$$

where  $C$  is the Clebsch-Gordan coefficient,  $I_{\text{sat}}$  is the saturation intensity and  $\gamma$  is the natural linewidth of the transition.

Using the coupling coefficients given in Figs. 3.3 and 3.1 for the paths given in Fig. 3.13 result in:

$$\Omega_{\text{Yb}} = \frac{I}{12} \left[ -\frac{\gamma_1^2}{\Delta_1 I_{\text{sat},1}} + \frac{\gamma_2^2}{\Delta_2 I_{\text{sat},2}} \right] \quad (3.20)$$

$$\Omega_{\text{Ba}} = \frac{I\sqrt{2}}{12} \left[ -\frac{\gamma_1^2}{\Delta_1 I_{\text{sat},1}} + \frac{\gamma_2^2}{\Delta_2 I_{\text{sat},2}} \right] \quad (3.21)$$

where subscript 1 (2) is used to describe parameters corresponding to  $^2P_{1/2}$  ( $^2P_{3/2}$ ) level of the corresponding atom.

Plugging in the atomic parameters given in Table 3.1, the Rabi frequencies

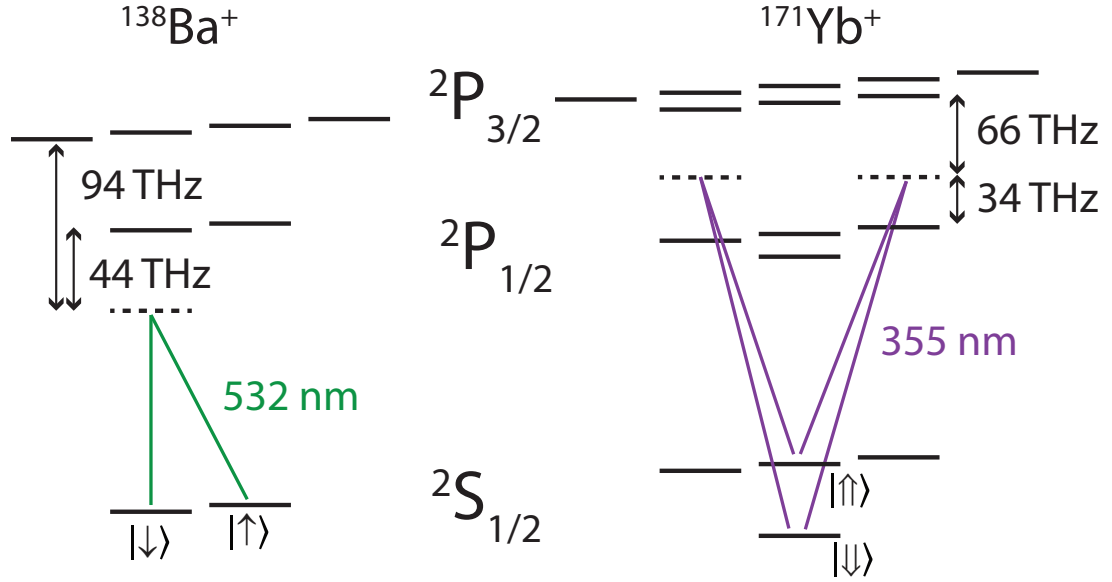


Figure 3.13: 532 and 355 nm photons off-resonantly couple to both  $^2P_{1/2}$  and  $^2P_{3/2}$  levels for stimulated Raman transitions. Detuning from the excited levels are shown for these wavelengths.

Excited Level	$^{171}\text{Yb}^+$		$^{138}\text{Ba}^+$	
	$^2P_{1/2}$	$^2P_{3/2}$	$^2P_{1/2}$	$^2P_{3/2}$
Natural Linewidth $\gamma/2\pi$ (MHz)	19.7	25.8	15.1	17.7
Saturation Intensity $I_{sat}$ (mW/cm <sup>2</sup> )	51.0	95.1	16.4	35.7
Detuning $\Delta/2\pi$ (THz)	34	-66	-44	-94

Table 3.1: Natural linewidth, saturation intensity and detuning from excited levels for  $^2P_{3/2}$  and  $^2P_{1/2}$  levels. Saturation intensity is calculated using  $I_{sat} = \frac{\hbar\gamma\omega_e^3}{12\pi c^2}$  where  $\omega_e$  is the resonant transition frequency from the ground state.

are:

$$\Omega_{\text{Yb}} = I \left( -2.75 \times 10^{-2} \frac{\text{Hz}}{\text{mW}/\text{cm}^2} \right) \quad (3.22)$$

$$\Omega_{\text{Ba}} = I \left( 2.62 \times 10^{-2} \frac{\text{Hz}}{\text{mW}/\text{cm}^2} \right). \quad (3.23)$$

Even though the destructive interference between the two paths in  $^{138}\text{Ba}^+$  decreases the Rabi frequency, lower saturation intensities and stronger coupling due to larger dipole matrix elements result in a similar stimulated Raman transition rate for  $^{171}\text{Yb}^+$  and  $^{138}\text{Ba}^+$  with an equal 355 and 532 nm optical intensity.

### 3.4.2 Differential Stark Shifts

In addition to driving transitions, the optical fields cause AC Stark shifts of the qubit states. Frequencies can be adjusted to account for this change in the qubit splitting. However, intensity fluctuations might introduce detuning errors in this case, therefore these Stark shift effects should be avoided if possible to prevent errors in the qubit operations.

In  $^{171}\text{Yb}^+$ , these shifts are [76]:

$$\chi_{\downarrow} = \frac{I}{24} \left[ \frac{\gamma_1^2}{\Delta_1 I_{\text{sat},1}} + \frac{2\gamma_2^2}{\Delta_2 I_{\text{sat},2}} \right] \quad (3.24)$$

$$\chi_{\uparrow} = \frac{I}{24} \left[ \frac{\gamma_1^2}{(\Delta_1 - \omega_{hf}) I_{\text{sat},1}} + \frac{\gamma_2^2}{2(\Delta_2 - \omega_{hf}) I_{\text{sat},2}} + \frac{3\gamma_2^2}{2(\Delta_2 + \omega'_{hf} - \omega_{hf}) I_{\text{sat},2}} \right] \quad (3.25)$$

where  $\omega'_{hf}$  is the hyperfine splittings in  $^2P_{3/2}$  manifold. For  $^{138}\text{Ba}^+$ , with the Raman

beams polarized as shown in Fig. 3.13 they are:

$$\chi_{\downarrow} = \frac{I}{24} \left[ \frac{\gamma_1^2}{\Delta_1 I_{\text{sat},1}} + \frac{2\gamma_2^2}{\Delta_2 I_{\text{sat},2}} + \frac{3\gamma_2^2}{\Delta_2 I_{\text{sat},2}} \right] \quad (3.26)$$

$$\chi_{\uparrow} = \frac{I}{24} \left[ \frac{\gamma_1^2}{\Delta_1 I_{\text{sat},1}} + \frac{2\gamma_2^2}{\Delta_2 I_{\text{sat},2}} + \frac{2\gamma_1^2}{\Delta_1 I_{\text{sat},1}} + \frac{\gamma_2^2}{\Delta_2 I_{\text{sat},2}} \right] \quad (3.27)$$

where first two terms in each expression are contributions of the  $\pi$  polarized component and the rest are from  $\sigma^-$  light. Small Zeeman shifts on the levels are ignored for simplicity as  $\Delta \gg \delta_{\text{Zeeman}}$ . From symmetry,  $\pi$  light shifts the levels by the same amount and the differential shift comes mostly due to the circular polarized field. Comparing these shifts to the effective coupling rate of the qubit states gives:

$$\frac{\chi_{\downarrow} - \chi_{\uparrow}}{\Omega_{Yb}} = 1.87 \times 10^{-4} \quad (3.28)$$

$$\frac{\chi_{\downarrow} - \chi_{\uparrow}}{\Omega_{Ba}} = 0.707. \quad (3.29)$$

This significant differential Stark shift on  $^{138}\text{Ba}^+$  can be minimized by introducing  $\sigma^+$  light to equalize the shifts on the  $|\uparrow\rangle$  and  $|\downarrow\rangle$  states as shown in Fig. 3.14. Even though this results in a lower Rabi frequency, detuning errors that might stem from long term intensity drifts can be minimized with this approach.

### 3.4.3 Re-pumping from $^2D_{5/2}$ Level with an Orange LED

The spontaneous emission rate is very small during stimulated Raman interactions as excited states are negligibly populated with large detuning from these levels. These rates are given by [77]:

$$\Gamma_{Yb} = \frac{2\pi I}{24} \left[ \frac{\gamma_1^3}{\Delta_1^2 I_{\text{sat},1}} + \frac{2\gamma_2^3}{\Delta_2^2 I_{\text{sat},2}} \right] \quad (3.30)$$

$$\Gamma_{Ba} = \frac{2\pi I}{8} \left[ \frac{\gamma_1^3}{\Delta_1^2 I_{\text{sat},1}} + \frac{\gamma_2^3}{\Delta_2^2 I_{\text{sat},2}} \right] \quad (3.31)$$

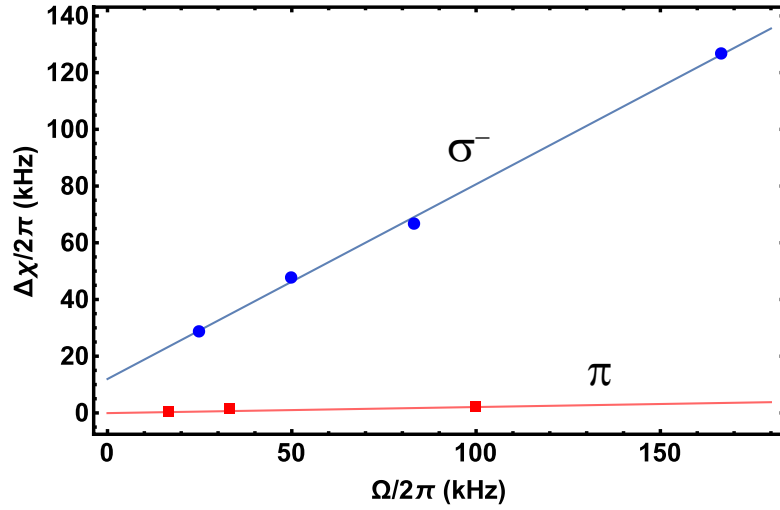


Figure 3.14: The Rabi frequency ( $\Omega$ ) and corresponding shift in the qubit splitting ( $\Delta\chi = \chi_{\downarrow} - \chi_{\uparrow}$ ) is measured on the  $^{138}\text{Ba}^+$  atom where 532 nm pulses are used for the rotation. Blue line shows a fit to measurement where only  $\pi$  and  $\sigma^-$  field is incident for transition. This result in a considerable differential shift with a slope of  $\Delta\chi/\Omega = 0.69$ , which agrees with the calculated value of 0.707. Rotation of the  $\sigma^-$  polarized light to linear results in an equal  $\sigma^+$  contribution and reduces the differential shift. Red squares shows the measurements with this adjustment, and a fit gives  $\Delta\chi/\Omega = 0.02$ . With more sensitive measurements, it might be possible to get even lower differential shifts on  $^{138}\text{Ba}^+$  qubit.

where the configuration that minimizes the differential Stark shift for the  $^{138}\text{Ba}^+$  atom is considered. Consequently, the probability of spontaneous emission during a  $\pi$  pulse calculated using Eqns. 3.21 and 3.31 gives:

$$P_{\text{Yb}} = 3.2 \times 10^{-6} \quad , \quad P_{\text{Ba}} = 5.9 \times 10^{-6}. \quad (3.32)$$

Even though these probabilities are negligible for each individual rotation, the atomic level structure of the  $^{138}\text{Ba}^+$  atom introduces another complexity to the system. The atom decays to the  $^2S_{1/2}$  or  $^2D_{3/2}$  manifolds after spontaneous emission from  $^2P_{1/2}$ . These events can be considered as a quantum gate error and operations restart in the next experimental cycle. However, decays from  $^2P_{3/2}$  might end up in  $^2D_{5/2}$ , and the  $^{138}\text{Ba}^+$  qubit will stay in this long lived metastable level for  $\tau = 31$  s, resulting in down time on the system if a re-initialization mechanism is not available. Only considering spontaneous emission from the  $^2P_{3/2}$  level and accounting for branching ratio of 0.215 (see Fig. 2.4), the probability of populating  $^2D_{5/2}$  during a  $\pi$  pulse is  $1.8 \times 10^{-7}$ . Experimentally, the  $^{138}\text{Ba}^+$  atom is observed to go dark at a rate of a few per minute with the 532 nm laser in use.

To solve this issue, we have utilized a high intensity orange LED (Luxeon Star 617nm) on the optical setup which deshelves the atom from  $^2D_{5/2}$  levels through  $^2P_{3/2}$  with absorption of a 614 nm photon (see Fig. 3.15). The available optical power that can address this dipole transition is estimated to be  $\sim 100$  nW, only  $\sim 10^{-7}$  of the total 1W due to the large spectral distribution of the emitted light from the LED. With a measured  $\sim 30$  ms average deshelving time, this layout is sufficiently fast compared to the timescale over which the population gets trapped

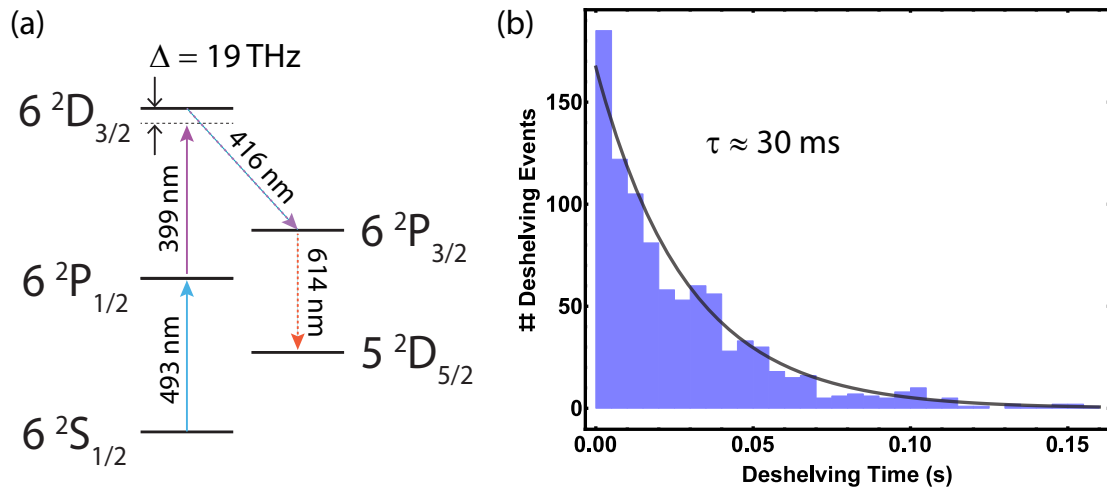


Figure 3.15: (a) Instead of relying on a 532 nm laser for trapping population at the  $^2D_{5/2}$  level, a 399 nm Yb photo-ionization laser is used for faster characterization of a 617 nm LED. With both 493 nm and 399 nm laser beams incident on the  $^{138}\text{Ba}^+$ , the ion is observed to go dark with an average rate of  $0.5\ \text{s}^{-1}$ . Suspected mechanisms that result in this behavior are shown here. (b) The fluorescence photons are monitored to measure average deshelving speed with the orange LED. While the cooling and Yb photo-ionization lasers are incident, a drop in the number of detected photons in a certain time window signals the occupation of the  $^2D_{5/2}$  level. During this process, the orange LED is kept on and the time the  $^{138}\text{Ba}^+$  atom stays dark is measured which corresponds the deshelving timescale.

and therefore provides a cheap and easy alternative to a laser that might otherwise be used for the same purpose.

### 3.4.4 Crosstalk Between the Qubits and Raman Beams

Crosstalk between 355 nm (532 nm) beams and the  $^{138}\text{Ba}^+$  ( $^{171}\text{Yb}^+$ ) qubit needs to be considered in our system as they couple to the  $^2P_{1/2}$  and  $^2P_{3/2}$  levels with a detuning of 238 THz (248 THz) and 187 THz (347 THz). This results in relative two photon Rabi frequencies:

$$\frac{\Omega_{Ba,355}}{\Omega_{Ba,532}} = \frac{\frac{1}{187} - \frac{1}{238}}{\frac{1}{44} - \frac{1}{94}} = 0.109, \quad \frac{\Omega_{Yb,532}}{\Omega_{Yb,355}} = \frac{\frac{1}{248} - \frac{1}{347}}{\frac{1}{34} + \frac{1}{66}} = 0.026 \quad (3.33)$$

on  $^{138}\text{Ba}^+$  and  $^{171}\text{Yb}^+$ , respectively, for equal 355 nm and 532 nm optical intensities on the Raman beams.

Since the qubit splitting frequencies are different, when set for driving transitions on their corresponding qubit, the 355 (532) nm Raman beams are unlikely to address the transitions on  $^{138}\text{Ba}^+$  ( $^{171}\text{Yb}^+$ ) qubit. However, due to usage of the pulsed laser, there might be unwanted comb teeth combinations that drive crosstalk transitions. This issue can be circumvented by adjusting the magnetic field amplitude to change the  $^{138}\text{Ba}^+$  qubit frequency or the repetition rate of the pulsed laser if the cavity is accessible.

Additionally, the number of possible cross transitions might be partially reduced by setting the polarization specifically for each of the individual qubits. For instance, elimination of the  $\pi$  polarized component on the 355 nm beams effectively suppresses any transition they can drive on  $^{138}\text{Ba}^+$  qubit. In contrast, the same

approach does not apply to 532 nm beams as they need to have both  $\pi$  and  $\sigma^-$  components for rotations on the  $^{138}\text{Ba}^+$  qubit.

## Chapter 4: Normal Mode Structure of Ytterbium-Barium Ion Chain

In this chapter, the collective motion of the  $^{171}\text{Yb}^+ - ^{138}\text{Ba}^+$  Coulomb chain in a linear Paul RF trap is reviewed. The modes of motion play an essential part in entanglement of nearby qubits [14, 28, 78, 79], hence it is important to understand how confinement dynamics are affected with unequal mass of the ions in a multi-species system.

### 4.1 Normal Mode Eigenfrequencies and Eigenvectors

These calculations follow the methods described in Ref. [80–82] where the atoms are considered to be well localized around their equilibrium position and subject to small vibrations compared to separations in between them.

#### 4.1.1 Longitudinal Modes

First, we look at the longitudinal direction in which the confinement is the weakest and consequently the atoms line up on this axis. The total kinetic energy is:

$$T = \frac{m_1 \dot{x}_1^2}{2} + \frac{m_2 \dot{x}_2^2}{2} \quad (4.1)$$

where atom 1 (2) position is defined as  $x_1 < 0$  ( $x_2 > 0$ ). Potential energy is given by the expression:

$$U = \frac{kx_1^2}{2} + \frac{kx_2^2}{2} + \frac{1}{x_2 - x_1} \quad (4.2)$$

with trap spring constant  $k = m_1\omega_1^2 = m_2\omega_2^2$ . Here, the angular frequencies  $\omega_{1,2}$  correspond to motional frequency of single confined atom. Equilibrium positions are determined by:

$$\begin{aligned} \frac{\partial U}{\partial x_1} &= 0 \Rightarrow x_1^{(0)} = -(1/2k^2)^{2/3} \\ \frac{\partial U}{\partial x_2} &= 0 \Rightarrow x_2^{(0)} = (1/2k^2)^{2/3} \end{aligned} \quad (4.3)$$

which are independent of the mass since the trapping potential only interacts with the charges. Assuming a harmonic collective motion around the equilibrium positions, potential energy can be approximated with a Taylor expansion truncated to second order:

$$U \approx \frac{1}{2} \frac{\partial^2 U}{\partial x_1^2} \Big|_0 x_1^2 + \frac{1}{2} \frac{\partial^2 U}{\partial x_2^2} \Big|_0 x_2^2 + \frac{\partial^2 U}{\partial x_1 \partial x_2} \Big|_0 x_1 x_2 \quad (4.4)$$

where the first derivative terms vanish at equilibrium and positions are replaced with displacements  $x_i - x_i^{(0)} \rightarrow x_i$ . Dynamics are described by the Lagrangian  $L = T - V$  and equations of motion are found from:

$$-\frac{\partial}{\partial t} \frac{\partial T}{\partial \dot{x}_i} = \frac{\partial U}{\partial x_i}. \quad (4.5)$$

and putting Eqns. 4.1, 4.4 here result in:

$$\begin{aligned} -m_1 \ddot{x}_1 &= \frac{\partial^2 U}{\partial x_1^2} \Big|_0 x_1 + \frac{\partial^2 U}{\partial x_1 \partial x_2} \Big|_0 x_2 \\ -m_2 \ddot{x}_2 &= \frac{\partial^2 U}{\partial x_1 \partial x_2} \Big|_0 x_1 + \frac{\partial^2 U}{\partial x_2^2} \Big|_0 x_2 \end{aligned} \quad (4.6)$$

These equations are represented in the following matrix form:

$$\omega_1^2 \begin{pmatrix} 2 & -1 \\ -1/\alpha & 2/\alpha \end{pmatrix} \begin{pmatrix} x_1 \\ x_2 \end{pmatrix} = \omega^2 \begin{pmatrix} x_1 \\ x_2 \end{pmatrix} \quad (4.7)$$

where ansatz  $x_i(t) = x_i e^{i\omega t}$  is used and  $\alpha = m_2/m_1$ . For equal mass ions,  $\alpha = 1$ , this eigenvalue problem has the well-known center of mass and breathing mode solutions with the values of:

$$\begin{aligned} X_{\text{CM}} &= \begin{pmatrix} 1/\sqrt{2} \\ 1/\sqrt{2} \end{pmatrix}, & \omega_{\text{CM}} &= \omega_1 \\ X_{\text{BR}} &= \begin{pmatrix} 1/\sqrt{2} \\ -1/\sqrt{2} \end{pmatrix}, & \omega_{\text{BR}} &= \sqrt{3}\omega_1 \end{aligned} \quad (4.8)$$

In the general case, the eigenvalues are:

$$\begin{aligned} \omega_{\text{OP}} &= \omega_1 \sqrt{\frac{\sqrt{\alpha^2 - \alpha + 1} + \alpha + 1}{\alpha}} \\ \omega_{\text{IP}} &= \omega_1 \sqrt{\frac{-\sqrt{\alpha^2 - \alpha + 1} + \alpha + 1}{\alpha}} \end{aligned} \quad (4.9)$$

with corresponding normalized eigenvectors:

$$\begin{aligned} X_{\text{OP}} &= \left( -\frac{\alpha + \sqrt{(\alpha - 1)\alpha + 1} - 1}{\sqrt{(\alpha + \sqrt{(\alpha - 1)\alpha + 1} - 1)^2 + 1}}, \frac{1}{\sqrt{(\alpha + \sqrt{(\alpha - 1)\alpha + 1} - 1)^2 + 1}} \right) \\ X_{\text{IP}} &= \left( \frac{-\alpha + \sqrt{(\alpha - 1)\alpha + 1} + 1}{\sqrt{(-\alpha + \sqrt{(\alpha - 1)\alpha + 1} + 1)^2 + 1}}, \frac{1}{\sqrt{(-\alpha + \sqrt{(\alpha - 1)\alpha + 1} + 1)^2 + 1}} \right) \end{aligned} \quad (4.10)$$

Instead of center of mass and breathing labels, a more appropriate in-phase (IP) and out-of-phase (OP) description is used here. Mass ratio dependence of mode motional amplitudes and frequencies are shown in Fig. 4.1 and 4.2.

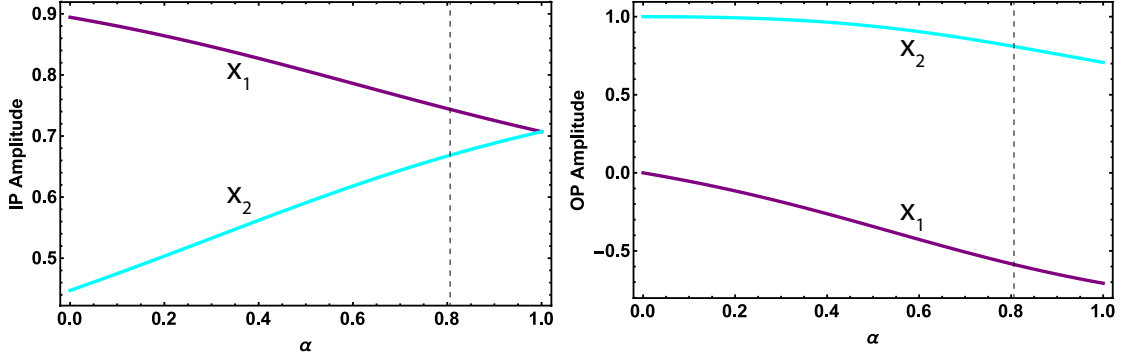


Figure 4.1: Dependence of motional amplitudes  $x_{1,2}$  to mass ratio for in-phase (IP) and out-of-phase (OP) modes. Dashed line shows  $^{138}\text{Ba}^+ \text{ } ^{171}\text{Yb}^+$  mass ratio of  $\approx 0.81$  where  $X_{\text{IP}} = (0.743, 0.668)$  and  $X_{\text{OP}} = (-0.587, 0.809)$

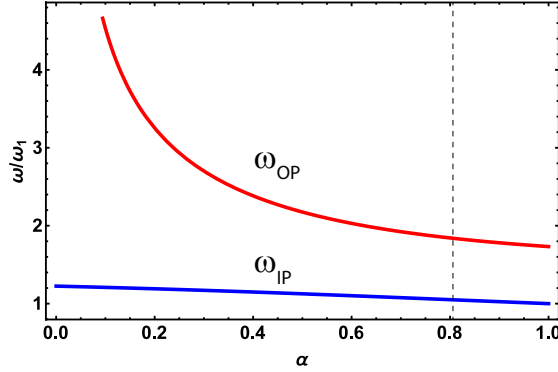


Figure 4.2: In-phase and out-of-phase mode frequencies normalized to single ion frequency of  $\omega_1$ . For  $^{138}\text{Ba}^+ \text{ } ^{171}\text{Yb}^+$  corresponding frequencies are  $\omega_{\text{IP}} = 1.05 \omega_1$  and  $\omega_{\text{OP}} = 1.84 \omega_1$ .

### 4.1.2 Transverse Modes

Stronger confinement in the transverse direction compared to longitudinal axis results in reduced sensitivity to heating and thermal motion in entanglement operations [83]. Hence, it might be more advantageous to use these modes in a multi-species module.

Kinetic energy along this direction is given by:

$$T = \frac{m_1 \dot{z}_1^2}{2} + \frac{m_2 \dot{z}_2^2}{2} \quad (4.11)$$

and potential energy is:

$$U = \frac{k_T z_1^2}{2} + \frac{k_T z_2^2}{2} + \frac{1}{|r_2 - r_1|} \quad (4.12)$$

where  $k_T = m_1 \omega_T^2$  and  $\omega_T$  is the transverse frequency of single ion of mass  $m_1$ . The Coulomb component can be approximated with a Taylor expansion assuming displacement in the transverse direction is small compared to the separation between the ions:

$$\begin{aligned} \frac{1}{|r_2 - r_1|} &= \frac{1}{\sqrt{(x_1 - x_2)^2 + (z_1 - z_2)^2}} \\ &\approx \frac{1}{\Delta x} \left( 1 - \frac{(z_1 - z_2)^2}{2\Delta x^2} \right) \\ &= \frac{1}{\Delta x} - \frac{1}{2\Delta x^3} (z_1^2 + z_2^2 - 2z_1 z_2) \end{aligned} \quad (4.13)$$

The equilibrium position is again found by  $\frac{\partial U}{\partial z_i} = 0$  giving  $z_1^{(0)} = 0$  and  $z_2^{(0)} = 0$ .

Using equilibrium positions found in Eqn. 4.3 for  $\Delta x^3$ , the Lagrange equation of motion is:

$$\begin{pmatrix} \omega_T^2 - \frac{\omega_1^2}{2} & \frac{\omega_1^2}{2} \\ \frac{\omega_1^2}{2\alpha} & \frac{\omega_T^2}{\alpha} - \frac{\omega_1^2}{2\alpha} \end{pmatrix} \begin{pmatrix} z_1 \\ z_2 \end{pmatrix} = \omega^2 \begin{pmatrix} z_1 \\ z_2 \end{pmatrix} \quad (4.14)$$

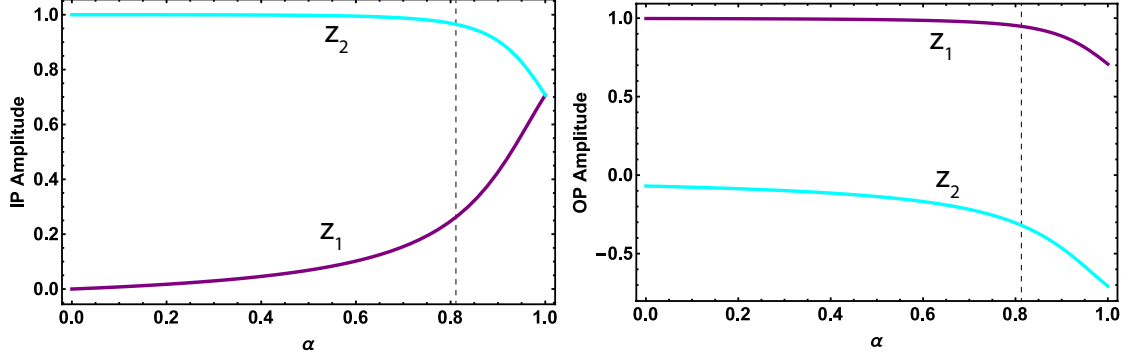


Figure 4.3: Dependence of motional amplitudes  $z_{1,2}$  to mass ratio for in-phase (IP) and out-of-phase (OP) modes. Dashed line shows  $^{138}\text{Ba}^+ - ^{171}\text{Yb}^+$  mass ratio of  $\approx 0.81$  where  $Z_{\text{IP}} = (0.256, 0.966)$  and  $Z_{\text{OP}} = (0.950, -0.312)$

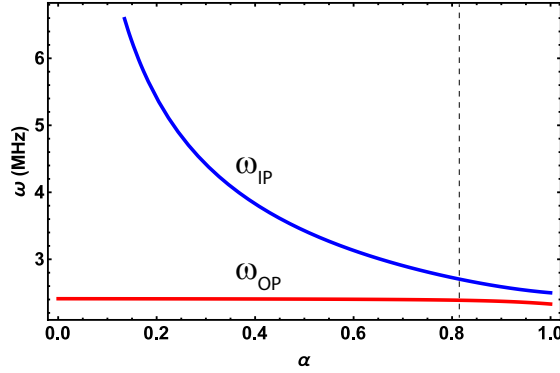


Figure 4.4: In-phase and out-of-phase mode frequencies in transverse direction. With single ion  $^{171}\text{Yb}^+$  frequencies of  $\omega_T = 2.5$  MHz and  $\omega_1 = 0.9$  MHz, the  $^{138}\text{Ba}^+ - ^{171}\text{Yb}^+$  chain frequencies are  $\omega_{\text{IP}} = 2.715$  MHz and  $\omega_{\text{OP}} = 2.39$  MHz.

For equal mass,  $\alpha = 1$ , this reproduces  $Z_{\text{IP}} = (1/\sqrt{2}, 1/\sqrt{2})$  with  $\omega_{\text{IP}} = \omega_T$  and  $Z_{\text{OP}} = (1/\sqrt{2}, -1/\sqrt{2})$  with  $\omega_{\text{OP}} = \sqrt{\omega_T^2 - \omega_1^2}$ . Motional amplitudes and mode frequencies for two ions with mass ratio  $m_2/m_1 = \alpha$  and typical single ion confinement potentials of  $\omega_T = 2.5$  MHz and  $\omega_1 = 0.9$  MHz are shown in Fig. 4.3 and 4.4.

Comparison of Fig. 4.1 and 4.3 reveal that, even with relatively close mass of  $^{171}\text{Yb}^+$  and  $^{138}\text{Ba}^+$ , there is a big mismatch in motional amplitudes for a given

transverse mode, whereas this mismatch is not as significant for longitudinal modes. Since the coupling of external fields to motional modes scales as  $\eta = \Delta\vec{k} \cdot \mathbf{Z}$ , the mismatch in mode amplitudes results in reduced entangling gate speeds as  $T_{\text{Gate}} \propto \frac{1}{\eta\Omega}$  [84, 85] where  $\Omega$  is the two photon Rabi frequency proportional to intensity  $I$  of the fields used and  $\Delta\vec{k} = \vec{k}_1 - \vec{k}_2$ . Limitations in available optical power in our setup resulted in switching to longitudinal modes to benefit from smaller mismatch for faster gate operations.

Before getting to experimental measurements, I present how the motional amplitudes are affected by confining potentials to complete this analysis. From Eqn. 4.10, it is clear that relative motion of the ions are not affected by the confining potentials and only depend on the mass ratio. The trapping potential determines the spread of the wavefunction,  $\sqrt{\frac{\hbar}{2m\omega}}$ , which is a common factor for both ions. In contrast, transverse mode structure depends on both the mass and confinement ratios,  $\frac{\omega_1}{\omega_T}$ , and Fig. 4.5 shows this dependence for the particular mass ratio of  $\alpha = \frac{m_{Ba}}{m_{Yb}} \approx 0.81$ .

As an additional note, a similar analysis shows that as the number of ions in the crystal chain increase, the mismatch on motional modes tend to decrease and utilization of transverse modes might become more practical.

## 4.2 Spectroscopy Measurements

The analysis of previous section is experimentally verified by resolving the motion of the ions with Raman spectroscopy. When two laser beams have a  $\Delta\vec{k}$

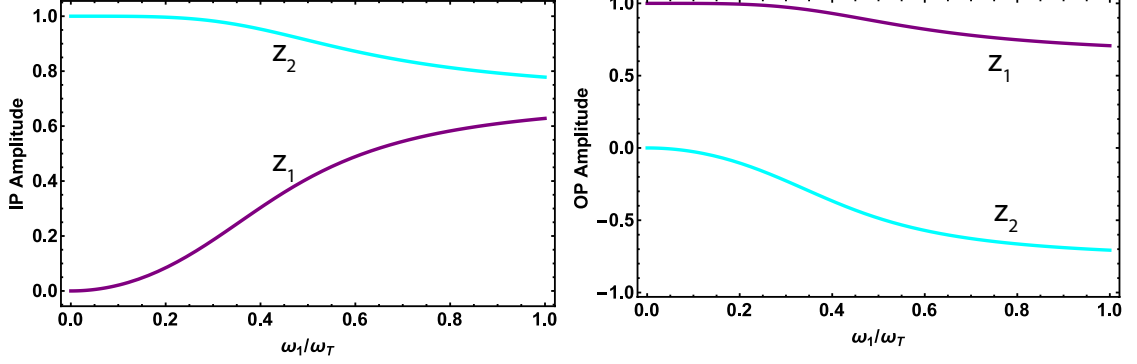


Figure 4.5: Weak longitudinal confinement results in bigger mismatch for the motional amplitudes in transverse modes. Therefore, increase in DC voltages to create a tighter trap in longitudinal direction indirectly helps in motional amplitude matching of  $^{171}\text{Yb}^+$  and  $^{138}\text{Ba}^+$  in transverse directions. However, as  $\omega_1$  approaches  $\omega_T$ , this analysis is likely to fail since the ions might realign along a weaker axis.

vector along a motional axis, transitions between different Fock states can be driven and the resonant Rabi frequencies are given by [38, 73]:

$$\begin{aligned}
 \Omega_{n,n} &\approx \Omega_0(1 - \eta^2 n) \\
 \Omega_{n,n-1} &\approx \Omega_0 \eta \sqrt{n} \\
 \Omega_{n,n+1} &\approx \Omega_0 \eta \sqrt{n+1}
 \end{aligned} \tag{4.15}$$

where  $\Omega_0$  is the base Rabi frequency,  $\eta = \Delta \vec{k} \cdot \vec{R}$  is the Lamb-Dicke parameter representing the coupling strength between the fields and the motion and  $n$  is the  $n^{\text{th}}$  eigenstate of the harmonic potential. The Rabi frequencies in Eqn. 4.15 correspond to carrier, red and blue sideband transitions in the given order.

Fig. 4.6 presents the beam geometry for addressing longitudinal and transverse modes. The 355 and 532 nm Raman beams coming from each direction are combined on the same optical path using suitable dichroic filters. Spatial adjustments are done on individual beams before combining to correct for the chromatic aberration of the

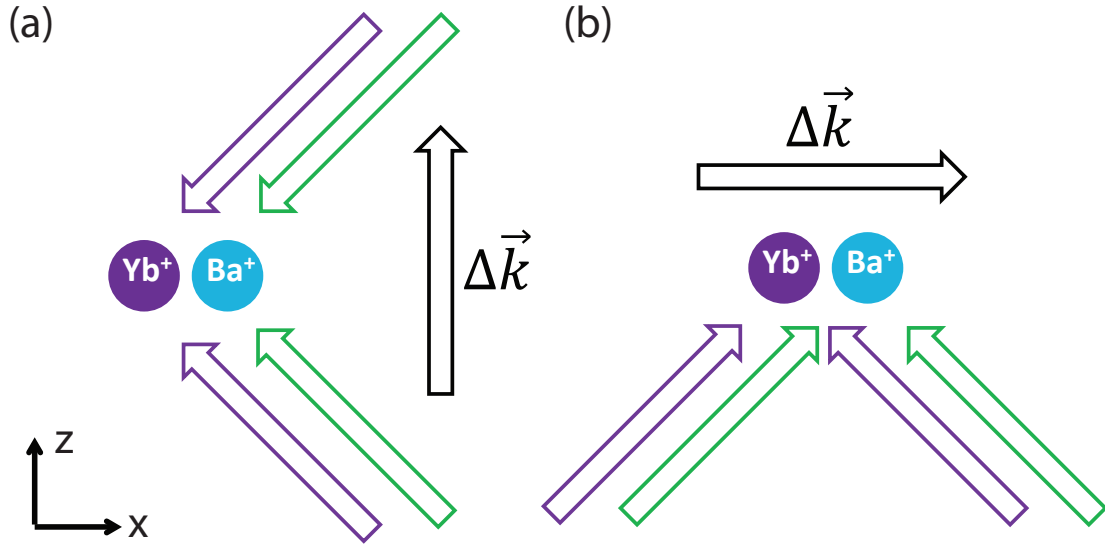


Figure 4.6: 355 nm (purple) and 532 nm (green) beams can address the (a) transverse,  $z$ , and (b) longitudinal,  $x$ , modes when there is a  $\Delta\vec{k}$  vector along the motional axis. By changing the direction of only one set of beams, switching between the two axes is possible.

final lens to have both beams focus at the same spot.

The frequency of these Raman beams are scanned, keeping the time and intensity constant, to reveal the motional spectrum (see Fig. 4.7). Even though traditionally transverse modes have been used in the previous works on this setup [13, 33, 45, 86], and among the Monroe group in general, a switch to longitudinal mode took place to benefit from better coupling of the ions to external fields.

### 4.3 Sub-Doppler Cooling with Electromagnetically Induced Transparency

Uncontrolled thermal motion of the ions can introduce decoherence into the system during interaction with external fields if the motional amplitude is compara-

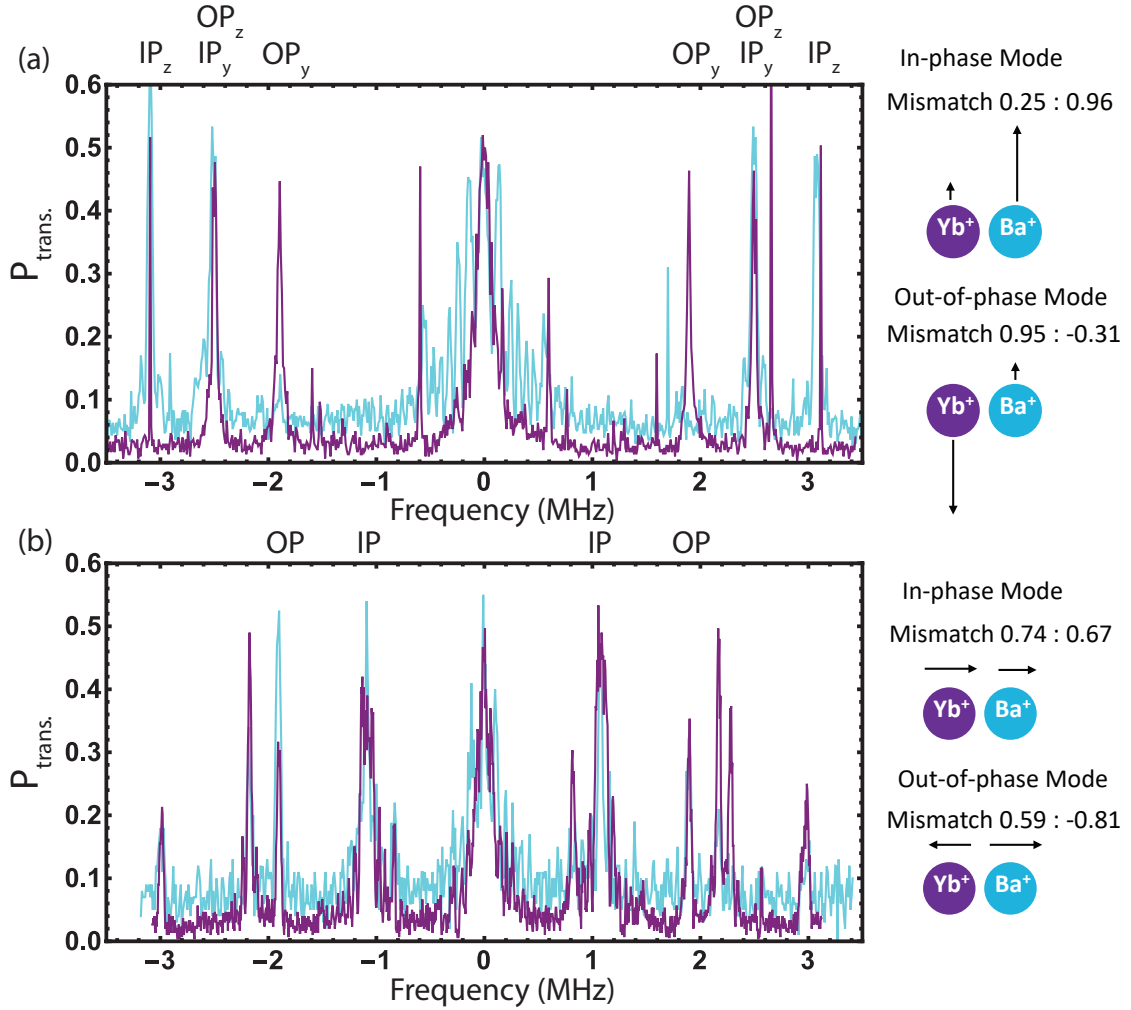


Figure 4.7: Motional spectrum centered around the carrier and negative (positive) frequencies correspond to red (blue) sideband transitions. Purple (Blue) line shows transition probability on  $^{171}\text{Yb}^+$  ( $^{138}\text{Ba}^+$ ) with 355 (532) nm Raman beams. (a) Both y and z transverse directions are resolved since  $\Delta\vec{k}$  had projection to both axes. In transverse directions, big mismatch between  $^{171}\text{Yb}^+$  and  $^{138}\text{Ba}^+$  motional amplitudes is evident from the width difference of spectral lines corresponding to IP and OP modes. (b) Closer motional amplitudes in the longitudinal direction results in similar width lines for both the IP and OP modes.

ble to the field wavelength. These errors are suppressed in the Lamb-Dicke regime ( $\eta^2(\bar{n} + 1) \ll 1$ ) [87], and achieving high fidelity quantum logic gates generally requires cooling motional modes nearly to the ground state ( $\bar{n} \approx 0$ ) [88]. Heating mechanisms, such as electric field noise [38], result in divergence from these limits and might be a limiting factor in quantum information processing in which long algorithms are implemented.

In a multi-species apparatus,  $^{138}\text{Ba}^+$  atoms can be utilized to be refrigerants as well to sympathetically cool the memory qubits in between quantum logic operations [89]. With Doppler cooling, the steady state temperature is limited to [90]:

$$k_B T = \frac{\hbar\gamma}{2}. \quad (4.16)$$

At this temperature, average phonon occupation numbers approximate to:

$$\hbar\omega\bar{n} \approx \frac{\hbar\gamma}{2} \Rightarrow \bar{n} \approx \frac{\gamma}{2\omega} \quad (4.17)$$

in which a typical motional mode frequency of  $\omega/2\pi = 2$  MHz results in  $\bar{n} \approx 4$  with  $\gamma/2\pi = 15.1$  MHz for the  $^{138}\text{Ba}^+$  atomic ion.

The heat can be further dissipated from Doppler cooled atoms by using narrower transitions [91], Raman sideband cooling [92] or electromagnetically induced transparency (EIT) techniques [93]. Compared to others, the EIT method can address a wider frequency range to simultaneously cool multiple modes and also provides faster cooling rates [94].

The EIT cooling mechanism is illustrated in Fig. 4.8. In a  $\Lambda$  system with one

excited and two ground states, a strong field creates atom-laser dressed states [95]:

$$|+\rangle = \cos\theta|e\rangle + \sin\theta|g_1\rangle \quad (4.18)$$

$$|-\rangle = \sin\theta|e\rangle - \cos\theta|g_1\rangle \quad (4.19)$$

$$(4.20)$$

where

$$\tan\theta = \frac{\sqrt{\Delta^2 + \Omega^2} - \Delta}{\Omega} \quad (4.21)$$

and the frequencies are shifted from bare states by:

$$\delta = \frac{1}{2}(\sqrt{\Delta^2 + \Omega^2} - \Delta). \quad (4.22)$$

A weak field ( $\Omega' < \Omega$ ) couples the state  $|g_2\rangle$  to dressed states with a Fano-like resonance [96, 97]. The coherent dark state at  $\Delta = \Delta'$  is utilized in suppressing the carrier transitions while a sharp resonance selectively addresses the red sideband  $|g_2, n\rangle \rightarrow |+, n-1\rangle$  when the induced light shift is set to the motional frequency,  $\delta = \omega$ . Therefore, each excitation event reduces the phonon number by one quanta and decays from  $|+\rangle$  back to ground states and restarts the process. The minimum average steady-state phonon number is given by [95]:

$$\bar{n} = \left(\frac{\gamma}{4\Delta}\right)^2 \quad (4.23)$$

with a maximum cooling rate of:

$$W^{max} \approx \frac{\gamma\omega}{4\sqrt{\Delta^2 + \Omega^2}}. \quad (4.24)$$

Depending on the requirements in the system,  $\Delta$  can be adjusted to find a compromise between the cooling rate and the minimum temperature achievable.

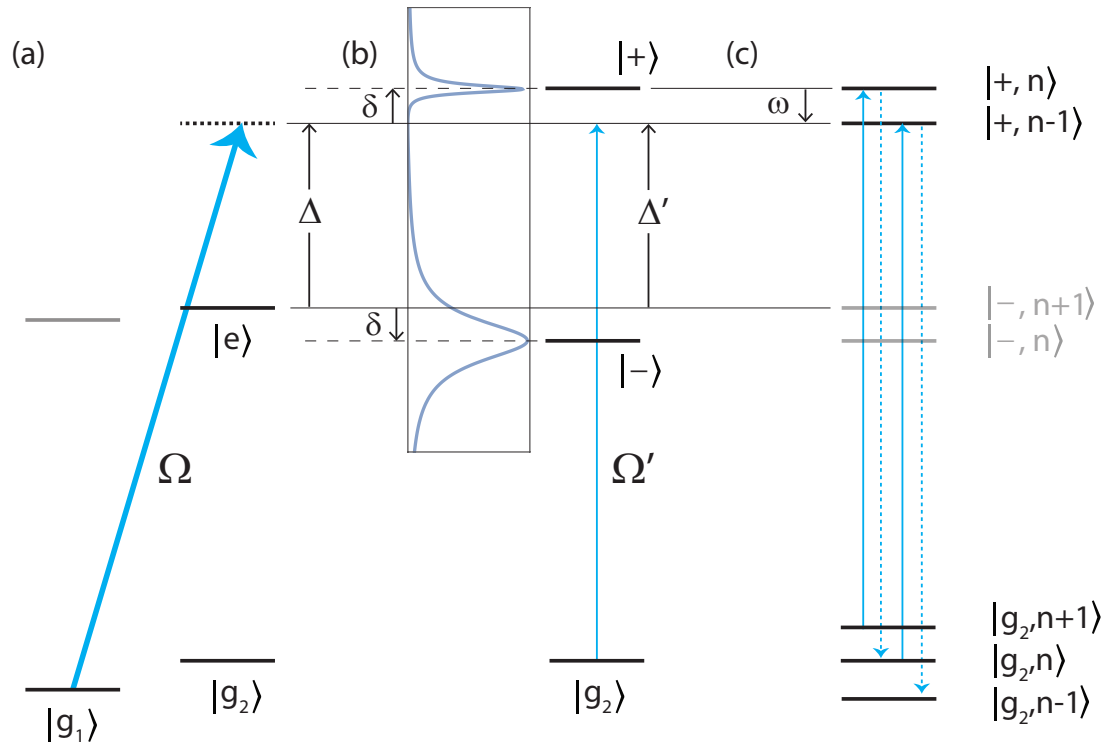


Figure 4.8: (a) Setting of the EIT cooling scheme on a  $\Lambda$  system, for instance utilizing one of the  $^2P_{1/2}$  and both  $^2S_{1/2}$  levels. (b) A strong beam introduces dressed states that are shifted by  $\delta$  from the bare state frequencies, and a weaker probe beam couples  $|g_2\rangle$  to  $|-\rangle$  and  $|+\rangle$  with a Lorentzian and Fano-like excitation spectrum, respectively. At  $\Delta = \Delta'$ , the absorption goes to zero for an ion at rest due to dark resonance, which results in suppression of carrier transitions. (c) The harmonic motion in the trap results in frequency modulation of the EIT beams if they have a  $\Delta\vec{k}$  along the motion axis, and red sideband transitions are driven when  $\delta = \omega$ . Or equivalently, missing  $\delta$  from the narrow resonance is supplied by the motion of the ion.

While the  ${}^2S_{1/2} \leftrightarrow {}^2P_{1/2} \leftrightarrow {}^2D_{3/2}$  configuration of  ${}^{138}\text{Ba}^+$  can possibly be used as the  $\Lambda$  system for the EIT cooling, the laser frequency stabilization requirements for realizing  $\Delta = \Delta'$  makes it impractical since  $\Omega$  and  $\Omega'$  are provided with two different lasers in this case. Instead, we use the  ${}^2S_{1/2}$  and  ${}^2P_{1/2}$  levels similar to Ref. [29], in which the correspondence to the general picture of Fig. 4.8(a) is:

$$|g_1\rangle \rightarrow |\downarrow\rangle, |g_2\rangle \rightarrow |\uparrow\rangle, {}^2P_{1/2} |m_J = +1/2\rangle \rightarrow |e\rangle. \quad (4.25)$$

To prevent population trapping in  ${}^2D_{3/2}$  states, the 650 nm laser is kept on during the EIT process but it does not participate in dynamics as the frequency difference between the red and green lasers is approximately  $\Delta$  and does not introduce extra coherent states.

In normal operating conditions, the frequency of the 493 nm laser is locked to:

$$(\omega_{\text{ge}} - \omega_{\text{laser}})/2\pi \approx 80 \text{ MHz} \quad (4.26)$$

and the AOMs are used to shift this set frequency close to resonance for operations described in the previous chapter. EIT beams are created by using AOMs with a center frequency around 200 MHz, which results in  $\Delta/2\pi \approx 120$  MHz. The strong  $\sigma^+$  beam that dresses the states is sent through the same fiber which is used for resonant circular polarized beams of state detection/initialization operations as shown in Fig. 3.7. For the weak probe field, the  $\pi$  polarized beam is sent through another fiber such that  $\vec{k}_\sigma - \vec{k}_\pi$  has a component along the motional axis of interest (set for cooling longitudinal motion in this thesis work). Additionally, the AOM drive frequency difference needs to match the splitting between  $|\downarrow\rangle \leftrightarrow |\uparrow\rangle$  to satisfy  $\Delta = \Delta'$ .

Even though the 493 nm laser is subject to frequency fluctuations since it is only passively stabilized, these drifts have negligible effect on EIT cooling performance. First, the Stark shift,  $\delta$ , on the dressed state is first order insensitive to changes in detuning,  $\Delta$ , as evident from Eqn. 4.22 with typical  $\Delta \gg \delta = \omega$  and  $\Delta > \Omega$  conditions. In addition, as both  $(\Omega, \sigma^+, \Delta)$  and  $(\Omega', \pi, \Delta')$  fields are produced from the same laser, detuning shifts are common mode. Hence, the  $\Delta = \Delta'$  optimum condition is satisfied for EIT cooling even with a noisy laser source. It should be noted that, due to magnetic field noise, there can be deviations from this ideal situation. However, with typical noise amplitude of the order 1 mG,  $^{138}\text{Ba}^+$  qubit splitting frequency only changes a few kHz which is not resolved with wide EIT features.

Fig. 4.9 shows the absorption spectrum and time dynamics of the EIT cooling scheme employed on a co-trapped  $^{171}\text{Yb}^+ - ^{138}\text{Ba}^+$  crystal. The atoms are first Doppler cooled and then EIT cooling is applied to  $^{138}\text{Ba}^+$  while  $^{171}\text{Yb}^+$  is kept on dark. The temperature of the crystal is extracted from the measured asymmetry on the longitudinal sidebands [38] with non-copropagating Raman transitions on  $^{171}\text{Yb}^+$  with 355 nm pulses. Additionally, Fig. 4.10 shows the longitudinal spectrum of a Doppler and EIT cooled multi-species chain where  $^{171}\text{Yb}^+$  is used to extract information on the collective motion.

Using the tools demonstrated here, it should be possible to sympathetically cool  $^{171}\text{Yb}^+$  atoms using  $^{138}\text{Ba}^+$  in between quantum logic gates for achieving higher fidelity operations. Since the qubit used for communication purposes is re-initialized before every entanglement trial, possible crosstalk between refrigerant and communi-

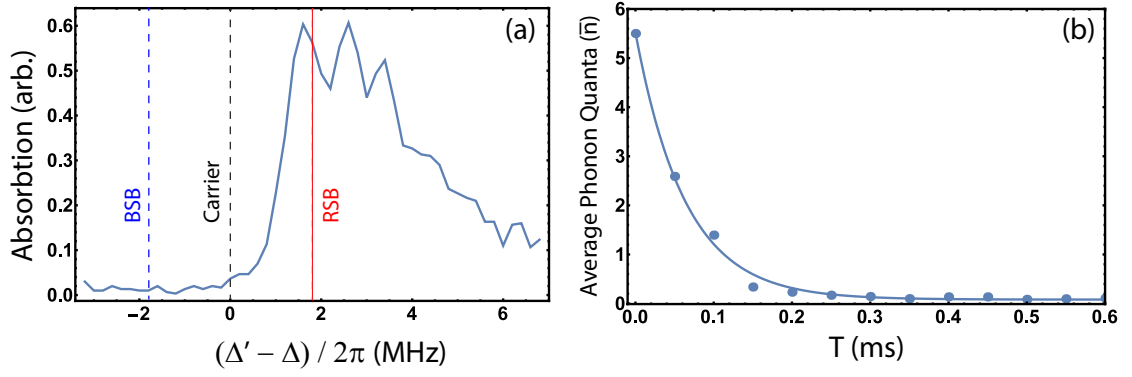


Figure 4.9: (a) The frequency of  $\pi$  polarized beam ( $\Delta'$ ) is scanned, while keeping  $\Delta$  fixed, to reveal Fano-like spectrum. A simple threshold method is used for defining absorption units, where the vertical axis depicts the fraction of events in which the detected number of 493 nm photons from  $^{138}\text{Ba}^+$  in a time window of  $200 \mu\text{s}$  is above the background level. When  $\Delta = \Delta'$ , carrier and blue sideband (BSB) transitions are suppressed and red sideband (RSB) transitions dissipate phonons from the crystal. With the broad spectrum spanning a few MHz, multiple modes can be cooled simultaneously. (b) The average phonon number in OP mode with frequency  $\omega_{\text{OP}}/2\pi \approx 1.8$  MHz is read out using  $^{171}\text{Yb}^+$  after an EIT cooling duration of T on neighbor  $^{138}\text{Ba}^+$ . The final average phonon quanta reach  $\bar{n} \approx 0.06$  in about  $300 \mu\text{s}$ .

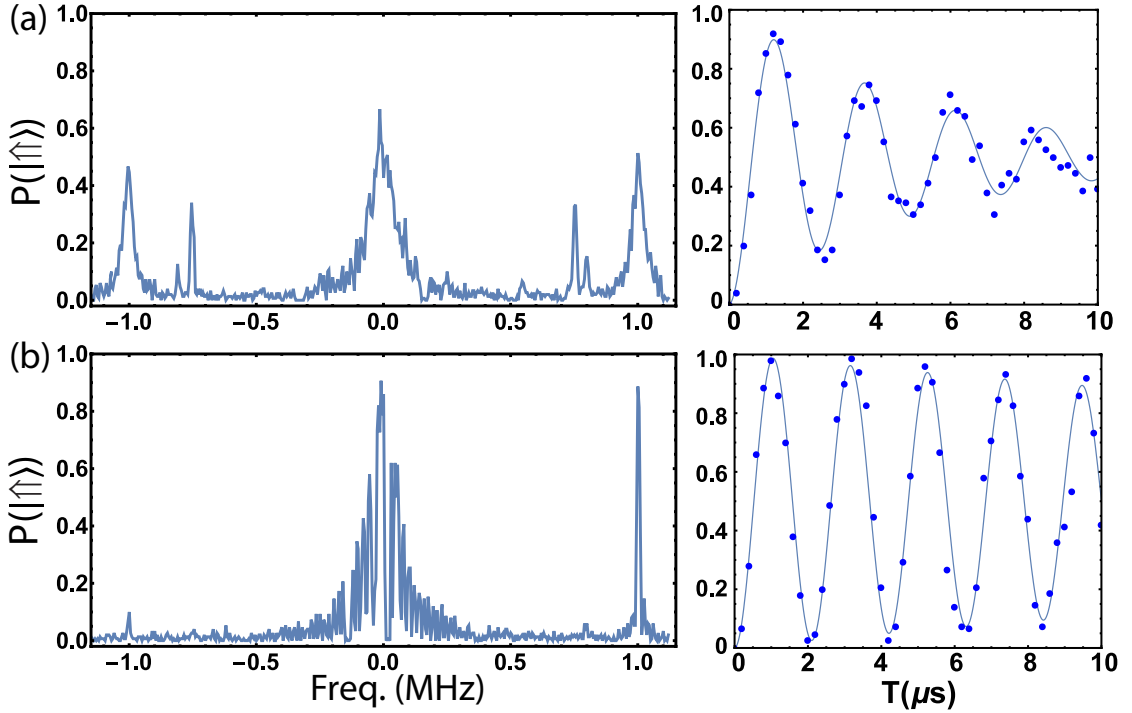


Figure 4.10: Partial spectrum of  $^{171}\text{Yb}^+ - ^{138}\text{Ba}^+$  chain and Rabi flops on  $^{171}\text{Yb}^+$  carrier transition with non-copropagating 355nm Raman beams on (a) Doppler and (b) EIT cooled atoms. Duration of the Raman interaction is  $30 \mu\text{s}$  for both scans. Peaks around 1 MHz correspond to IP mode,  $\omega_{\text{IP}}$ , which is cooled to  $\bar{n} \approx 0.1$  with the EIT technique. Weaker peaks around 0.8 MHz correspond to phonon exchange frequencies between different modes,  $\omega_{\text{OP}} - \omega_{\text{IP}}$ . Since the phonon occupation number effects carrier Rabi frequency (see Eqn. 4.15), oscillation quickly vanishes in a Doppler cooled atom due to timescale differences between oscillations corresponding to different Fock states. In contrast, the oscillations persist for longer with the EIT cooling employed.

cation  $^{138}\text{Ba}^+$  qubits would not pose the same problem encountered between memory and communication qubits. Therefore,  $^{138}\text{Ba}^+$  atoms can be utilized for both tasks in the same ion chain.

## Chapter 5: Phonon Mediated Interactions between Ytterbium and Barium Ions

The analysis in the previous chapter shows that the Coulomb force between proximate ions results in quantized collective motion in a RF Paul trap. These phonon modes can be utilized directly in the Cirac-Zoller (CZ) scheme as a bus to transfer information between communication and memory qubits [28, 85] or spin-dependent forces can be used in Mølmer-Sørensen (MS) interactions [78] for generating entanglement between  $^{171}\text{Yb}^+ - ^{138}\text{Ba}^+$  and several of these entangling gates can be combined for information swap operations [67]. In this chapter, I analyze these two different interactions and present our experimental results on a  $^{171}\text{Yb}^+ - ^{138}\text{Ba}^+$  chain.

### 5.1 Cirac-Zoller Interactions

In 1995, Cirac and Zoller proposed using common modes of motion as a bus to introduce a conditional phase shift on qubit states for entanglement operations between two ions on a string [85]. Stringent requirements of achieving ground state occupation in the collective motional mode and individual addressing to qubits makes this scheme less attractive compared to MS operations (to be discussed in

detail in next section) in quantum information processing. Nevertheless, the CZ interaction picture offers a conceptually simple way of transferring information from one qubit to the other and it is worth investigating.

### 5.1.1 Coherent Information Transfer Operation

Since the 355 nm and 532 nm Raman beams only drive transitions on their respective  $^{171}\text{Yb}^+$  and  $^{138}\text{Ba}^+$  ions, the individual addressing requirement is easily achieved without any particular effort on creating tightly focused beams. In addition, the EIT cooling described previously provides near ground state initialization for better performance on CZ interactions.

Starting with  $^{138}\text{Ba}^+$  in a general superposition state that is to be transferred to an initialized  $^{171}\text{Yb}^+$  qubit:

$$|\psi\rangle_{Ba^+} = \alpha|\downarrow\rangle + e^{i\phi_0}\beta|\uparrow\rangle, \quad |\psi\rangle_{Yb^+} = |\downarrow\rangle \quad (5.1)$$

and the collective motion bus in the ground state,  $|n\rangle = |0\rangle$ , gives the joint state of:

$$|\Psi_1\rangle = \alpha|\downarrow\rangle|\downarrow\rangle|0\rangle + e^{i\phi_0}\beta|\uparrow\rangle|\downarrow\rangle|0\rangle. \quad (5.2)$$

Application of a RSB  $\pi$  rotation on the  $^{138}\text{Ba}^+$  qubit leads to:

$$\begin{aligned} |\Psi_2\rangle &= \alpha|\downarrow\rangle|\downarrow\rangle|0\rangle - e^{i(\phi_0-\phi_{532})}\beta|\downarrow\rangle|\downarrow\rangle|1\rangle \\ &= |\downarrow\rangle|\downarrow\rangle(\alpha|0\rangle - \beta e^{i(\phi_0-\phi_{532})}|1\rangle) \end{aligned} \quad (5.3)$$

where the  $^{138}\text{Ba}^+$  superposition is mapped to the collective motion with an additional optical phase difference between the two beams driving the transition ( $\phi_{532} =$

$\phi_{\text{RSB},1} - \phi_{\text{RSB},2}$ ) imprinted on the state. Since the state  $|n\rangle = |-1\rangle$  does not exist, the  $\alpha$  portion remains unchanged with this operation while  $\beta$  part undergoes  $|\downarrow\rangle|1\rangle \leftrightarrow |\uparrow\rangle|0\rangle$  transition. Note that the realization of  $|n\rangle = |0\rangle$  is critical here for perfect mapping of qubit state to motion. This state acquires a phase under time evolution:

$$|\Psi_2(\tau)\rangle = |\downarrow\rangle|\downarrow\rangle(\alpha|0\rangle - \beta e^{i(\phi_0 - \phi_{532} + \phi_\tau)}|1\rangle) \quad (5.4)$$

where  $\phi_\tau = \omega_m \tau$  with the motional mode frequency of  $\omega_m$ . The superposition is mapped onto  $^{171}\text{Yb}^+$  by application of another RSB  $\pi$  pulse, this time using 355 nm Raman beams on the  $^{171}\text{Yb}^+$  :

$$\begin{aligned} |\Psi_3\rangle &= |\downarrow\rangle(\alpha|\downarrow\rangle|0\rangle - e^{i(\phi_0 - \phi_{532} + \phi_\tau + \phi_{355})}\beta|\uparrow\rangle|0\rangle) \\ &= |\downarrow\rangle|0\rangle(\alpha|\downarrow\rangle - e^{i(\phi_0 - \phi_{532} + \phi_\tau + \phi_{355})}\beta|\uparrow\rangle) \end{aligned} \quad (5.5)$$

where  $\phi_{355}$  is the optical phase coming from the 355 nm laser fields. This step finalizes the state transfer from  $^{138}\text{Ba}^+$  to  $^{171}\text{Yb}^+$ . In addition to amplitudes  $\alpha$  and  $\beta$ , the phase information needs to be transferred coherently for a full state mapping. These phase issues will be investigated in the next section in conjunction with the experimental setup.

### 5.1.2 Experimental Results

For the experimental demonstrations, we followed the procedure outlined in Ref. [28] where the operation is performed between  $^9\text{Be}^+$  and  $^{27}\text{Al}^+$ . In the first experiment, the  $^{138}\text{Ba}^+$  qubit is prepared in a superposition state with the stimulated

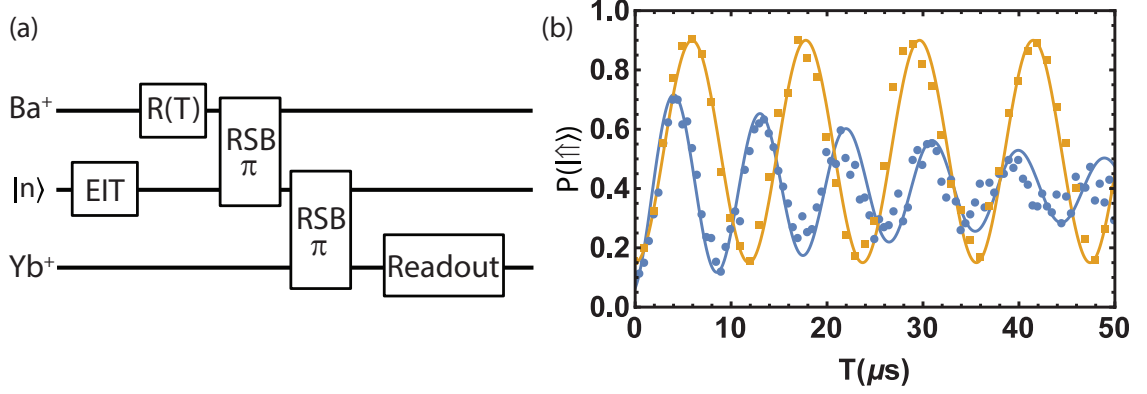


Figure 5.1: (a) Experimental sequence. (b) The Rabi flop on  $^{138}Ba^+$  is readout on  $^{171}Yb^+$  after state mapping. Yellow squares and blue circles show measurements from two different ion traps with average quanta of  $\bar{n} \approx 0.1$  and  $\bar{n} \approx 0.5$  after EIT cooling, respectively. Poor cooling behavior in the trap with the higher phonon occupation number is attributed to the observed excessive heating rate of  $\dot{\bar{n}} \approx 5 \text{ ms}^{-1}$ .

Raman transition using 532 nm laser beams with duration  $T$ :

$$|\psi\rangle_{Ba^+} = R(T, \phi_0)|\downarrow\rangle = \cos\left(\frac{\Omega T}{2}\right)|\downarrow\rangle + e^{i\phi_0}\sin\left(\frac{\Omega T}{2}\right)|\uparrow\rangle \quad (5.6)$$

where  $\Omega$  is the usual two photon Rabi frequency and  $\phi_0$  is the optical phase. Hence, this simply corresponds to the general picture with:

$$\cos\left(\frac{\Omega T}{2}\right) \rightarrow \alpha, \quad \left(\frac{\Omega T}{2}\right) \rightarrow \beta. \quad (5.7)$$

Afterwards,  $RSB \pi$  pulses transfer the state from  $^{138}Ba^+$  to  $^{171}Yb^+$  where it gets read out as shown in Fig. 5.1. Since the phase of the final state has no effect on  $\alpha$  and  $\beta$  coefficients, this measurement does not reveal coherence properties of this transfer operation. The final temperature has a significant effect in qubit state transfer fidelity, which is a big limitation of the CZ technique as demonstrated.

A separate experiment is conducted to verify that the phase written on the original qubit is preserved after the transfer operation onto the destination qubit (see

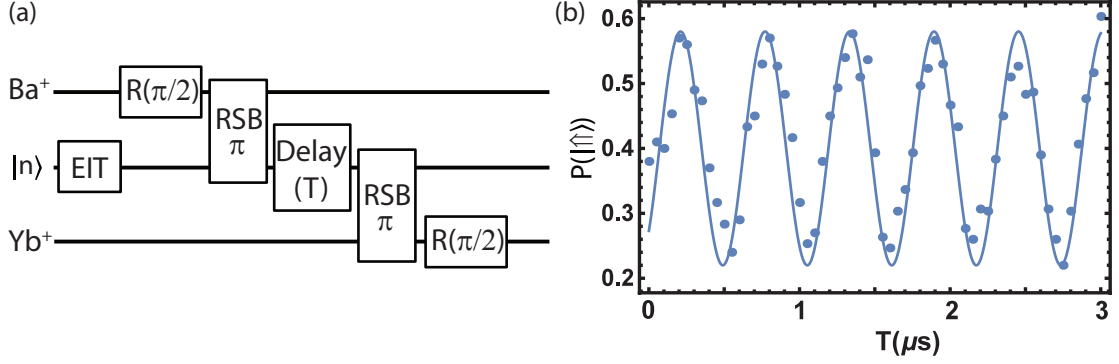


Figure 5.2: (a) Sequence of the Ramsey experiment. (b) A delay is imposed while the information is held on the phonon bus. Therefore, Ramsey fringes oscillate with frequency of the utilized mode, and measurement is in good agreement with  $\omega_m/2\pi \approx 1.8$  MHz of OP mode used here.

Fig. 5.2). Instead of continuously Rabi flopping the  $^{138}\text{Ba}^+$  qubit, phase evolution  $\omega_m T$  is probed with fixed  $\pi/2$  pulses in a Ramsey experiment. Applying a  $\pi/2$  transition with phase  $\phi_F$  to  $^{171}\text{Yb}^+$  in Eqn. 5.5 and replacing  $\alpha = \beta = \frac{1}{\sqrt{2}}$  for the initial rotation on  $^{138}\text{Ba}^+$ , the final state is:

$$\begin{aligned}
 |\Psi_F\rangle &= \frac{1}{2}|\downarrow\rangle|0\rangle(|\downarrow\rangle + e^{i\phi_F}|\uparrow\rangle) - e^{i(\phi_0 - \phi_{532} + \phi_T + \phi_{355})}(|\uparrow\rangle - e^{-i\phi_F}|\downarrow\rangle) \\
 &= \frac{1}{2}|\downarrow\rangle|0\rangle[(1 + e^{i\Phi})|\downarrow\rangle + e^{i\phi_F}(1 - e^{i\Phi})|\uparrow\rangle] \quad (5.8)
 \end{aligned}$$

where  $\Phi = \phi_0 - \phi_{532} + \phi_T + \phi_{355} - \phi_F$ . Since carrier  $\pi/2$  and sideband  $\pi$  pulses are driven by the same source for individual species, the differential phase between them,  $\phi_0 - \phi_{532}$  and  $\phi_{355} - \phi_F$ , is independent of optical phases. These differential phases can be adjusted by changing the phase of the RF applied to the Raman beam AOMs, however, they are kept constant for each experimental shot on this case. Hence, the amplitude of the state  $|\uparrow\rangle$  is expected to change with delay time  $T$  due to the  $\phi_T = \omega_m T$  dependence in  $\frac{1}{4}|(1 - e^{i\Phi})|^2$ .

These experiments demonstrate that a superposition on the communication qubit can be coherently transferred to the memory qubits with a CZ approach. However, there are two major challenges in using this scheme on a multi-species node of a network. First, the requirement for ground state cooled atoms would require extra time be spent on sub-Doppler cooling procedures to handle heating mechanisms, and to reduce the entanglement generation rate between modules as a consequence. As an alternative, refrigerant atoms in the ion crystal can be utilized for sympathetic cooling of communication qubits, although this might prevent processing quantum information on memory qubits during the cooling cycle and similarly introduce excessive down time on the network. Second, since the phase introduced by the photonic entanglement ( $\phi_0$ ) is a static phase [13], the transfer operation described above might not preserve this phase information if the optical phases are introduced by  $\phi_0 - \phi_{532}$ . Stabilization of optical paths on the wavelength scale or additional qubit rotations to cancel optical phases might be a solution to this problem.

## 5.2 Mølmer-Sørensen Interactions

The MS interaction provides a robust alternative to CZ type state transfer operations between communication and memory qubits. First, the atoms only need to be in the Lamb-Dicke limit rather than the motional ground state [78]. This would allow higher entanglement attempt rates since interruption for extra cooling steps gets minimized. Second, phase information can be preserved with MS interactions

on the state transfer operation [67].

The MS interaction is gated by simultaneous excitation of red and blue sideband transitions with a detuning of  $-\delta$  and  $\delta$ , respectively, from a selected motional mode [37, 78]. From Eqns. 3.17 and 3.16, this results in:

$$H_{\text{MS}} = \frac{\hbar}{2} \sum_{m=1,2} \Omega'_m \sigma_+^{(m)} (ae^{-i(\delta t - \phi_{m,r})} + a^\dagger e^{i(\delta t + \phi_{m,b})}) + \text{h.c.} \quad (5.9)$$

where  $\Omega'_m = \eta_m \Omega_m \mathcal{D}'_{n,n'}$  is the sideband Rabi frequency and phases of the red (r) and blue (b) transitions are  $\phi_{m,r(b)} = \Delta k_{m,r(b)} x_{m,0} - \Delta \phi_{r,(b)}$  with equilibrium position of the ions given by  $x_{m,0}$ . The Lamb-Dicke parameter  $\eta$  is dependent on the wavevector differences of two Raman beams and mode amplitude of the ion on the addressed motion, which is plugged using Eqn. 3.13 modified for unequal ion masses:

$$\eta_m = \Delta k_m q_m = \Delta k_m x_m \sqrt{\frac{\hbar}{2M_m \omega}} \quad (5.10)$$

where longitudinal motion is considered in this case and the mode frequency is  $\omega$ . The mode amplitudes  $x_m$  are found analytically and  $\Omega'_m$  measurements verified these findings in the previous chapter.

### 5.2.1 Spin-Dependent Forces

Before analyzing how two qubits can be entangled with this interaction, we first look at the single ion case where Eqn. 5.9 simplifies to:

$$H_{\text{MS}} = \frac{\hbar \Omega'}{2} (\sigma_+ e^{i\phi_S} - \sigma_- e^{-i\phi_S}) (ae^{i\phi_M} e^{-i\delta t} + a^\dagger e^{-i\phi_M} e^{i\delta t}) \quad (5.11)$$

where  $\phi_S = (\phi_r + \phi_b)/2$  is the spin phase and  $\phi_M = (\phi_r - \phi_b)/2$  is the motion phase.

The time evolution operator corresponding to this Hamiltonian can be found by Magnus expansion:

$$U(t) = \exp\left(\sum_i \hat{O}_i\right) \quad (5.12)$$

and the expansion terms are:

$$\hat{O}_1(t) = -\frac{i}{\hbar} \int_0^t H(t') dt' \quad (5.13)$$

$$\hat{O}_2(t) = -\frac{1}{2\hbar^2} \int_0^t dt' \int_0^{t'} [H(t'), H(t'')] dt'' \quad (5.14)$$

Even though there are an infinite number of terms in this expansion, the series terminates after the second term as will be shown here later. The first term of the Magnus expansion with spin operator defined as  $\hat{S} = (\sigma_+ e^{i\phi_S} - \sigma_- e^{-i\phi_S})$ :

$$\hat{O}_1(t) = \frac{\hbar\Omega'}{2} \hat{S} \int_0^t (ae^{i\phi_M} e^{-i\delta t} + a^\dagger e^{-i\phi_M} e^{i\delta t}) \quad (5.15)$$

$$= \hat{S}(\alpha(t)a^\dagger - \alpha^*(t)a) \quad (5.16)$$

where

$$\alpha(t) = \frac{\Omega'}{2\delta} [1 - e^{i\delta t}] e^{-i\phi_M} \quad (5.17)$$

The second term is:

$$\hat{O}_2(t) = -\frac{1}{2} \left(\frac{\Omega' \hat{S}}{2}\right)^2 \int_0^t dt' \int_0^{t'} (e^{-i\delta(t'-t'')} - e^{i\delta(t'-t'')}) dt'' \quad (5.18)$$

$$= i \left(\frac{\Omega' \hat{S}}{2\delta}\right)^2 (\delta t - \sin(\delta t)) \quad (5.19)$$

The third and higher order Magnus expansion terms contain nested commutators of the form  $[H(t), [H(t'), H(t'')]]$ . Since harmonic oscillator raising and lowering operators have a scalar commutator, the series terminates at second order. Therefore,

time evolution operator is:

$$U_{\text{MS}}(t) = \exp[\hat{S}(\alpha(t)a^\dagger - \alpha^*(t)a) + i\hat{S}^2\Phi(t)] \quad (5.20)$$

$$\Phi(t) = -\left(\frac{\Omega'}{2\delta}\right)^2 (\delta t - \sin(\delta t)) \quad (5.21)$$

This interaction applies a spin-dependent force on the atomic ion which can be seen easier on the eigenbasis of the spin operator. Considering the general case of qubit spin states  $|0\rangle$  and  $|1\rangle$ , the spin operator  $\hat{S}$  has eigenstates:

$$|0_{\phi_S}\rangle = \frac{1}{\sqrt{2}}(|0\rangle + e^{i\phi_S}|1\rangle) \quad (5.22)$$

$$|1_{\phi_S}\rangle = \frac{1}{\sqrt{2}}(|0\rangle - e^{i\phi_S}|1\rangle) \quad (5.23)$$

with eigenvalues  $\pm 1$ . In this basis, the time evolution operator is:

$$\begin{aligned} U_{\text{MS}}(t) &= \exp[(\alpha(t)a^\dagger - \alpha^*(t)a)(|1_{\phi_S}\rangle\langle 1_{\phi_S}| - |0_{\phi_S}\rangle\langle 0_{\phi_S}|) \\ &+ i\Phi(t)(|1_{\phi_S}\rangle\langle 1_{\phi_S}| + |0_{\phi_S}\rangle\langle 0_{\phi_S}|)]. \end{aligned} \quad (5.24)$$

The effect of this operator on atomic state  $|0, \beta\rangle$  including both spin and motion is:

$$\begin{aligned} U_{\text{MS}}(t)|0, \beta\rangle &= U_{\text{MS}}(t)(|0_{\phi_S}\rangle + |1_{\phi_S}\rangle)/\sqrt{2} \\ &= \frac{e^{i\Phi(t)}}{\sqrt{2}}[\hat{D}(\alpha(t))|1_{\phi_S}, \beta\rangle - \hat{D}(-\alpha(t))|0_{\phi_S}, \beta\rangle] \end{aligned} \quad (5.25)$$

with displacement operator defined as  $\hat{D}(\alpha(t)) = \exp[\alpha(t)a^\dagger - \alpha^*(t)a]$ . The displacement operator follows the  $\hat{D}(\alpha)\hat{D}(\beta) = \hat{D}(\alpha + \beta)e^{i\phi_D}$  commutation rule with  $\phi_D = \text{Im}(\alpha\beta^*)$  [73]. Therefore, the final state following the spin dependent force of MS interaction is:

$$U_{\text{MS}}(t)|0, \beta\rangle = \frac{e^{i\Phi(t)}}{\sqrt{2}}[e^{i\phi_D}|1_{\phi_S}, \beta + \alpha(t)\rangle - e^{-i\phi_D}|0_{\phi_S}, \beta - \alpha(t)\rangle]. \quad (5.26)$$

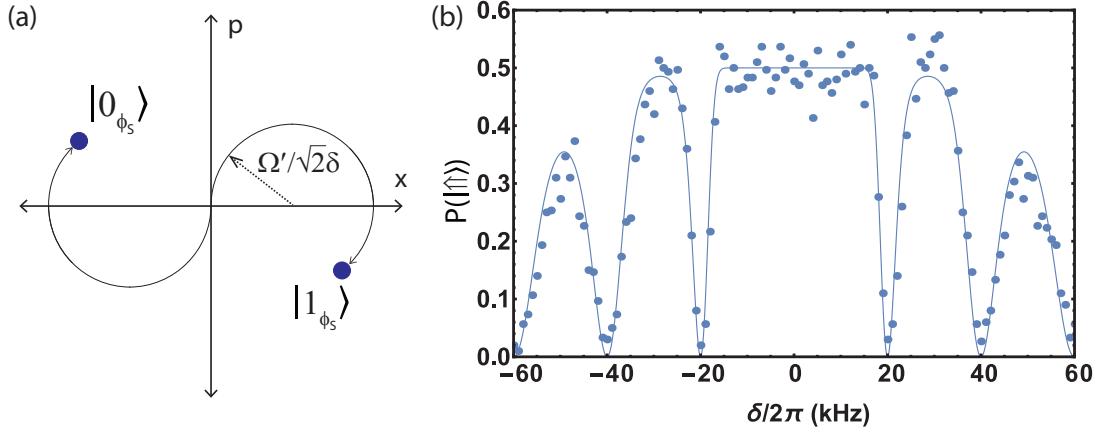


Figure 5.3: (a) The motional state is displaced in the phase space by driving red and blue sideband transitions with a detuning  $\delta$ . The applied force is opposite for different spin states, hence they get separated with this interaction. The trajectory, shown in a frame rotating with the harmonic oscillator frequency, is a circle with radius  $\Omega'/\sqrt{2\delta}$  that closes after  $T = 2n\pi/\delta$ , where  $n$  is an integer indicating the number of loops in the phase space. (b) Bi-chromatic fields are applied using the 355 nm field to realize MS interaction on a single  $^{171}\text{Yb}^+$  qubit initialized in  $|\downarrow\rangle$ . The detuning,  $\delta$ , from the red and blue sideband transition is scanned for a fixed interaction duration of  $50 \mu\text{s}$ . The spin and motion decouple when  $\delta/2\pi = n \times 20$  kHz and the  $^{171}\text{Yb}^+$  spin state goes back to  $|\downarrow\rangle$ .

The interaction can be visualized in the phase space (see Fig. 5.3(a)) where there is no coupling between eigenstates of the spin operator, but motional states are displaced and get entangled with the spin states. After an interaction time of  $T = 2n\pi/\delta$ , with an integer  $n$ , the motional states overlap again at the starting point in phase space (since  $\alpha(T) = 0$  from Eqn. 5.17) and disentangle from the spin. From Eqn, 5.21 the overall effect is an extra phase picked up by the spin states:

$$\Phi(T) = n\pi \left( \frac{\Omega'}{\sqrt{2\delta}} \right)^2 \quad (5.27)$$

which corresponds to a circular trajectory traced  $n$  times in the phase space.

This analysis is tested by measuring the  $^{171}\text{Yb}^+$  qubit state after applying a spin-dependent force to the  $|\downarrow\rangle$  state. This force is created by bi-chromatic 355 nm

fields and the expected spin rotation probability for a thermal distribution is given by [37]:

$$P(|\uparrow\rangle)[t, \delta] = \frac{1}{2}(1 - e^{-(\bar{n}+1/2)|2\alpha(t,\delta)|^2}) \quad (5.28)$$

where  $\bar{n}$  is the average phonon occupation number. This theoretical curve is compared to experimental measurements in Fig. 5.3(b). This experiment was conducted on a  $^{171}\text{Yb}^+ - ^{138}\text{Ba}^+$  crystal, however the force is only applied to the  $^{171}\text{Yb}^+$  qubit using the collective in-phase mode with  $\omega_{\text{IP}} \approx 1$  MHz. Hence, the  $^{138}\text{Ba}^+$  atom is not involved in the dynamics and can be traced out from the joint state.

## 5.2.2 Multi-Species Entanglement

The same treatment can be extended for two atoms, specifically the  $^{171}\text{Yb}^+ - ^{138}\text{Ba}^+$  crystal considered here. The Hamiltonian given in Eqn. 5.9 simplifies to [73]:

$$H = \sum_{m_1=|\downarrow\rangle_{\phi_{S,1}}, |\uparrow\rangle_{\phi_{S,1}}} \sum_{m_2=|\downarrow\rangle_{\phi_{S,2}}, |\uparrow\rangle_{\phi_{S,2}}} \hbar \left( \frac{\Omega_{m_1, m_2}^*}{2} a e^{i\delta t} + \frac{\Omega_{m_1, m_2}}{2} a^\dagger e^{-i\delta t} \right) |m_1 m_2\rangle \langle m_1 m_2| \quad (5.29)$$

where  $\Omega_{m_1, m_2} = \pm \Omega_1' e^{-i\phi_{M,1}} \pm \Omega_2' e^{-i\phi_{M,2}}$  with positive (negative) signs corresponding to  $m = |\uparrow\rangle_{\phi_{S,1}}, |\uparrow\rangle_{\phi_{S,2}}$  ( $m = |\downarrow\rangle_{\phi_{S,1}}, |\downarrow\rangle_{\phi_{S,2}}$ ). Here, the spins are expressed in rotated  $\phi_S$  basis with eigenvectors of operator  $\hat{S}_i = (\sigma_+ e^{i\phi_{S,i}} - \sigma_- e^{-i\phi_{S,i}})$ . The spin and motional force phases are:

$$\phi_{S,i} = (\Delta k_{i,r} X_{0,i} - \Delta \phi_{i,r} + \Delta k_{i,b} X_{0,i} - \Delta \phi_{i,b})/2 \quad (5.30)$$

$$\phi_{M,i} = (\Delta k_{i,r} X_{0,i} - \Delta \phi_{i,r} - \Delta k_{i,b} X_{0,i} + \Delta \phi_{i,b})/2 \quad (5.31)$$

where  $X_{0,i}$  is the equilibrium position.

The time evolution under this Hamiltonian is a displacement in phase space similar to the single qubit case which is utilized for entangling two qubit internal states via spin-dependent geometrical phase accumulations. After an interaction time of  $T = 2\pi/\delta$  with  $\Omega'_1 = \Omega'_2 = \Omega$ , the loops close in phase space and phases acquired for the joint two qubit states are [67]:

$$\Phi_e = \Phi_{|\downarrow\rangle_{\phi_{S,1}}|\downarrow\rangle_{\phi_{S,2}},|\uparrow\rangle_{\phi_{S,1}}|\uparrow\rangle_{\phi_{S,2}}} = \frac{8\pi\Omega^2}{\delta^2} \sin^2\left(\frac{\phi_{M,1} - \phi_{M,2}}{2}\right) \quad (5.32)$$

$$\Phi_o = \Phi_{|\downarrow\rangle_{\phi_{S,1}}|\uparrow\rangle_{\phi_{S,2}},|\uparrow\rangle_{\phi_{S,1}}|\downarrow\rangle_{\phi_{S,2}}} = \frac{8\pi\Omega^2}{\delta^2} \cos^2\left(\frac{\phi_{M,1} - \phi_{M,2}}{2}\right) \quad (5.33)$$

where  $\Phi_e$  and  $\Phi_o$  represent the phase accumulated by even and odd spin parity states, respectively. The entangling speed is maximum, for fixed sideband Rabi frequencies, when the phase difference between geometric phases are maximized, which happens at  $\phi_{M,1} - \phi_{M,2} = p\pi$  with an integer  $p$ . This can be visualized in the phase space by considering the displacement of individual motional packets corresponding to internal spin states, which can add up or cancel depending on the displacement direction (see Fig. 5.4). Therefore, application of the MS interaction for  $T = 2\pi/\delta$  to qubits initialized to  $|\downarrow\rangle|\downarrow\rangle$  results in:

$$\begin{aligned} U(T)|\downarrow\rangle|\downarrow\rangle &= U(T) \frac{|\downarrow\rangle_{\phi_{S,1}}|\downarrow\rangle_{\phi_{S,2}} + |\uparrow\rangle_{\phi_{S,1}}|\uparrow\rangle_{\phi_{S,2}} - |\downarrow\rangle_{\phi_{S,1}}|\uparrow\rangle_{\phi_{S,2}} - |\uparrow\rangle_{\phi_{S,1}}|\downarrow\rangle_{\phi_{S,2}}}{2} \\ &= e^{i\Phi_o} \frac{e^{i(\Phi_e - \Phi_o)} (|\downarrow\rangle_{\phi_{S,1}}|\downarrow\rangle_{\phi_{S,2}} + |\uparrow\rangle_{\phi_{S,1}}|\uparrow\rangle_{\phi_{S,2}}) - |\downarrow\rangle_{\phi_{S,1}}|\uparrow\rangle_{\phi_{S,2}} - |\uparrow\rangle_{\phi_{S,1}}|\downarrow\rangle_{\phi_{S,2}}}{2}. \end{aligned} \quad (5.34)$$

The maximally entangled state is created when  $\Phi_e - \Phi_o = \pi/2$ , which is realized by changing the optical intensity of the Raman beams to adjust the sideband Rabi

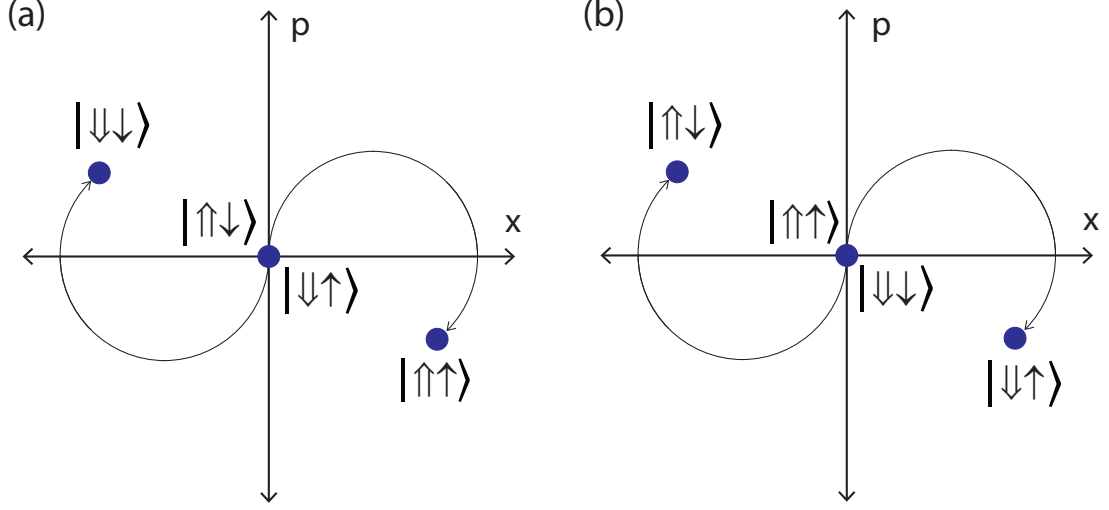


Figure 5.4: Addressing the out-of-phase mode of the  $^{171}\text{Yb}^+ - ^{138}\text{Ba}^+$  crystal where the spin states are expressed in their corresponding  $\phi_S$  basis, (a) [(b)] shows the evolution of motional states under influence of a differential force. This is realized by setting  $\phi_{M,1} = (2p + 1)\pi + \phi_{M,2}$  [ $\phi_{M,1} = 2p\pi + \phi_{M,2}$ ] where  $p$  is an integer. In this case, the force is out-of-phase when the qubit internal states are in an even [odd] parity state, therefore the mode is excited for only two out of four joint states. Either setting can be used for generating a maximally entangled two qubit state since a phase difference between pairs is evident in both cases.

frequencies:

$$U(T)|\downarrow\rangle|\downarrow\rangle = \frac{1}{\sqrt{2}}(|\downarrow\rangle|\downarrow\rangle - ie^{i(\phi_{S,1} + \phi_{S,2})}|\uparrow\rangle|\uparrow\rangle) \quad (5.35)$$

where only the spin phase remains on the entangled state while the motion phase mainly determines the required optical intensities.

### 5.2.2.1 Experimental Considerations and Results

There are several calibration steps for ideal experimental implementation of the MS interaction where spin-dependent forces are applied using 355 and 532 nm Raman beams from a pulsed laser. The out-of-phase longitudinal mode is used here

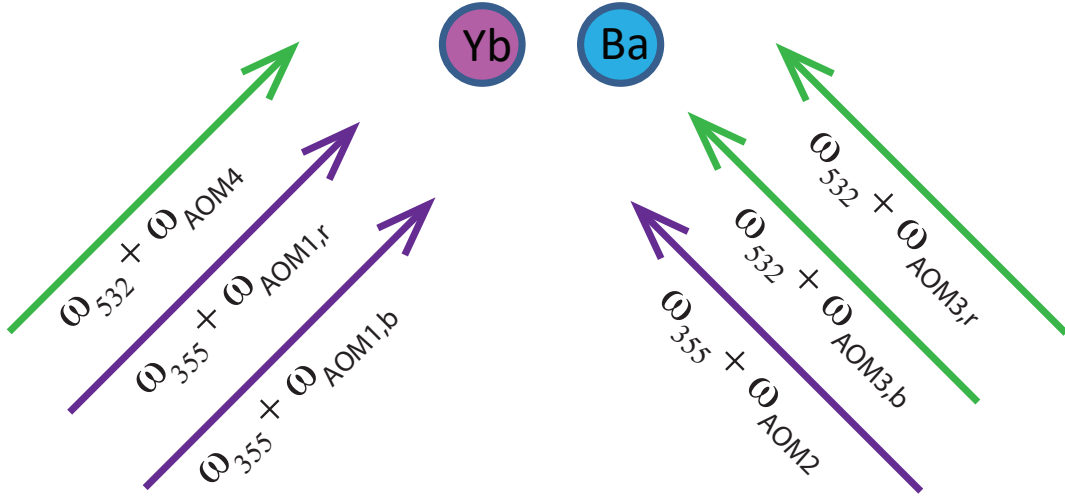


Figure 5.5: The red and blue sideband transitions are addressed by a bi-chromatic setup where AOMs are used for frequency adjustments on the main Raman beams. These beams have a  $\Delta k$  component along the longitudinal axis to address the collective motion in this direction. The RFs used on AOM's 1 and 3 are produced with the same arbitrary waveform generator which is essential in maintaining a well defined phase relation between  $\phi_{M,1}$  and  $\phi_{M,2}$  as well as between single and two qubit operations which involves  $\phi_{S,1}$  and  $\phi_{S,2}$ . The effects of laser repetition rate fluctuations on the beat-note frequency is canceled with feeding forward the corrections to the AOM 2 [98] and a free running RF is applied to AOM 4.

with a frequency of  $\omega_{OP} \approx 1.8$  MHz to benefit from lower heating rates and a higher mode frequency compared to in-phase mode. The fields are incident on the atoms with a  $\pi/4$  angle to the motional axis as shown in Fig. 5.5, resulting in  $|\Delta \mathbf{k}| \approx \sqrt{2}k$ .

The off-resonant red and blue sideband transitions are driven by creating bi-chromatic optical fields by modulating an AOM with two RF's in conjunction with

another beam (see Fig. 5.5 and 5.6):

$$\omega_{\text{AOM1,r}} - \omega_{\text{AOM2}} = \omega_{\text{HF}} - c\omega_{\text{rep}} - \omega_{\text{OP}} - \delta \quad (5.36)$$

$$\omega_{\text{AOM1,b}} - \omega_{\text{AOM2}} = \omega_{\text{HF}} - c\omega_{\text{rep}} + \omega_{\text{OP}} + \delta \quad (5.37)$$

$$\omega_{\text{AOM3,r}} - \omega_{\text{AOM4}} = \omega_{\text{Zeeman}} - \omega_{\text{OP}} - \delta \quad (5.38)$$

$$\omega_{\text{AOM3,b}} - \omega_{\text{AOM4}} = \omega_{\text{Zeeman}} + \omega_{\text{OP}} + \delta \quad (5.39)$$

where  $\omega_{\text{rep}}/2\pi$  is the repetition rate of the pulsed laser and  $c$  is an integer. Since the Zeeman splitting of the  $^{138}\text{Ba}^+$  qubit is only a few MHz, the large bandwidth of pulsed laser is not necessary to be utilized with 532 nm Raman beams.

For the multi-species entanglement generation, first the red and blue sideband Rabi frequencies on each individual qubit need to be equalized. Due to diffraction efficiency variance for different RF inputs and beam steering effects, the Rabi frequencies might not be equal with the same RF power input. This calibration can be done by measuring the sideband Rabi frequencies directly, and the single qubit MS interaction can be used to verify and fine tune the optical intensities by observing closure of the trajectories in phase space.

As analyzed in the previous section, the free parameters are  $\delta$ ,  $\phi_S$ ,  $\phi_M$  and  $\Omega$  for each qubit. The duration of the entangling gate is constrained by chosen detuning as  $T = 2n\pi/\delta$  where  $n$  is an integer number indicating circle laps in the phase space. The optical intensities need to be adjusted to realize  $\Omega'_1 = \Omega'_2 = \Omega$  and

$$n \times \frac{8\pi\Omega^2}{\delta^2} = \frac{\pi}{2}. \quad (5.40)$$

Decoherence mechanisms, such as heating of the motional modes or magnetic field noise, introduce errors during interaction, therefore it is beneficial to have faster

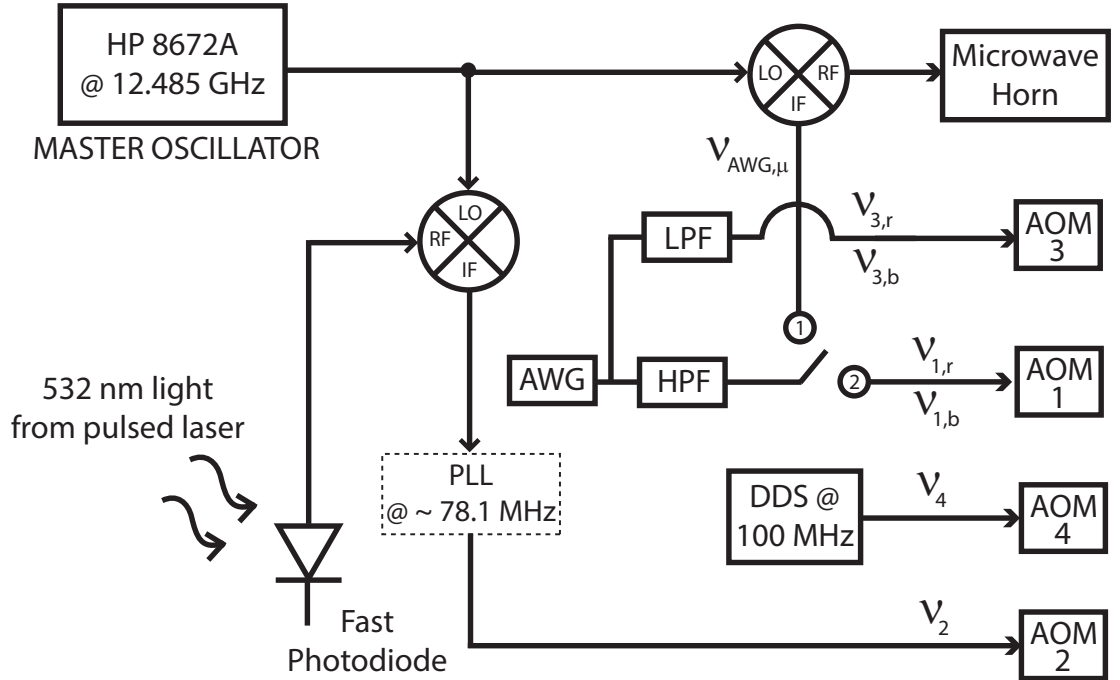


Figure 5.6: Schematic of RF circuitry used for driving coherent operations on  $^{171}\text{Yb}^+ - ^{138}\text{Ba}^+$  system. The output of an arbitrary waveform generator (AWG) can be switched between microwave or stimulated Raman transitions. The waveform written to the AWG for MS interactions includes all four RF signals ( $\nu_{1,r}$ ,  $\nu_{1,b}$ ,  $\nu_{2,r}$ ,  $\nu_{2,b}$  with  $\nu = \omega/2\pi$ ) and low/high pass filters (LPF, HPF) prevent output RFs from going to the AOMs for other qubit. A phase-lock-loop (PLL) is used to lock the beat-note frequency addressing  $^{171}\text{Yb}^+$  rotations [98].

entanglement operations. While a larger detuning can be used for this purpose, it also introduces a requirement for larger Rabi frequencies as well from Eqn. 5.40. In practice, the achievable entanglement speed is limited by available optical power on the Raman beams.

After setting a detuning  $\delta$  and fixing the interaction time correspondingly, and equalizing the sideband Rabi frequencies between  $^{171}\text{Yb}^+$  and  $^{138}\text{Ba}^+$ , the motional phase  $\phi_M$  on one of the qubits is adjusted by changing the RF phase addressing either the red or blue sideband transition. This way, maximum differential phase accumulation between even and odd parity joint states can be realized (see Eqn. 5.33). One crucial aspect is maintaining the shot-to-shot phase relation between these motional phases such that  $\phi_{M,1} - \phi_{M,2}$  is constant throughout experiments. With the  $\Delta k_{i,r} - \Delta k_{i,b}$  term in Eqn. 5.31, these phases are insensitive to changes in optical path length fluctuations and therefore once set, they remain stable [33] and usage of a single arbitrary waveform generator makes sure they have a well defined phase relation between each other in every experiment.

In contrast, the spin phases  $\phi_S$  are dependent on the optical path lengths and they are written directly to the entangled state as in Eqn. 5.35. However, if the spin rotations are driven with the same Raman beams, the phase coherence can be maintained between single and two qubit operations. In a multi-species network, photonic entanglement operations introduce extra complexity to the system since the multi-species MS interaction is aimed to be used for transferring information from communication to memory qubits, and an optical dependence might result in decoherence between the photonic entanglement and information transfer oper-

ations. The method demonstrated in Ref. [33] to resolve this issue is not directly compatible with a multi-species setup since canceling  $\phi_S$  optical sensitivity transfers this effect to  $\phi_M$  which would result in variance of phase space trajectories and the accumulated geometric phase. Instead, extra single qubit rotations can be included to cancel any optical path dependence of spin phases [67, 73] but as will be shown later, this condition can also be realized without resorting to them.

It should be noted that, since the 355 and 532 nm pulses do not follow the same path, they do not apply the spin dependent force simultaneously to the qubits. This might seem counterintuitive, but in the phase space picture it can be visualized in terms of consecutive displacement on the motional state corresponding to spin states which add or cancel depending on the motional phase of the Raman beams and the parity of joint spin state.

Following these steps, the  $^{171}\text{Yb}^+$  and  $^{138}\text{Ba}^+$  qubits are entangled and the results are shown in Fig. 5.7. The fidelity of this operation was  $\sim \mathcal{F} = 0.60$  in our system, and we attribute this low fidelity to an excessive heating rate ( $\dot{\bar{n}} \approx 5 \text{ ms}^{-1}$ ) in the trap where this operation was implemented [84]. Another multi-species trap is assembled since these results were obtained, and a higher fidelity operation is expected with a lower heating rate of  $\dot{\bar{n}} \approx 0.1 \text{ ms}^{-1}$ .

### 5.3 The Swap Gate

The entanglement generated via the MS interaction is not sufficient for transferring information from  $^{138}\text{Ba}^+$  to  $^{171}\text{Yb}^+$  by itself. However, a swap gate can be

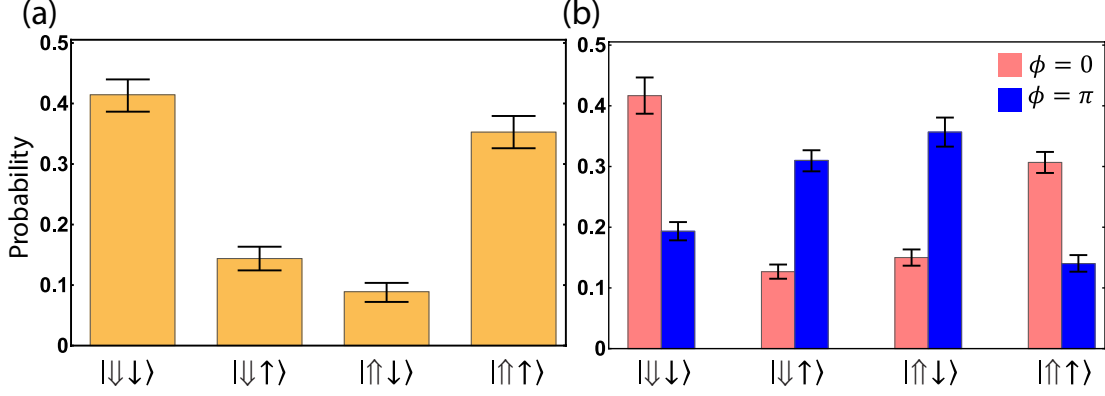


Figure 5.7: (a) Populations of  $^{171}\text{Yb}^+$  and  $^{138}\text{Ba}^+$  qubit states after MS interaction. (b) Following the MS interaction,  $\pi/2$  pulses are applied to both qubits. The phase of  $^{138}\text{Ba}^+$   $\pi/2$  pulse is kept constant, while the  $^{171}\text{Yb}^+$   $\pi/2$  rotation phase is scanned. Maximum contrast points achieved in the resulting parity oscillation of the qubits are shown here.

implemented by a sequence of two MS gates.

The full truth table of MS entangling gate is given by:

$$\begin{aligned}
|\downarrow\rangle|\downarrow\rangle &\rightarrow \frac{1}{\sqrt{2}}(|\downarrow\rangle|\downarrow\rangle - ie^{i(\phi_{S,1}+\phi_{S,2})}|\uparrow\rangle|\uparrow\rangle) \\
|\downarrow\rangle|\uparrow\rangle &\rightarrow \frac{1}{\sqrt{2}}(|\downarrow\rangle|\uparrow\rangle - i|\uparrow\rangle|\downarrow\rangle) \\
|\uparrow\rangle|\downarrow\rangle &\rightarrow \frac{1}{\sqrt{2}}(|\uparrow\rangle|\downarrow\rangle - i|\downarrow\rangle|\uparrow\rangle) \\
|\uparrow\rangle|\uparrow\rangle &\rightarrow \frac{1}{\sqrt{2}}(|\uparrow\rangle|\uparrow\rangle - ie^{-i(\phi_{S,1}+\phi_{S,2})}|\downarrow\rangle|\downarrow\rangle). \tag{5.41}
\end{aligned}$$

In a multi-species apparatus, the aim is transferring a superposition state in  $^{138}\text{Ba}^+$ ,  $\alpha|\downarrow\rangle + e^{i\phi}|\uparrow\rangle$ , to the memory qubit. Applying two MS gates to the joint state, with a  $\pi$  phase shift on the total spin phase in the second operation with respect to the first, results in transfer of  $^{138}\text{Ba}^+$  superposition to  $^{171}\text{Yb}^+$  :

$$U_{\text{MS}}(\phi_{S,1} - \pi, \phi_{S,2})U_{\text{MS}}(\phi_{S,1}, \phi_{S,2})[|\downarrow\rangle(\alpha|\downarrow\rangle + \beta e^{i\phi}|\uparrow\rangle)] \rightarrow |\downarrow\rangle(\alpha|\downarrow\rangle - i\beta e^{i\phi}|\uparrow\rangle). \tag{5.42}$$

The required  $\pi$  spin phase shift can be realized by advancing the red and blue sideband RF phases by  $\pi$  for the second MS operation,  $\Delta\phi_{1,r} \rightarrow \Delta\phi_{1,r} + \pi$  and  $\Delta\phi_{1,b} \rightarrow \Delta\phi_{1,b} + \pi$ , which results in:

$$\phi_{S,1} \rightarrow \phi_{S,1} + \pi \quad (5.43)$$

$$\phi_{M,1} \rightarrow \phi_{M,1} \quad (5.44)$$

from Eqn. 5.30 and 5.31. This also preserves the motional phase, which results in identical phase trajectories for both MS gates and produce the same truth table. Importantly, the spin phases are not imprinted on the final state via this swap gate. Hence, the phase information of  $^{138}\text{Ba}^+$  in addition to superposition amplitudes  $\alpha$  and  $\beta$  can be transferred to  $^{171}\text{Yb}^+$  without introducing decoherence.

To sum up, the MS approach provides a robust and coherent transfer method compared to the CZ approach. However, with the low fidelity of the MS gate in our system, transferring information with this method has not been attempted yet.

## Chapter 6: Outlook

The basic ingredients of a multi-species node for realizing a network architecture are demonstrated in this thesis. The first step toward validating this approach of scaling would be combining these operations to show entanglement between a  $^{138}\text{Ba}^+$  photon and a  $^{171}\text{Yb}^+$  atomic qubit, and efforts are underway.

In this chapter, I describe how some of the additional key requirements can be implemented in a network structure. First, the communication  $^{138}\text{Ba}^+$  qubits of distant modules need to be entangled which can be done following the Bell state measurement methods demonstrated in Refs. [13,15,25]. However, atomic structure of a  $^{138}\text{Ba}^+$  atom is different from the atoms used in previous works, and requires extra considerations on the experimental sequence and the setup.

Second, coherence across the network needs to be maintained in this architecture. These considerations are outlined in detail in Ref. [33] and I provide small adjustments to this work to incorporate multi-species modules.

### 6.1 Entanglement of Remote Barium Qubits

The experimentally shown atom-photon entanglement in this thesis could be utilized to connect separate modules. However, mixing between two orthogonal

polarization states at high collection solid angles [36] would result in considerable error in this operation.

As an alternative, photons can be collected along the quantization axis, where coupling of a  $\pi$  polarized photon into a single mode fiber vanishes due to rotational symmetry [71]. However, this approach requires adjustments of the photon generation scheme and the optical beam setup.

The requirement for a circularly polarized beam for  $^{138}\text{Ba}^+$  qubit initialization poses a challenge in this new setup. This beam needs to be along the quantization axis for perfect polarization and therefore it propagates along the axis of collection and might damage the detectors that are used for the heralded entanglement scheme. Even though the initialization beam is not incident when detection of the single photons from  $^{138}\text{Ba}^+$  is attempted, intense optical beams on photon detectors might introduce afterpulse that require additional delays in the sequence to minimize overlap between this signal and the photons originating from the atom. Some possible configurations to address this issue are shown in Fig. 6.1.

After initializing the  $^{138}\text{Ba}^+$  qubits to state  $|\downarrow\rangle$ , a  $\pi/2$  rotation is applied to create a superposition state and with a subsequent fast excitation  $\pi$  pulse, the atom–photon state is:

$$|\downarrow\rangle \rightarrow |\downarrow\rangle + |\uparrow\rangle \rightarrow (|\downarrow\rangle|\pi\rangle + |\uparrow\rangle|\sigma^-\rangle) + (|\uparrow\rangle|\pi\rangle + |\downarrow\rangle|\sigma^+\rangle) \quad (6.1)$$

ignoring normalization. As mentioned before, the  $\pi$  polarization does not couple into the fiber along this direction, resulting in:

$$|\Psi\rangle = |\uparrow\rangle|\sigma^-\rangle + |\downarrow\rangle|\sigma^+\rangle \quad (6.2)$$

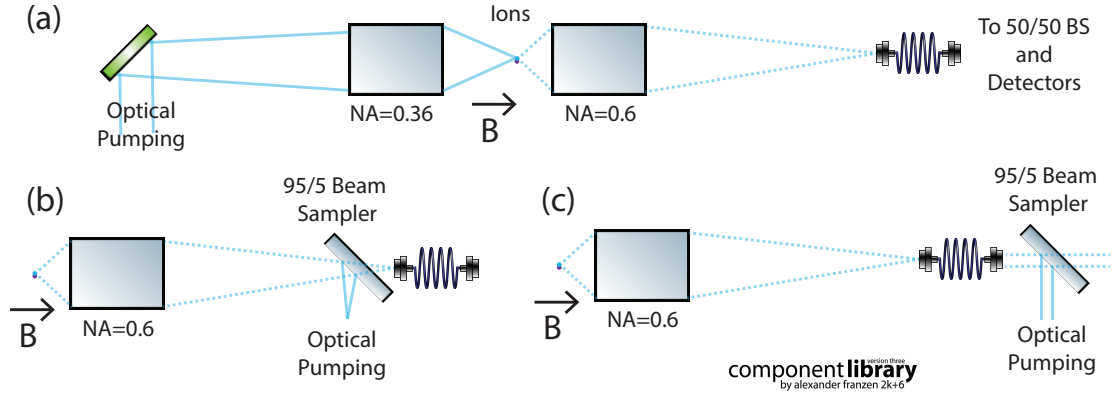


Figure 6.1: (a) The circular polarized optical pumping beam can be sent through the opposite side of the single photon collection optics, but this light would couple into the fiber and might have adverse effects on the single photon detectors. Additional recovery time for detectors might result in a lower entanglement generation rate with this configuration. (b) Instead, initialization light can be aligned from the same side of collection optics by using a beam sampler such that most of the light can be coupled into the fiber. Aberrations that might stem from the sampler can be corrected with adaptive optics [59] or the sampler can be moved further downstream as in part (c) if reflections that might go back to the detectors are not significant.

an atom–photon entangled state. A quarter wave plate rotates circular polarization into linear, which is easier to distinguish in lab frame:

$$|\Psi\rangle = |\uparrow\rangle|H\rangle + |\downarrow\rangle|V\rangle. \quad (6.3)$$

The polarization state of the photons from two different ion traps are measured after a 50/50 beam splitter where coincident detection of photons heralds the entanglement of atomic qubits.

Another isotope of barium is under development for quantum information purposes in the Campbell Group at UCLA. Ba-133 has nuclear spin 1/2 and consequently  $^{133}\text{Ba}^+$  atomic level structure resembles  $^{171}\text{Yb}^+$  closely. However, natural abundance of this isotope is too low for reliable trapping, hence enriched sources are required. More importantly, radioactivity of this isotope requires additional safety

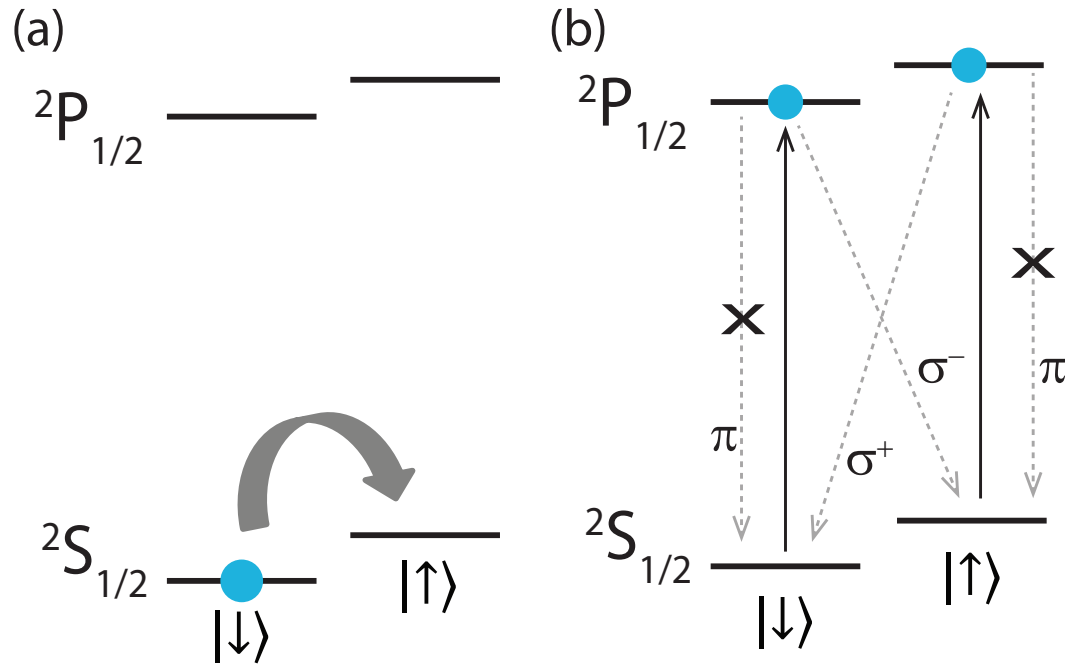


Figure 6.2: (a) After initialization in  $|\downarrow\rangle$ , a  $\pi/2$  rotation prepares the qubits for photon generation with fast excitation. (b) Spontaneous emission results in photons entangled with their parent atom, and collection along the quantization axis prevents  $\pi$  polarized components from coupling to the fiber. However, there is a trade-off between fidelity and entanglement generation rate with this approach since qubit rotations need to be incorporated into each trial.

procedures. Its decay type is electron capture with an average emitted gamma energy of 0.266 MeV and half life of 10.74 years.

Compared to  $^{138}\text{Ba}^+$ , faster entanglement generation, likely a factor of two, can be achieved with  $^{133}\text{Ba}^+$  since qubit preparation step can be eliminated with this isotope, similar to schemes demonstrated in Refs. [13,25]. Additionally, the frequency of the photons rather than the polarization state can be utilized in heralded entanglement schemes [15] to isolate environmental effects from flying photon qubits. Other advantages would be deterministic single shot qubit state measurements and longer coherence times, which are not strong requirements for communication qubits in a multi-species module as mentioned before.

## 6.2 Maintaining Phase Stability in a Multi-Species Network

The phase stability in a single species network architecture with quantum operations spread temporally and spatially is considered in great detail in Ref. [33]. All of the quantum gates are referenced to a common oscillator with sufficiently low phase noise in this method (see Fig. 6.3).

This approach can be easily extended to a multi-species module. Since the swap gate does not introduce additional phases and information from  $^{138}\text{Ba}^+$  to  $^{171}\text{Yb}^+$  can be transferred coherently, as long as operations involving the memory qubits preserve phase information, the system can be scaled up with a multi-species approach. There is also no limitation on which axis of motion needs to be used for the  $^{138}\text{Ba}^+ - ^{171}\text{Yb}^+$  swap gate. Longitudinal modes can be used for this operation



## Bibliography

- [1] C. Monroe, R. J. Schoelkopf, and M. D. Lukin. Quantum connections. *Sci. Am.*, 314:50–57, 2016.
- [2] T. Xia, M. Lichtman, K. Maller, A. W. Carr, M. J. Piotrowicz, L. Isenhower, and M. Saffman. Randomized benchmarking of single-qubit gates in a 2D array of neutral-atom qubits. *Phys. Rev. Lett.*, 114:100503, 2015.
- [3] T. Brecht, W. Pfaff, C. Wang, Y. Chu, L. Frunzio, M. H. Devoret, and R. J. Schoelkopf. Multilayer microwave integrated quantum circuits for scalable quantum computing. *NPJ Quant. Inf.*, 2:16002, 2016.
- [4] A. Reiserer, N. Kalb, M. S. Blok, K. J. M. van Bemmelen, T. H. Taminiiau, R. Hanson, D. J. Twitchen, and M. Markham. Robust quantum-network memory using decoherence-protected subspaces of nuclear spins. *Phys. Rev. X*, 6:021040, 2016.
- [5] S. Olmschenk, K. C. Younge, D. L. Moehring, D. N. Matsukevich, P. Maunz, and C. Monroe. Manipulation and detection of a trapped  $\text{Yb}^+$  hyperfine qubit. *Phys. Rev. A*, 76:052314, 2007.
- [6] C. J. Dedman, R. G. Dall, L. J. Byron, and A. G. Truscott. Active cancellation of stray magnetic fields in a Bose-Einstein condensation experiment. *Rev. Sci. Instrum.*, 78:024703, 2007.
- [7] A. Narla, S. Shankar, M. Hatridge, Z. Leghtas, K. M. Sliwa, E. Zalys-Geller, S. O. Mundhada, W. Pfaff, L. Frunzio, R. J. Schoelkopf, and M. H. Devoret. Robust concurrent remote entanglement between two superconducting qubits. *Phys. Rev. X*, 6:031036, Sep 2016.
- [8] A. Sipahigil, M. L. Goldman, E. Togan, Y. Chu, M. Markham, D. J. Twitchen, A. S. Zibrov, A. Kubanek, and M. D. Lukin. Quantum interference of single photons from remote nitrogen-vacancy centers in diamond. *Phys. Rev. Lett.*, 108:143601, Apr 2012.

- [9] T. Choi, S. Debnath, T. A. Manning, C. Figgatt, Z.-X. Gong, L.-M. Duan, and C. Monroe. Optimal quantum control of multimode couplings between trapped ion qubits for scalable entanglement. *Phys. Rev. Lett.*, 112:190502, May 2014.
- [10] C. Monroe and J. Kim. Scaling the ion trap quantum processor. *Science*, 339:1164–1169, 2013.
- [11] R. Islam et al. Emergence and frustration of magnetism with variable-range interactions in a quantum simulator. *Science*, 340:583, 2013.
- [12] C. Monroe, R. Raussendorf, A. Ruthven, K. R. Brown, P. Maunz, L.-M. Duan, and J. Kim. Large-scale modular quantum-computer architecture with atomic memory and photonic interconnects. *Phys. Rev. A*, 89:022317, 2014.
- [13] D. Hucul, I. V. Inlek, G. Vittorini, C. Crocker, S. Debnath, S. M. Clark, and C. Monroe. Modular entanglement of atomic qubits using both photons and phonons. *Nat. Phys.*, 11:37–42, 2015.
- [14] S. Debnath, N. M. Linke, C. Figgatt, K. A. Landsman, K. Wright, and C. Monroe. Demonstration of a small programmable quantum computer with atomic qubits. *Nature*, 536:63, 2016.
- [15] D. L. Moehring, P. Maunz, S. Olmschenk, K. C. Younge, D. N. Matsukevich, L.-M. Duan, and C. Monroe. Entanglement of single atom quantum bits at a distance. *Nature*, 449:68, 2007.
- [16] W. Pfaff, B. J. Hensen, G. Bernien, S. B. van Dam, M.S. Blok, T. H. Haminiau, M. J. Tiggelman, R. N. Schouten, M. Markham, D. J. Twitchen, and R. Hanson. Unconditional quantum teleportation between distant solid-state quantum bits. *Science*, 345:532–535, Aug 2014.
- [17] C. Nölleke, A. Neuzner, A. Reiserer, C. Hahn, G. Rempe, and S. Ritter. Efficient teleportation between remote single-atom quantum memories. *Phys. Rev. Lett.*, 110:140403, Apr 2013.
- [18] D. Kielpinski, C. Monroe, and D. J. Wineland. Architecture for a large-scale ion-trap quantum computer. *Nature*, 417:709, 2002.
- [19] C. K. Hong, Z. Y. Ou, and L. Mandel. Measurement of subpicosecond time intervals between two photons by interference. *Phys. Rev. Lett.*, 59:2044–2046, Nov 1987.
- [20] B. Calkins, P. L. Mennea, A. E. Lita, B. J. Metcalf, W. S. Kolthammer, A. L.-L., J. B. Spring, P. C. Humphreys, R. P. Mirin, J. C. Gates, P. G. R. Smith, I. A. Walmsley, T. Gerrits, and S. W. Nam. High quantum-efficiency photon-number-resolving detector for photonic on-chip information processing. *Opt. Express*, 21(19):22657–22670, Sep 2013.

- [21] T. Legero, T. Wilk, A. Kuhn, and G. Rempe. Time-resolved two-photon quantum interference. *Appl. Phys. B*, 77:797, 2003.
- [22] J. D. Jackson. Classical electrodynamics. *John Wiley and Sons, Inc., 3rd edition*, 1999.
- [23] B. B. Blinov, D. L. Moehring, L.-M. Duan, and C. Monroe. Observation of entanglement between a single trapped atom and a single photon. *Nature*, 428:153–157, 2004.
- [24] T-C. Wei, J. T. Barreiro, and P. G. Kwiat. Hyperentangled bell-state analysis. *Phys. Rev. A*, 75:060305, Jun 2007.
- [25] D. N. Matsukevich, P. Maunz, D. L. Moehring, S. Olmschenk, and C. Monroe. Bell inequality violation with two remote atomic qubits. *Phys. Rev. Lett.*, 100:150404, Apr 2008.
- [26] S. Olmschenk, D. Hayes, D. N. Matsukevich, P. Maunz, D. L. Moehring, K. C. Younge, and C. Monroe. Measurement of the lifetime of the  $6p^2P_{1/2}$  level of  $\text{Yb}^+$ . *Phys. Rev. A*, 80:022502, Aug 2009.
- [27] Y. Wang, J. Minář, L. Sheridan, and V. Scarani. Efficient excitation of a two-level atom by a single photon in a propagating mode. *Phys. Rev. A*, 83:063842, Jun 2011.
- [28] P. O. Schmidt, T. Rosenband, C. Langer, W. M. Itano, and J. J. Bergquist and D. J. Wineland. Spectroscopy using quantum logic. *Science*, 29:749–752, July 2005.
- [29] Y. Lin, J. P. Gaebler, T. R. Tan, R. Bowler, J. D. Jost, D. Leibfried, and D. J. Wineland. Sympathetic electromagnetically-induced-transparency laser cooling of motional modes in an ion chain. *Phys. Rev. Lett.*, 110:153002, Apr 2013.
- [30] T. P. Harty, D. T. C. Allcock, C. J. Ballance, L. Guidoni, H. A. Janacek, N. M. Linke, D. N. Stacey, and D. M. Lucas. High-fidelity preparation, gates, memory, and readout of a trapped-ion quantum bit. *Phys. Rev. Lett.*, 113:220501, Nov 2014.
- [31] S. Muralidharan, L. Li, Kim J, N. Lütkenhaus, M. D. Lukin, and L. Jiang. Optimal architectures for long distance quantum communication. *Nat. Sci. Rep.*, 6:20463, 2016.
- [32] C. M. Natarajan, M. G. Tanner, and R. H. Hadfield. Superconducting nanowire single-photon detectors: physics and applications. *Superconductor Science and Technology*, 25(6):063001, 2012.
- [33] I. V. Inlek, G. Vittorini, D. Hucul, C. Crocker, and C. Monroe. Quantum gates with phase stability over space and time. *Phys. Rev. A*, 90:042316, Oct 2014.

- [34] G. Vittorini, D. Hucul, I. V. Inlek, C. Crocker, and C. Monroe. Entanglement of distinguishable quantum memories. *Phys. Rev. A*, 90:040302, Oct 2014.
- [35] D. A. Hucul. A modular quantum system of trapped atomic ions. *PhD Thesis, University of Maryland, College Park*, 2015.
- [36] S. M. Olmschenk. Quantum teleportation between distant matter qubits. *PhD Thesis, University of Michigan, Ann Arbor*, 2009.
- [37] D. L. Hayes. Remote and local entanglement of ions with photons and phonons. *PhD Thesis, University of Maryland, College Park*, 2012.
- [38] D. J. Wineland, C. Monroe, W. M. Itano, D. Leibfried, B. E. King, and D. M. Meekof. Experimental issues in coherent quantum-state manipulation of trapped ions. *J. Res. Nat. Inst. Stand. Tech.*, 103:259, 1998.
- [39] E. Mount, S.-Y. Baek, M. Blain, D. Stick, D. Gaultney, S. Crain, R. Noek, T. Kim, P. Maunz, and J. Kim. Single qubit manipulation in a microfabricated surface electrode ion trap. *New Journal of Physics*, 15(9):093018, 2013.
- [40] S. Seidelin, J. Chiaverini, R. Reichle, J. J. Bollinger, D. Leibfried, J. Britton, J. H. Wesenberg, R. B. Blakestad, R. J. Epstein, D. B. Hume, W. M. Itano, J. D. Jost, C. Langer, R. Ozeri, N. Shiga, and D. J. Wineland. Microfabricated surface-electrode ion trap for scalable quantum information processing. *Phys. Rev. Lett.*, 96:253003, Jun 2006.
- [41] P. Maunz. High optical access trap 2.0. *SAND2016-0796R*, 2016.
- [42] K. G. Johnson, B. Neyenhuis, J. Mizrahi, J. D. Wong-Campos, and C. Monroe. Sensing atomic motion from the zero point to room temperature with ultrafast atom interferometry. *Phys. Rev. Lett.*, 115:213001, Nov 2015.
- [43] J. Smith, A. Lee, P. Richerme, B. Neyenhuis, P. W. Hess, P. Hauke, M. Heyl, D. A. Huse, and C. Monroe. Many-body localization in a quantum simulator with programmable random disorder. *Nat. Phys.*, 2016.
- [44] R. Noek, G. Vrijsen, D. Gaultney, E. Mount, T. Kim, P. Maunz, and J. Kim. High speed, high fidelity detection of an atomic hyperfine qubit. *Opt. Lett.*, 38(22):4735–4738, Nov 2013.
- [45] D. Hayes et al. Entanglement of atomic qubits using an optical frequency comb. *Phys. Rev. Lett.*, 104:140501, 2010.
- [46] D. Trypogeorgos and C. J. Foot. Cotrapping different species in ion traps using multiple radio frequencies. *Phys. Rev. A*, 94:023609, Aug 2016.
- [47] R. C. Thompson. Spectroscopy of trapped ions. *Adv. At. Mol. Opt. Phys.*, 31:86–87, 1993.

- [48] J. J. Curry. Compilation of wavelengths, energy levels, and transition probabilities for Ba I and Ba II. *J. Phys. Chem. Ref. Data*, 33:725, 2004.
- [49] N. D. Scielzo, J. R. Guest, E. C. Schulte, I. Ahmad, K. Bailey, D. L. Bowers, R. J. Holt, Z.-T. Lu, T. P. O'Connor, and D. H. Potterveld. Measurement of the lifetimes of the lowest  $^3P_1$  state of neutral Ba and Ra. *Phys. Rev. A*, 73:010501, Jan 2006.
- [50] G. Leschhorn, T. Hasegawa, and T. Schaetz. Efficient photo-ionization for barium ion trapping using a dipole-allowed resonant two-photon transition. *Appl. Phys. B*, 108:159, 2012.
- [51] M. D. Rotter. Quantum feedback and quantum correlation measurements with a single barium ion. *PhD Thesis, University of Innsbruck, Austria*, 2008.
- [52] A. V. Steele, L. R. Churchill, P. F. Griffin, and M. S. Chapman. Photoionization and photoelectric loading of barium ion traps. *Phys. Rev. A*, 75:053404, May 2007.
- [53] David S. K., Peter K. S., Kermit C. S., and John C. T. Direct calibration of laser wavelength and bandwidth using the optogalvanic effect in hollow cathode lamps. *Appl. Opt.*, 16(10):2617–2619, Oct 1977.
- [54] D. De Munshi, T. Dutta, R. Rebhi, and M. Mukherjee. Precision measurement of branching fractions of  $^{138}\text{Ba}^+$ : Testing many-body theories below the 1% level. *Phys. Rev. A*, 91:040501, Apr 2015.
- [55] N. Kurz, M. R. Dietrich, Gang Shu, R. Bowler, J. Salacka, V. Mirgon, and B. B. Blinov. Measurement of the branching ratio in the  $6P_{3/2}$  decay of Ba II with a single trapped ion. *Phys. Rev. A*, 77:060501, Jun 2008.
- [56] N. Yu, W. Nagourney, and H. Dehmelt. Radiative lifetime measurement of the  $\text{Ba}^+$  metastable  $5D_{3/2}$  state. *Phys. Rev. Lett.*, 78:4898–4901, Jun 1997.
- [57] C. Aucher, T. W. Noel, M. R. Hoffman, S. R. Williams, and B. B. Blinov. Measurement of the branching fractions and lifetime of the  $5D_{5/2}$  level of  $\text{Ba}^+$ . *Phys. Rev. A*, 90:060501, Dec 2014.
- [58] H. Oberst. Resonance fluorescence of single barium ions. *Diploma Thesis, University of Innsbruck, Austria*, 1999.
- [59] J. D. Wong-Campos, K. G. Johnson, B. Neyenhuis, J. Mizrahi, and C. Monroe. High-resolution adaptive imaging of a single atom. *Nat. Photonics*, 10:606–610, 2016.
- [60] F. Splatt, M. Harlander, M. Brownnutt, F. Zhringer, R. Blatt, and W. Hnsel. Deterministic reordering of 40  $\text{Ca}^+$  ions in a linear segmented Paul trap. *New Journal of Physics*, 11(10):103008, 2009.

- [61] A. Kleczewski, M. R. Hoffman, J. A. Sherman, E. Magnuson, B. B. Blinov, and E. N. Fortson. Coherent excitation of the  $6S_{1/2}$  to  $5D_{3/2}$  electric-quadrupole transition in Ba. *Phys. Rev. A*, 85:043418, 2012.
- [62] M. Acton, K.-A. Brickman, P. C. Haljan, P. J. Lee, L. Deslauriers, and C. Monroe. Near-perfect simultaneous measurement of a qubit register. *Quantum Info. Comput.*, 6(6):465–482, September 2006.
- [63] D. Reiß, A. Lindner, and R. Blatt. Cooling of trapped multilevel ions: A numerical analysis. *Phys. Rev. A*, 54:5133–5140, Dec 1996.
- [64] I. Siemers, M. Schubert, R. Blatt, W. Neuhauser, and P. E. Toschek. The ”trapped state” of a trapped ionline shifts and shape. *EPL (Europhysics Letters)*, 18(2):139, 1992.
- [65] D. J. Berkeland and M. G. Boshier. Destabilization of dark states and optical spectroscopy in zeeman-degenerate atomic systems. *Phys. Rev. A*, 65:033413, Feb 2002.
- [66] A. Keselman, Y. Glickman, N. Akerman, S. Kotler, and R. Ozeri. High-fidelity state detection and tomography of a single-ion Zeeman qubit. *New J. Phys.*, 13(7):073027, 2011.
- [67] T. R. Tan, J. P. Gaebler, Y. Lin, Y. Wan, R. Bowler, D. Leibfried, and D. J. Wineland. Multi-element logic gates for trapped-ion qubits. *Nature*, 528:380–383, 2015.
- [68] F. Schmidt-Kaler, S. Gulde, M. Riebe, T. Deuschle, A. Kreuter, G. Lancaster, C. Becher, J. Eschner, H. Häffner, and R. Blatt. The coherence of qubits based on single  $\text{Ca}^+$  ions. *J. Phys. B: At. Mol. Opt. Phys.*, 36(3):623, 2003.
- [69] T. Ruster, C. T. Schmiegelow, H. Kaufmann, C. Warschburger, F. Schmidt-Kaler, and U. G. Poschinger. A long-lived Zeeman trapped-ion qubit. *arXiv:1606.07220*, 2016.
- [70] C. Aughter, C.-K. Chou, T. W. Noel, and B. B. Blinov. Ion–photon entanglement and bell inequality violation with  $^{138}\text{Ba}^+$ . *J. Opt. Soc. Am. B*, 31(7):1568–1572, Jul 2014.
- [71] T. Kim, P. Maunz, and J. Kim. Efficient collection of single photons emitted from a trapped ion into a single-mode fiber for scalable quantum-information processing. *Phys. Rev. A*, 84:063423, Dec 2011.
- [72] S. Olmschenk, D. N. Matsukevich, P. Maunz, D. Hayes, L.-M. Duan, and C. Monroe. Quantum teleportation between distant matter qubits. *Science*, 323:486, 2009.

- [73] P. J. Lee, K.-A. Brickman, L. Deslauriers, P. C. Haljan, L.-M. Duan, and C. Monroe. Phase control of trapped ion quantum gates. *J. Opt. B: Quant. Semi. Opt.*, 7(10):S371, 2005.
- [74] T. P. Harty, M. A. Sepiol, D. T. C. Allcock, C. J. Ballance, J. E. Tarlton, and D. M. Lucas. High-fidelity trapped-ion quantum logic using near-field microwaves. *Phys. Rev. Lett.*, 117:140501, Sep 2016.
- [75] S. Weidt, J. Randall, S. C. Webster, K. Lake, A. E. Webb, I. Cohen, T. Navickas, B. Lekitsch, A. Retzker, and W. K. Hensinger. Trapped-ion quantum logic with global radiation fields. *arXiv:1603.03384*, 2016.
- [76] J. A. Mizrahi. Ultrafast control of spin and motion in trapped ions. *PhD Thesis, University of Maryland, College Park*, 2013.
- [77] W. C. Campbell, J. Mizrahi, Q. Quraishi, C. Senko, D. Hayes, D. Hucul, D. N. Matsukevich, P. Maunz, and C. Monroe. Ultrafast gates for single atomic qubits. *Phys. Rev. Lett.*, 105:090502, Aug 2010.
- [78] K. Mølmer and A. Sørensen. Entanglement and quantum computation with ions in thermal motion. *Phys. Rev. A*, 62:022311, 1999.
- [79] D. Leibfried et al. Experimental demonstration of a robust, high-fidelity geometric two ion-qubit phase gate. *Nature*, 422:412, 2003.
- [80] G. Morigi and H. Walther. Two-species coulomb chains for quantum information. *The European Physical Journal D - Atomic, Molecular, Optical and Plasma Physics*, 13(2):261–269, 2001.
- [81] J. P. Home. Quantum science and metrology with mixed species ion chains. *Adv. At. Mol. Opt. Phys.*, 62:231–272, 2013.
- [82] D.F.V. James. Quantum dynamics of cold trapped ions with application to quantum computation. *Applied Physics B*, 66(2):181–190, 1998.
- [83] S.-L. Zhu, C. Monroe, and L.-M. Duan. Trapped ion quantum computation with transverse phonon modes. *Phys. Rev. Lett.*, 97:050505, Aug 2006.
- [84] A. Sørensen and K. Mølmer. Entanglement and quantum computation with ions in thermal motion. *Phys. Rev. A*, 62:022311, Jul 2000.
- [85] J. I. Cirac and P. Zoller. Quantum computations with cold trapped ions. *Phys. Rev. Lett.*, 74:4091, 1995.
- [86] D. Hayes et al. Coherent error suppression in multiqubit entangling gates. *Phys. Rev. Lett.*, 109:020503, 2012.
- [87] G. Kirchmair, J. Benhelm, F. Zhringer, R. Gerritsma, C. F. Roos, and R. Blatt. Deterministic entanglement of ions in thermal states of motion. *New Journal of Physics*, 11(2):023002, 2009.

- [88] C. J. Ballance, T. P. Harty, N. M. Linke, M. A. Sepiol, and D. M. Lucas. High-fidelity quantum logic gates using trapped-ion hyperfine qubits. *Phys. Rev. Lett.*, 117:060504, Aug 2016.
- [89] B. B. Blinov, L. Deslauriers, P. Lee, M. J. Madsen, R. Miller, and C. Monroe. Sympathetic cooling of trapped  $\text{Cd}^+$  isotopes. *Phys. Rev. A*, 65:040304, Apr 2002.
- [90] C. J. Foot. Atomic physics. *Oxford University Press*, 2005.
- [91] F. Diedrich, J. C. Bergquist, Wayne M. Itano, and D. J. Wineland. Laser cooling to the zero-point energy of motion. *Phys. Rev. Lett.*, 62:403–406, Jan 1989.
- [92] C. Monroe, D. M. Meekhof, B. E. King, S. R. Jefferts, W. M. Itano, D. J. Wineland, and P. Gould. Resolved-sideband raman cooling of a bound atom to the 3D zero-point energy. *Phys. Rev. Lett.*, 75:4011–4014, Nov 1995.
- [93] G. Morigi, J. Eschner, and C. H. Keitel. Ground state laser cooling using electromagnetically induced transparency. *Phys. Rev. Lett.*, 85:4458–4461, Nov 2000.
- [94] R. Lechner, C. Maier, C. Hempel, P. Jurcevic, B. P. Lanyon, T. Monz, M. Brownnutt, R. Blatt, and C. F. Roos. Electromagnetically-induced-transparency ground-state cooling of long ion strings. *Phys. Rev. A*, 93:053401, May 2016.
- [95] G. Morigi. Cooling atomic motion with quantum interference. *Phys. Rev. A*, 67:033402, Mar 2003.
- [96] Y. Stalgies, I. Siemers, B. Appasamy, and P. E. Toschek. Light shift and Fano resonances in a single cold ion. *J. Opt. Soc. Am. B*, 15(10):2505–2514, Oct 1998.
- [97] G. Janik, W. Nagourney, and H. Dehmelt. Doppler-free optical spectroscopy on the  $\text{Ba}^+$  mono-ion oscillator. *J. Opt. Soc. Am. B*, 2(8):1251–1257, Aug 1985.
- [98] R. Islam et al. Beat note stabilization of mode-locked lasers for quantum information processing. *Opt. Lett.*, 39:3238–3241, 2014.